ISSN 3078-1760
E-ISSN 3078-1965

BAKI ALİ NEFT MƏKTƏBİ
BAKU HIGHER OIL SCHOOL

JESMT

JOURNAL OF ENGINEERING SCIENCES & MODERN TECHNOLOGIES

VOLUME 1 • NUMBER 1
2025

www.jesmt.org

JESMT
JOURNAL OF ENGINEERING SCIENCES & MODERN TECHNOLOGIES

Contact Address

Baku Higher Oil School Campus,
Yeni Salyan Highway 3rd km, 25, Sabail district, AZ1023, Baku, Azerbaijan
Phone: (+994 12) 521 00 00 (ext.: 33046); Fax: (+994 12) 521 33 64;
e-mail: submission@jesmt.org; web: https://jesmt.org

Register No: 4364, 16.12.2021

JESMT
JOURNAL OF ENGINEERING SCIENCES & MODERN TECHNOLOGIES

Volume 1, Number 1, 2025

Table of Contents

From the Founding Editor

Dear readers and esteemed scholars,

It is with great pride and joy that I introduce the inaugural issue of the "Engineering Sciences and Modern Technologies" international scientific journal, published under the auspices of Baku Higher Oil School. This journal is dedicated to advancing the fields of engineering sciences and modern technologies by providing a platform for the dissemination and discussion of in-depth scientific research and innovative ideas. Our objective is to expand the knowledge base of the scientific community, particularly among scholars, engineers, and researchers working in these fields, and to stimulate their scientific endeavors.

The articles published in this journal will present the results of research conducted across various branches of engineering sciences and technology, reaching a broad audience and fostering new discussions within the scientific community. Our publication is committed to facilitating knowledge exchange among scholars, strengthening scientific collaborations, and contributing to the advancement of innovative technologies.

I extend my deepest gratitude to everyone who has supported the creation and successful launch of this journal, and I am confident that it will occupy a significant place in the scientific world.

Sincerely,

Elmar Gasimov
Founding Editor,
Rector of Baku Higher Oil School

Journal of Engineering Sciences & Modern Technologies
ISSN 3078-1760, E-ISSN 3078-1965
Volume 1, Number 1, 2025, page 1-8

BAKI ALİ NEFT MƏKTƏBİ
BAKU HIGHER OIL SCHOOL

https://jesmt.org/

https://doi.org/10.70334/3078-1965.2025.1.1

UDC 502.3

Entropy law and global eco-energy problem

Fuad Valiyev

Baku Higher Oil School, Baku, Azerbaijan, fuad.valiyev@bhos.edu.az

Keywords:

Biogical factor,
CO_2 emission,
Global footprint,
Energy consumption,
Global annual emission,
Coal,
Sustainable development,
Ecological disaster

A B S T R A C T

The demand for energy is gradually increasing. At present, this demand is mainly met by fossil fuels such as oil, gas, coal. However, according to the second law of thermodynamics, the process of converting thermal energy into mechanical energy is accompanied by an increase in entropy, and accordingly, by emissions into the environment in the form of heat and material waste. All environmental problems are ultimately the challenging manifestation of the accelerated growth of Entropy.

The article deals with global eco-energy problems related to the critical growth of anthropogenic impact on nature in the context of the law of entropy.

Received: 10.01.2024
Accept: 15.02.2024

For millennia, Man and Nature have coexisted in harmony. Initially, people used the gifts of the Nature without causing a significant damage to it. However, this idyll was broken at the end of the 18th century with the start of the Industrial Revolution, marked by the invention and introduction of thermal(steam) machines. The emergence of technologies with high energy consumption has led to a sharp increase in demand for energy.

These days, Humanity faces a number of vital and insurmountable problems, but the greatest of all is the Global Eco-Energy Problem. Our modern civilization, with all the mod cons like heating and cooling, cars and planes, owes much to thermal machines. However, for all these privileges we are doomed to pay way too much in accordance with the The Second Law of Thermodynamics, the immutable law that reflects the fundamental asymmetry in natural processes: *Mechanical energy can be fully converted into thermal energy, while the reverse process is not fully possible – in a cyclically recurring process only a certain part of the heat energy can be converted into mechanical energy!*

If we want to turn heat energy into mechanical energy or electricity, we have to pay a "tax". The tax, called Anergy, is heavy enough and is dumped into the environment in the form of contaminated, toxic energy, which is already unfit for further use. For example, the efficiency of modern cars on average is 0.2. This means that out of ten liters of gasoline in our gas tank, only two liters are consumed usefully, the rest is thrown into Nature from the muffler in the form of pollutants.

The quality of energy is determined by a fundamental physical parameter called Entropy. With the growth of Entropy, which is a measure of disorder and chaos, Energy, as if subjected to inflation, loses its quality, i.e., its ability to turn into useful work deteriorates.

Based on the Second Law of Thermodynamics or the Law of Entropy all processes in Nature go in the direction of increasing Entropy – from order to disorder! In fact, the Entropy crisis, not the Energy crisis, is the greatest danger for mankind's future. All environmental problems are ultimately the challenging manifestation of the accelerated growth of Entropy.

All processes where the Energy conversions take place are simultaneously the Entropy producing processes associated by emissions in the form of heat and material pollutants into the environment. The change of entropy characterizes the dissipation of energy in the process of transformation of various types of energy into each other.

The main sources of Energy are currently fossil fuels - oil, gas and coal. We burn them, we convert the received thermal energy into mechanical or electrical energy, paying a huge contribution in the form of heat and material dirty emissions into the Nature. Billions of heat machines are used in cars, planes, ships, industrial facilities, power plants, household, and billions of tons of contaminated, toxic emissions are constantly poisoning the environment every hour, every day – they are discharged into rivers, seas, released into the atmosphere, thrown into the soil. The very fragile energy-matter balance in the Earth's biosphere is disrupted, and, eventually, the threat to the existence of life on our planet increases day by day.

Man, as a biological factor, has existed on Earth for thousands of years. However, over the past 100 years, scientific and technological capabilities of human beings have reached the level that would give them dominance in the ecosystem, empower to change the fundamental features of the biosphere and the planet as a whole. According to Global Footprint Network Organization, almost half of wildlife has been destroyed by the last two human generations.

The amount of CO_2 emitted annually into the atmosphere has reached a monstrous value - 40 billion tons! Currently, the concentration of CO_2 in the atmosphere has reached a record value for the last 800 thousand years – 410ppm. This is one of the main causes of global warming - the gradual rise of average temperature of the Earth.

Those who deny the fact of global warming are either naive or come from certain political and business interests.

Like all other factors that ensure life on Earth, the amount of CO_2 is set by the divine will at a certain optimal functional level necessary for the existence of life. For thousands of years, until the beginning of the 19th century, the amount of CO_2 in the Earth's atmosphere, with small fluctations, has changed to around 280 ppm. However, with the outbreak of the industrial revolution, as a clear indication of the ever-increasing anthropogenic aggression of man to nature, the amount of CO_2 has steadily increased. (Fig.1)

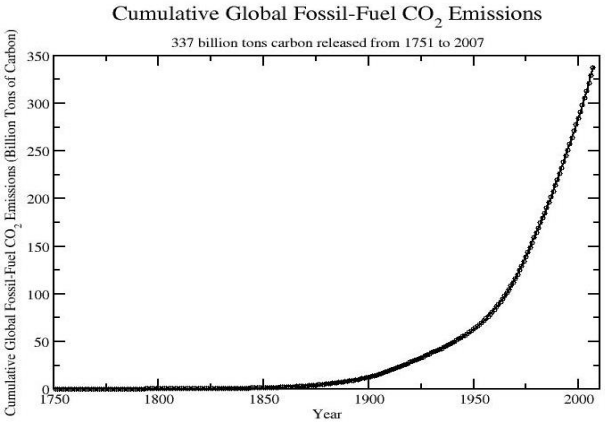

Fig 1. Source: CDIAC

The concentration of CO_2 in the atmosphere is rapidly increasing. In 1900, the global annual emission was 2 billion tons, but now it is 20 times higher. The growth rate of CO_2 in the atmosphere is 2% per year on average. The areas that produce the largest amount of CO_2 are the electricity and heat, transport and industrial sectors. The share of household in this issue is relatively small.

Fig. 2 shows the dynamics of CO_2 emissions change in developed and developing countries in 1965-2013. As it seems, CO_2 emissions in developed countries have stabilized around 15 billion tons since the 1980s. However, emissions in developing countries continue to increase year after year.

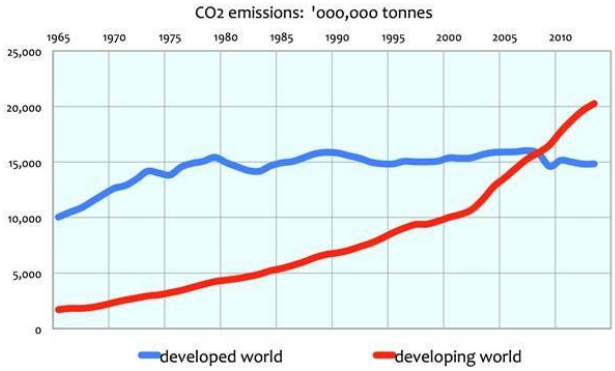

Fig 2. Source: BP Statistical Review of World Energy

According to data for 2018 (Joint Research Center, EDGAR), the world's leading manufacturers of CO_2 are China, the United States, the countries of the European Union, India, Russia and Japan. In the same year, China produced 11255.9 million tons (29.7% world total), USA – 5275.5 million tons (13.9%), EU – 3457.3 million tons (9.3%), India – 2621.9million tons (6.9%), Russia – 1748.4 million tons (4.6%) and Japan – 1198.6 million tons (3.2%) of CO_2.

The main factor that drives the rise in CO_2 concentration in the atmosphere is the steady increase in energy demand around the world, which is primarily met by the use of organic

mineral fuels.As can be seen from Fig.3, the world's energy consumption has increased by more than 3.5 times over the past 50 years, mainly due to oil, gas, coal.

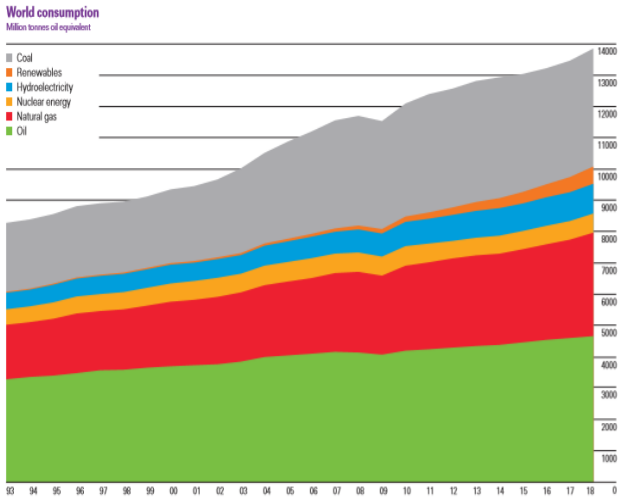

Fig 3. Source: BP Statistical Review

Most CO_2 is produced by burning coal, and currently the share of coal in the world's energy resources is quite large. For China, which is the largest CO_2 "manufacturer", the share of coal in the energy balance is about 60%.The share of the mineral-organic "trio" consisting of coal , oil and gas in the global energy consumption balance of 2014 is about 86%. The share of renewable energy sources, unfortunately, is still very negligible.

If the rate of change of any quantity is directly proportional to its numerical value, this quantity is increased by exponential law. This means that as the quantity N grows, its growth rate dN/dt also grows. Mathematically, the differential equation of exponential growth is expressed as follows: $\mathbf{dN/dt= kN}$, if k is taken as a constant, the solution of the equation is $\mathbf{N=N_0e^{kt}}$.

Global processes have significantly accelerated - the changes in Nature that would take millennia to happen, can be observed within decades now. Processes such as population growth, energy production and consumption, environmental pollution, epidemics, etc. mathematically expressed by exponential law. The essence of processes obeying this law is that they eventually acquire the character of an explosion, and the growing quantity suddenly reaches a certain critical level.

In this regard, Prof. Dennis Medeouz draws an interesting example. Let's say that on the surface of the lake there is a white-water lily, and every day its number is doubled, that is, the number of lilies is multiplied by a geometric series- 1, 2, 4, 8, 16... If there is no obstacle to its growth, it will occupy the entire surface of the lake for 30 days, destroying all other livings in the lake.

The peculiarity of this process is their insidious nature. In the first stages, growth for a long time is very insignificant, and no one thinks that it can cause problems. There arises an illusion of calmness, security... Thus, on the 21st day of the thirty-day process lilies occupied only 0.2% of the surface of the lake. At the end of the 25th day - only 3 per cent. As if there is no reason for the trouble, because 97 per cent of the lake surface is still intact...

However, in the last stages, the speed of the process becomes so great that it is no longer possible to suspend the process. On the 29th day lilies will occupy half of the lake. It's already too late - you only have one day left to save the lake... The next day the lake will be completely covered with lilies... *Thus, it took 29 days to cover one half of the lake, and only one day is required to cover the other half... If we wait for the" 29th day", there will simply not be enough time to solve the problem...*

The population of the planet is increasing, the material needs of people are growing, which necessitate a permanent increase in industrial and energy capacity. Due to population growth and accelerated economic activity, the biocapacity available to each inhabitant of the Earth during the last fifty years decreased nearly twice and now it is only 1.7gha.

The capacity of 10 countries with the largest biocapacity has been shown in the Fig. 4. As it seems, about 60% of the total biocapacity in the world belongs to these countries. Brazil is the country with the largest biocapacity in the world. However, over the past fifty years, as a result of the relentless exploitation of the existing ecosystem, the bioresources of this country have decreased by 71% (Global Footprint Network Organization).

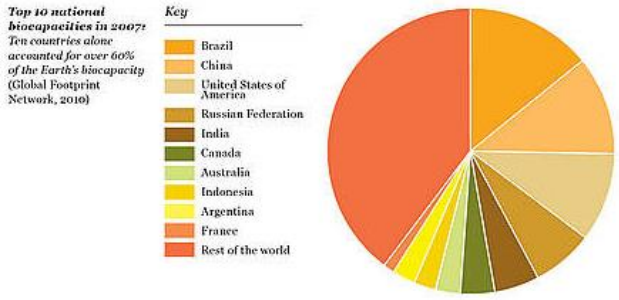

Fig 4. Source: Global Footprint Network Organization

Currently, 86% of the world's population lives in countries where the Ecological Footprint exceeds the biocapacity of these countries.

One of the alarming manifestations of the Global Warming is the accelerated melting of Antarctic and Arctic glaciers. High concentration of CO_2 in the air is the cause of an increase in the

acidity of Ocean waters, and this in turn brings about irreversible changes in the flora and fauna of the Ocean.

The area of tropical forests is reduced annually by about 100 thousand square kilometers. If this goes on, the tropical forests, the "lungs" of the planet, will disappear completely in the coming decades, which in turn will accelerate climate change.

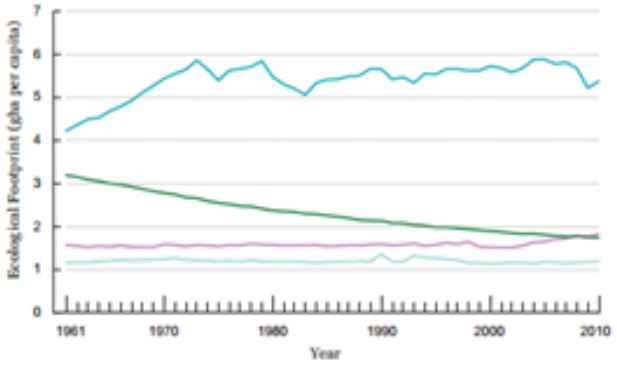

Fig 5. Source: World Bank classification and data

The dynamics of the ecological footprint of low, middle and high-income countries per capita and the biocapacity in the world between 1961-2010 are shown in Fig. 5. As it seems, the per capita ecological footprint of high-income countries increased sharply between 1961-1971. In the following years, although the ecological footprint remains stable, the difference with biocapacity is gradually increasing. On the other hand, although the per capita ecological footprint of low- and middle-income countries remains stable for almost 50 years, the ecological footprint of middle income countries has already surpassed the biocapacity, and for low income countries the difference with biototome is steadily decreasing.

The wounds inflicted by Man on our planet are clearly visible from space. On the surface of the Pacific Ocean, there is a huge gray spot drifting at times between America and Asia. The spot has an area of approximately 1.5 million square kilometers and is an island formed mainly by plastic debris.

This Island, called the Great Pacific Ocean Garbage Patch, is a kind of Indictment addressed to humanity for its cruel, ruthless attitude to Nature over the past 100 years.

Humanity today lives as it were at the expense of a debt taken from nature and this debt is not reduced, on the contrary, it is growing year after year. In the Fig.6, the dynamics of global ecological footprint and biocapacity change in 1961-2012 is shown. In the 70-ies of the last century, as can be seen from the figure, a very annoying for mankind transition took place – the demand for Natural resources exceeded the self-restoration potential of the biosphere.

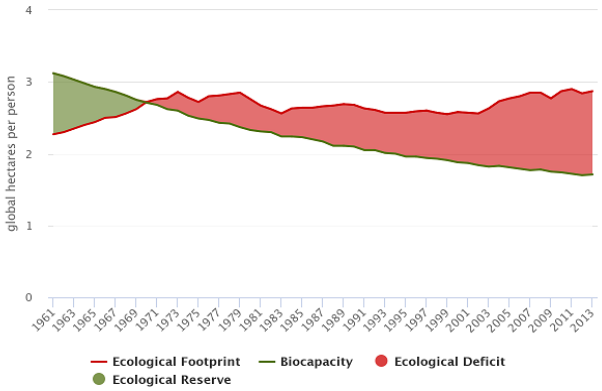

Fig 6. Source: Global Footprint Network

The increase in the number and demand of the population from year to year, and in connection with this, a decrease in potential resources, intensification of anthropogenic loading of Nature, climate changes are the bitter truth of the last fifty years.

The Fig. 7 shows the dynamics of changes in the world's Ecological Footprint factors during 1961-2012 and the required conventional number of Earths in the ordinate axis. It seems that over the course of 50 years, the CO_2 footprint has increased dramatically, and currently, it accounts for more than half of the total footprint, while the footprint of other components has remained almost constant. As you can see, starting in 1970, the presence of one planet was not enough to satisfy mankind's demand for bioresurses. In 2012, we already needed 1.7 Earth planets!

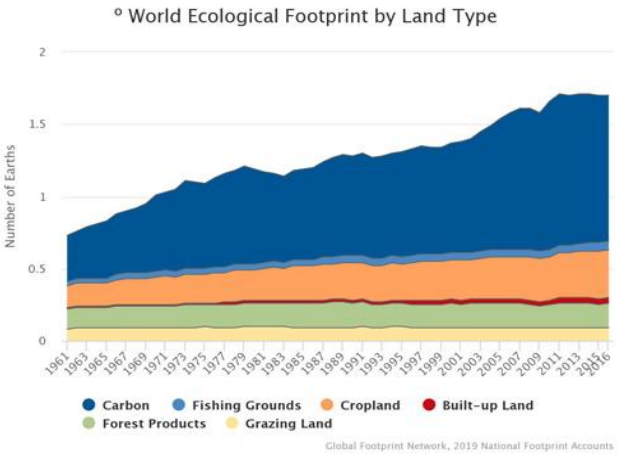

Fig 7. Source: Global Footprint Network report

At present, the ecological footprint of humanity has surpassed the total area of the Planet that could potentially be used as well as the capacity of the Earth to restore its resources, and our growing demand is being met only by the physical and biological degradation of the planet. The world population continues to grow, and people's

demand for bioresources and a more comfortable life is also growing. This, in turn, results in excessive production of food and household goods, building materials, clothing, and, as a result, more energy consumption, which is accompanied by a significant increase in waste, including CO_2, thrown into Nature.

If everyone in the world followed the trend of the inhabitants of developed and rich countries in terms of ecological footprint, we could destroy more than one planet. For example, resource consumption of the population of Qatar and Luxembourg exceeds the current capacity of their territories by 10 times.

Thanks to scientific, technical and technological achievements, the Human Development Index of people in developed countries has significantly increased, triggering the increase in the quality and quantity of food, clothing, material goods, rest, and travel. A brutal exploitation of Nature and violation of the divine balance in the ecosystem have exacted a heavy price.

Only 20% of the planet's population lives in industrially developed countries, but these countries produce 75% of the total industrial waste that pollutes the environment.

The Fig. 8 shows the dependence between the Human Development Index and the ecological footprint for different countries. As you can see, the increase in wealth is accompanied by an increase in the footprint. North America, Europe and some Middle East, Asia-Pacific Basin countries have the highest HDI, but these same countries have the greatest ecological footprint.

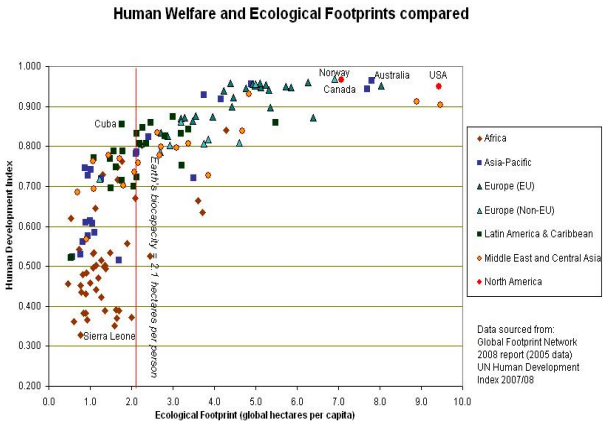

Fig 8. Source: Global Footprint Network report

It is inconceivable, but the fact that Nature, stable and unchanged for millenia, has been subjected to unprecedented interference in the lifetime of only two generations and undergone drastic changes in quantity and quality. We owe it to Nature for everything - the water we drink, the food we eat, the energy we consume, and the material blessings we depend on, and we pay back evil for good. While our violence against Nature is nothing more than ingratitude, the punishment of ingratitude is quite severe: natural cataclysms, drought, soil erosion, desertification, extreme climate change, intensification of glacial melting, depletion of natural food products and so on.

Humanity today is living in a debt that it receives from Nature, and this debt not only fails to decrease, but on the contrary, it continues to grow year after year.

The Ecological Overshoot Day or the Day of Ecological Debt is a month and a day of the year when the "budget" of the Earth required for one year is already exhausted. In other words, this is the day when the total amount of bioresources consumed by humanity from the beginning of the year to the present time equals to the natural capital of the Earth which can be restored only within one year. The Ecological Overshoot Day gradually shifts its place in the calendar - in 2018, for instance, we"celebrated" this day on August 1 (Fig. 9). This means that all our bioresources to be consumed within a a year were squandered by the 1st of August 1. In the remaining five months until the end of the year, we were forced "to take a debt" from the next year. And the cost of this growing debt is heavy – shortage of food and drinking water, erosion of the soil, an increase in the amount of carbon dioxide in the air, an increase in the acidity of the ocean, a decrease intheland fertility, etc.

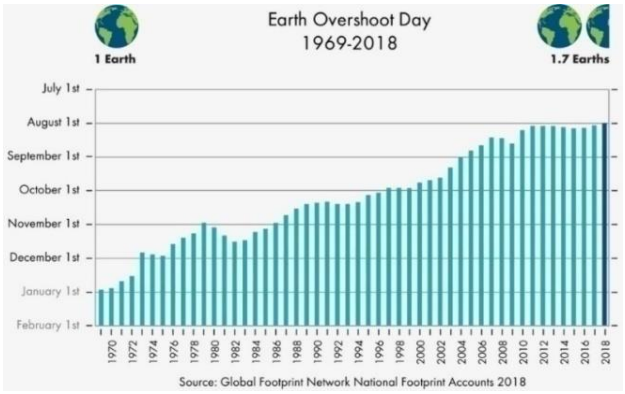

Fig 9. Source: Global Network Footprint Accounts

It should be noted that the Ecological Debt Day coincides with different calendar days in different countries. For example, this day is "celebrated" in the United States, Canada in March, in Sweden, Finland, Austria, Russia-in April, in Germany, France, England, Japan, Italy – in may. In Turkey, the debt Day falls on July 11, and in Azerbaijan on October 10.

The world economy is growing steadily. The annual increase in global energy consumption is approximately 4% Is there an end to economic

growth and energy production? Given that the Earth is a small cosmic space, the existence of a global production limit is inevitable. This limit is determined by the dangerous limit of the ecological problems for mankind that are growing in parallel with the increase in production. The atmosphere, water basins, land can only process a certain amount of production waste. After this critical threshold, the irreversible processes that arise can lead to natural cataclysms, and eventually, can destroy the existence of mankind.

Thus, the increase in production makes it inevitable to increase energy conversions, and, accordingly, global entropy, which means an increase in polluted energy, harmful waste thrown into the environment. The Earth can only process this polluted emission to a certain extent. This limit, in fact, indicates the final limit of the volume of production. This was stated back in the 70s in the report of the Club of Rome[1].

Based on the phenomenological principles of non-equilibrium thermodynamics, it is possible to identify the relationship between the processes of energy conversion, entropy production and thermal-material emissions. The basis here is that any process of energy conversion is, in principle, irreversable, and in accordance with the second law, irreversable processes produce entropy, which is accompanied by thermal and material emissions.

The entropy production is characterized by the density of entropy production defined as [2]:

$$\rho_S = j_Q \cdot \nabla \frac{1}{T} + \sum j_k \cdot \left(-\nabla \frac{\mu_k}{T} + \frac{F_k}{T}\right)$$

Here, $\mathbf{j_Q}$ and $\mathbf{j_k}$ are, respectively, the density of heat and diffusion currents caused by generalized forces, such as temperature gradients and chemical potentials($\boldsymbol{\mu_k}$), as well as specific external forces ($\mathbf{F_k}$). The formula shows that the presence of gradients in the system of corresponding physical and chemical parameters, as well as external forces that can change the thermodynamic state, inevitably leads to the production of entropy, which is accociated by thermal and material emissions into the environment.

Developed countries, especially the United States, have the most production capacity, accordingly, they are the most entropy producers. And it seems that they are not about to reduce this very dangerous for the future of mankind production, which has many, most importantly, political and social reasons.

All non-regenerative, irreversible processes increase entropy, and if we take into account that both in Nature and production processes there are no absolutely reversible processes then we have to admit that the permanent increase of entropy is inevitable. *The transformation of energy and the increase in entropy are integral processes - where that energy conversion goes there entropy grows.*

If entropy decreases in any process, this is not yet an absolute decrease, since this decrease is accompanied with an increase in entropy in another process (space), which in total overcomes the initial decrease in entropy.

Thus, although the creative activity of mankind, the provision of vital demand, the creation of certain comfort for living, reduces entropy locally, it increases entropy globally, that is, the creation of local order is necessarily accompanied by an increase in global disorder. The growth of population and social needs require permanent economic growth, which, in fact, is contrary to the laws of thermodynamics, according to which nothing can be created without energy conversion and the corresponding production of entropy.

The current predatory exploitation of natural resources will result in ecological catastrophe as no time left for long reasoning and procrastination. The delay may have fatal and irreversible consequences with two possible scenarios: *Either a sharp decline in all life indicators or a gradual transition to self-maintenance, a moderate life in harmony with the Nature. The choice is ours! Alarm bells are ringing – it's the Choice Time now!*

The concept of sustainable development is the concept of preserving Nature by ensuring the minimum quality of life, meeting the current rasional demand, as well as not depriving future generations of normal living opportunities.

There are two fundamental scientific problems the solution to which can once and for all save humanity from the Energy-Entropy concern: 1) Obtaining controlled nuclear fusion 2) Discovering an effective and efficient method of free hydrogen production and its use as a fuel. Of-course, these problems will be solved sooner or later, but the main thing for humanity is to survive until that time…

In the meantime we have only two opportunities to mitigate the existing problem: 1. Moving towards a large-scale use of renewable energy sources 2. Ensuring maximum energy saving regime in all fields of activity, in household and industry, with the wide application of energy-saving methods and technologies.

Despite all the existing problems, the share of renewable energy sources in the world energy balance is growing. German experience in this matter is commendable. As can be seen from the Fig. 10, approximately 14.7% of the energy consumed in Germany in 2019 was renewable

energy. Roughly 40% of Germany's electricity is from renewable sources and the goal is at least 80 percent by 2050.

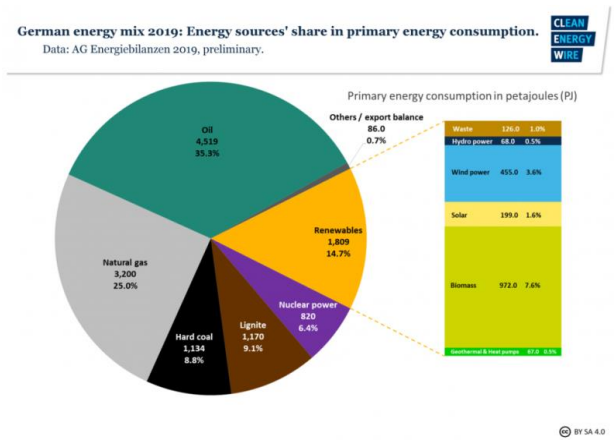

Fig 10. Source: AG Energiebilanzen 2019

The Fig.11 shows the dynamics of changes in the share of different sources for electricity production in Germany over the period 1990-2019. As you can see, over the past 20 years, there has been a significant increase in the share of renewable sources, while the share of non-oil products, and especially the share of coal, is decreasing year by year.

As you can see, over the past 20 years, there has been a significant increase in the share of renewable sources, while the share of non-oil products, and especially the share of coal, is decreasing year by year.

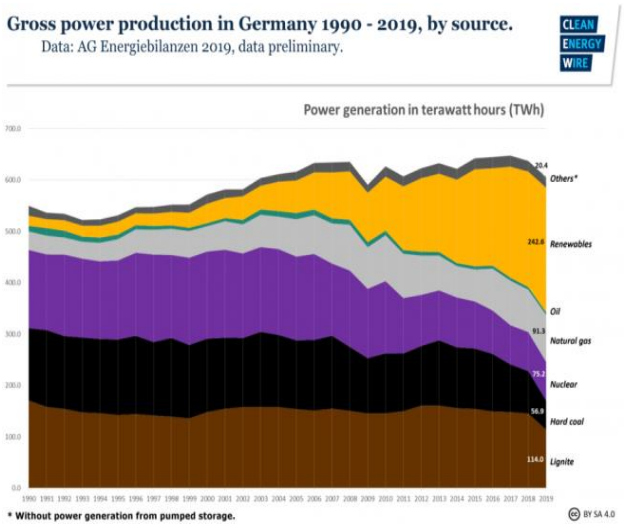

Fig 11. Source: AG Energiebilanzen 2019

For a long time, scientists have been announcing the upcoming global ecological disaster. In 1968, an organization called Club of Rome was established with the mission to attract the world's leading scientists to the scientific assessment of the ways of human development, future global problems, as well as to inform the world community about the existing global threats.

The first report, prepared on the basis of comprehensive scientific research commissioned by the Club, was presented by a group of scientists from the Massachusetts Institute of Technology (MIT), under the guidance of a prominent scientist on the dynamics of the system, Professor Jay Wright Forrester. Later, the reports of professors D.L. Meadows, E. Pestel, M. Mesarovich and others were presented. The final theses of these reports were quite alarming: *"The current pace of exploitation of natural resources and current way of life will lead mankind to ecological disaster in the 21st century... If humanity does not give up its harmful habits, if it does not change its attitude towards Nature, there is no salvation for it...The power without wisdom has turned Man into a modern barbarian with a magnificent power, but without any rational understanding of the application of this power... There is only one way to stop the dangerous course of processes - balancing the flow of resources that ensure the existence of man with the real biopotensial of the Earth".*

In 2010, more than 250 members of the United States National Academy of Sciences signed a Declaration entitled "Climate Change and the Integrity of Science".The document presented the general results of a long-term study of the UN intergovernmental Commission on climate change with the participation of parallel working groups. The results were quite pessimistic: Atmospheric CO_2 and ocean acidity continue to increase, and global warming is accelerating... And at the end of the Declaration it was noted: *"Society has two choices: We can ignore the science and hide our heads in the sand and hope we are lucky, or we can act in the public interest to reduce the threat of global climate change quickly and substantively. But delay must not be an option!".*

Unfortunately, despite all the alarming warnings, no serious steps were taken to solve the problem, and the process continued to deteriorate. Finally, political figures, heads of the world's leading countries also began to understand that the situation is really reaching a critical level. At the conference attended by the heads of 195 countries in Paris in 2015, a historic agreement was reached on measures to mitigate the climate change. But, unfortunately, there is no hope that all signatories will remain faithful to their obligations, since they are nothing more than promises of a declarative nature made on a voluntary basis, having no legal basis and mechanism to be controlled. The US president has already stated that his country will not follow the agreement.

If the present state remains intact, the catastrophe will be inevitable. The only way to stop the dangerous course of processes is to bring the resource streams supporting life existence of people in accord with levels admissible for the Earth potential. The situation is severe but not hopeless. As bitter as the facts are, fortunately, everything has not been lost and there is enough grief for optimism in the future. It is encouraging that more and more people are now realizing the global scale of the problem. The restoration of the increasingly fragile ecosystem of the Earth depends on the extent to which all people perceive the current danger.

Living in a thrifty regime, away from extremism, wastefulness in our everyday life, away from excessive demand in food, clothing, entertainment, comfort, travel should become the main paradigm of life. Each person should evaluate personal ecological footprint and make appropriate changes in his/her life to reduce it to a normal level. Energy saving, moderation in living, in food, in clothing, in entertainment should be our lifestyle. People need to realize that energy wastefulness dooms future generations to misfortune. People need to realize that now there are no alternatives for surviving of Adam's children beyond confession, reconciliation, tolerance and collaboration.

Only together we can save our Living Planet from barbaric attitude, from cruelty to wildlife. Without waiting for the 29th day when the environmental crisis will reach the limit of the explosion and it will be to late to do anything, people should realize that they are the inhabitants of a very small, in the cosmic sence, space called Earth, and the only way to survive is to get rid of mutual hatred, intolerance and build a modest, thrifty and civilized community to preserve Mother Nature.

References and Sources

[1] Meadows, D.H. The Limits to Growth, Universe Books, 1972

[2] Reiner Kümmel, The Second Law of Economics, Springer, 2010

[3] BP 2015-2018 data of the BP Statistical Review of World Energy

[4] IEA energy balance statistics for 1970-2015

[5] Global Carbon Project (GCP);

[6] Carbon Dioxide Information Analysis Center (CDIAC)

[7] Global Footprint Network Organization

[8] World Bank classification and data

[9] AG Energiebilanzen 2019

Journal of Engineering Sciences & Modern Technologies
ISSN 3078-1760, E-ISSN 3078-1965
Volume 1, Number 1, 2025, page 9-23

BAKI ALİ NEFT MƏKTƏBİ
BAKU HIGHER OIL SCHOOL

https://jesmt.org/

https://doi.org/10.70334/3078-1965.2025.1.9

UDC 550.8

Hydrostatic pressures evaluation for effective benchmarking of basin's abnormal pressures

Rauf Nadirov

Baku Higher Oil School, Department of Petroleum Engineering, Baku, Azerbaijan,
rauf.nadirov@bhos.edu.az; rauf.nadirov@socar.az

Keywords:

Hydrostatic pressures,
Overpressure,
Brine salinity,
Brine density,
Temperature,
South Caspian basin

A B S T R A C T

The paper addresses a number of problematic issues that arise in the course of analysis of oil-and-gas bearing basins, their modelling and quantitative forecasting of some the most important parameters of its formation and development.

Researches carried out and described in the paper are focused on the problem of development of pore pressures in permeable rocks of the South-Caspian basin (SCB).

The paper also describes the problematic issues related to hydrostatic pressure in permeable rocks of the SCB. Hydrostatic pressure is a benchmark that allows one to draw conclusions about the presence of overpressure (OP) in the basin. The paper describes the technique of their correct calculation and forecasting dependent on the brine salinity, distinctive features of development in various stratigraphic units and zones of the basin. The quantitative variations and approaches that provide subsequent quantitative assessment of OP are given using proposed methodology, examples of their assessment in one or another part of the basin.

The issues studied and described in the paper are focused on the initial modules of the basin analysis and modelling. They covering such stages of lithogenesis as sediment deposition, subsidence, compaction, lithologic-facies characteristics and the heating associated with these processes, formation of overpressure and the evolution of reservoir properties formed as a result of the formation of different facies within the sedimentary rocks.

Received: 05.10.2020
Accept: 11.12.2023

I. Introduction

It is generally recognized that after the primary and secondary recovery mechanisms are carried out in an oil reservoir, up to two third of the crude oil remain trapped in the reservoirs due to the dominating capillary forces or poor sweep efficiency of the injection fluid. In order to mobilize the trapped oil and increase the drainage efficiency, more effective and advanced recovery methods must be implemented.

The hydrostatic pressures (HSP) in the permeable sediments of the basins where over-pressures (OP) are developed, are the base level of pore pressures, with respect to which conclusion is made whether the pressures in these rocks are abnormally low (underpressure), high (overpressure) or normal hydrostatic pressures (NHP). This conclusion is primarily made based on comparative analysis of measured pore pressures in permeable rocks in the wells with hydrostatic pressures calculated by default gradient equations. If, in this case, the values of pore pressures measured in the wells coincide with those calculated for the specified hydrostatic gradients, then the pressures are not considered abnormal, either high or low. Deviations from the calculated gradient line of hydrostatic pressure, predominantly upwards, are identified as abnormally high pore pressures or overpressures [1, 2]

However, one should mention the occurrence of OP in impermeable rocks, primarily in clays.

The most common and widespread mechanism of OP occurrence is the process of underbalanced compaction during subsidence, when as a result of compaction at high sedimentation rates, water in clay pores does not have time to migrate to neighbor permeable sediments. As a result, overpressures arise in clays, and pore pressures begin exceeding hydrostatic pressures, which is expressed in the deviation of the pore pressure curve from the ordinarily straight line of hydrostatic pressures vs depth [3].

This curve of change in normal hydraulic pressures with depth is shown graphically as a straight line derived from the fixed gradient values determined by the averaged density of mineralized water in buried reservoir rocks (Fig. 1).

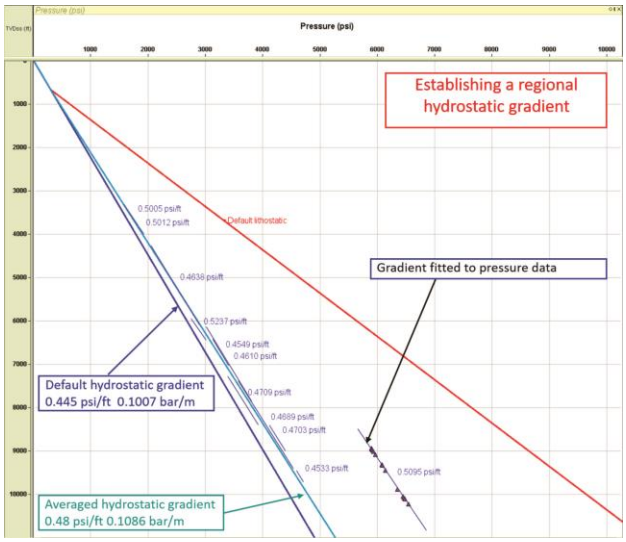

Fig. 1. Hydrostatic pressure lines based on fresh water gradient (dark blue) and estimated average from water gradients from different drilled reservoirs (light blue).

Usually, in the process of prediction of pressures for well planning, the default averaged or default value accepted for a particular oil-gas basin or region is used. The density of water varies, to a large extent from basin to basin, depending on its salinity, which varies from the seawater to deep water brines. In addition, the salinity of groundwater tends to increase with depth from fresh water to saturated solutions (Fig. 2).

In some basins, for example, in the section of sediments of the South Caspian basin, intervals of reverse or cyclic mineralization are observed. The gradients of hydrostatic pressure in the basins are, in fact, far from simplified linearity, actually varying with depth depending on changes in mineralization, in other words, the salinity of the underground water brines, which determine their density and hence the gradients of hydrostatic pressures. Thus, an accurate quantitative forecast of hydrostatic pressures narrows down to a prediction of water density, which in turn predicts the salinity of the waters that make up the section of horizons.

The algorithm for solving this problem can be represented as follows.

II. Theory and Methods

The algorithm for solving this problem can be represented as follows.

Definition for hydrostatic pressure (HSP) could be formulate as pressure exerted by a static column of fluid. HSP is a function of the fluid density and the vertical height of the fluid column. It can be expressed by the equation [1,2,3]:

$$P = \rho * g * h \qquad (1)$$

where: **P** is the HSP, **ρ** is the average fluid density, **g** is the gravity acceleration, and **h** is the vertical height of the fluid column measured from a datum (Sea level for offshore and the water table for onshore).

However, consideration of the fluid density as average from the multiple aquifers is risky to get inaccurate results. Summary of main properties of the HSP could be listed as: *

- Controlled by brine density (derived from salinity)
- Varies with depth from horizon to horizon – not a straight line
- Usually shown as a straight line
- Reference for determination of overpressure

Correspondence between different types of the water salinity, NaCl ppm, HSP gradients, and equivalent mud weights (EMW) are depicted in Table 1. Therefore, the HSP gradients vary in wide random from 0.433 psi/ft for fresh water to 0.519 psi/ft for saturated brine with relevant NaCl ppm from 0 to more than 300000 values. Hence, an accurate estimation of salinity is a key for precision for HSP prediction.

It is common knowledge in log interpretation practice, there is a triple relationship between salinity, subsurface temperature and apparent resistivity. We can to find any of them due to two others from the famous Schlumberger chart (Fig 2).

However, here a few notes should be mentioned:

- The chart built for chlorine NaClsalinity (CS) only
- For conversion into Total Salinity(TS) the following equation is proposed – TS=CS * 1.657

- In case of other anions and cation some correction coefficients (multiplayers) could be used taken from another chart (Fig.3)

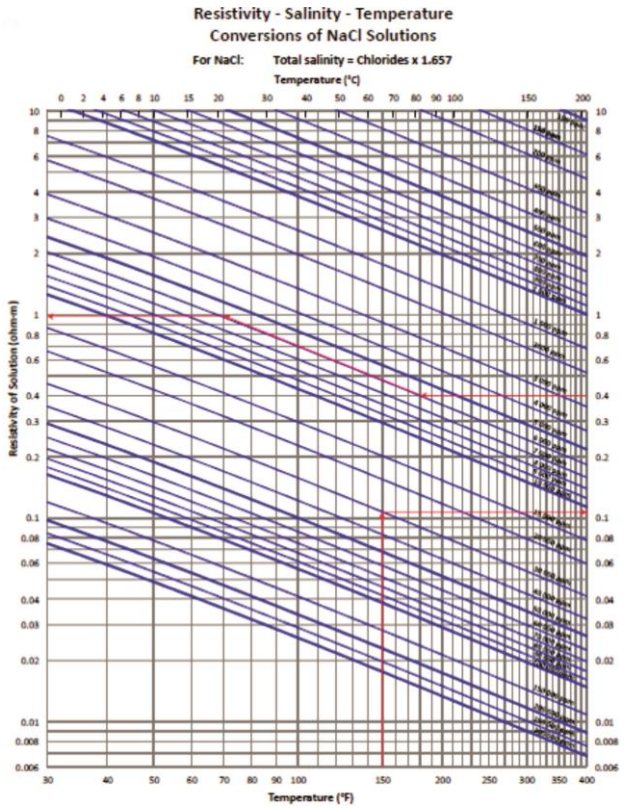

Fig. 2. Schlumberger chart shown the triple relationship between salinity, temperature and resistivity of solution [5].

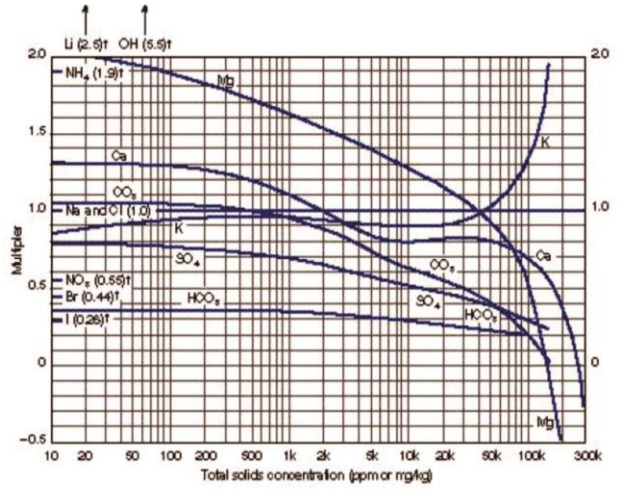

Fig. 3. Multiplayers used for estimation with consideration of different anions and cations additionally to the simple NaCl salinity [5].

Using the Archie's equation for fully water saturated rocks [6] we can estimate the formation water resistivity ($\mathbf{R_w}$) from apparent resistivity estimated from logs ($\mathbf{R_a}$) :

$$R_w = R_a * \varphi^m / a \qquad (2)$$

where φ - porosity, m - cementation exponent, a - tortuosity factor (= 1).

Porosity could be estimated from other logs, e.g. density, neutron porosity, etc. Further, the combination of resistivity, temperature and porosity logs could be proceed to calculate a salinity versus depth log [4, 8]. Alternatively, the formation water resistivity could be estimated from spontaneous potential (**SP**) logs [9].

In order to calculate synthetic salinity from logs, firstly the resistivity logs should be corrected by bringing to the surface temperature condition [14].

The common way to estimate t the conductance difference between any two points along the depth profile is the usage the Arp's equation [10]:

$$R_{w\,T2} = R_{w\,T1} * (T_1 + 21.5) / (T_2 + 21.5) \qquad (3)$$

where $\mathbf{R_{w\ T2}}$ and $\mathbf{R_{w\ T1}}$ are resistivity at depths where temperatures are $\mathbf{T_2}$ **and** $\mathbf{T_1}$**.**

The formation water resistivity ($\mathbf{R_w}$) can in turn be converted into Total Dissolved Solids (TDS), as well as, further into a Chloride Concentration (CC). If the formation water's ionic solution contains salts other than sodium chloride (NaCl) concentration in parts per million, it could be estimated by application of the known multiplier technique [12, 13].

The value of total dissolved solids (**TDS**) can be determined from empirical relationship to the water resistivity ($\mathbf{R_w}$). In case of absent, the empirical relationship the Jorgensen's equation [7] could be used as default for the purpose:

$$TDS = (10000/R_w) * 0.65 \qquad (4)$$

Further TDS logs calculated by the above proposed workflow could be simply transformed into brine density logs and hence by applying some smoothing technique into hydrostatic pressure curves, instead of lines. The proposed approach and described method allow to reach much more accurate calculation of hydrostatic pressure, as an accurate benchmark for overpressure calculation.

III. Application to the South Caspian Basin

The total dissolved solids (TDS) curve can be calibrated by approximating the results of analytical data when the geological section of a field or region contains point by point measurements of TDS.

The accurate quantitative forecast of hydrostatic pressures is reduced to a water density forecast, which in its turn is a forecast of the water salinity composing the section of the horizons.

Thus we receive the real hydrostatic pressure curve that can be used as points for more accurate measurement of abnormally high pore pressures.

The above algorithm was used for calculations based on log charts and pressure data obtained from one of the fields located in the offshore section of the South Caspian basin (Figure 4).

The logging data for the measured apparent resistances were recalculated from the deep temperature conditions to the surface conditions as shown in the first column, where the red line is the apparent resistances, while the blue line is the temperature equivalent resistances recalculated at 25°C.

Temperature curve is shown next to it. Actual temperature measurements in this well were performed simultaneously with measurements of the pressure in the porous horizons of the sediment section. Due to the lack of measurements, the upper part of the temperature curve above 1400 meters was created synthetically by extrapolation to normal conditions, such as 1 atm of pressure and 25°C of surface temperature.

Then the resistance curve was transformed into a synthetic salinity curve based on NaCl. It, in its turn, was converted to total dissolved solids (TDS) curve.

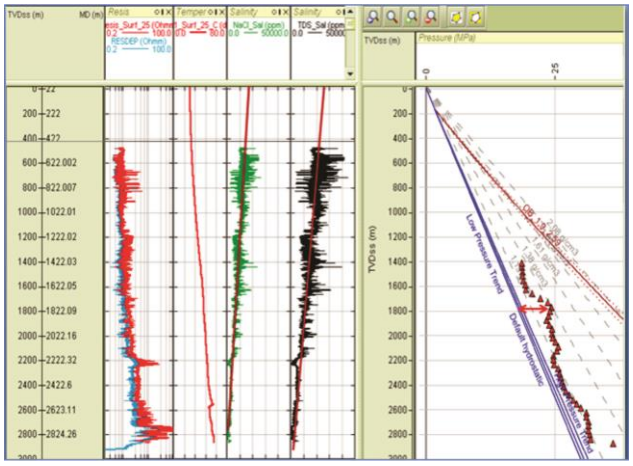

Fig. 4. Composite panel of measured, synthetically calculated log curves, combined with a diagram of pressure changes with depth. The first track shows the calculated apparent pressure (blue) and the pressure recalculated to surface conditions (red). The next track shows the temperature curve generated according to the measured and synthesized on the upper part of the chart. Further, it shows mathematical curves for chloride (NaCl) salinity (green) and total dissolved solids (black). To the right is a pressure diagram with three hydrostatic pressure lines calculated from the mineralization curves. As we can see from this diagram, the same values of measured pressures correspond to different values of overpressure depending on the hydrostatic pressure trend.

III.A. Quantitative Dependence of Hydrostatic Pressure to Hydrogeological Features of the Basin Environment

The water density significantly varies between the basins depending on their salinity, which changes from fresh, river water to sea water and further to hypogene aqueous solution. Moreover, the salinity of subsurface water tends to increase with depth from fresh water to saturated solutions. (Table 1) [1,11,13]. The relationship between different types of natural waters, their total salinity, chloride content, hydrostatic pressure gradients, and equivalent mud values is shown in table 1. Hydrostatic gradients vary greatly, from 0.433 psi/ft for fresh water to 0.519 psi/ft for saturated brines, with corresponding NaCl salinity values over 300,000 ppm.

Table 1. Salinity types and corresponding normal hydrostatic pressures and equivalent mud weight.

Formation Water Types	Salinity Chloride g/litre	NaCl ppm	Normal HS pressure gradient (psi/ft)	Equivalent mud weight (ppg)
Fresh water	0	0	0.433	8.34
Brackish water	12.3	20300	0.438	8.43
Sea water	33	54450	0.448	8.63
Salt water	51.3	84640	0.457	8.80
Typical formation waters	70 110	110000 178900	0.465 0.484	8.96 9.30
Gulf of Mexico	140 170	230000 282500	0.497 0.511	9.56 9.83
Saturated brine	191.6	316150	0.519	9.99

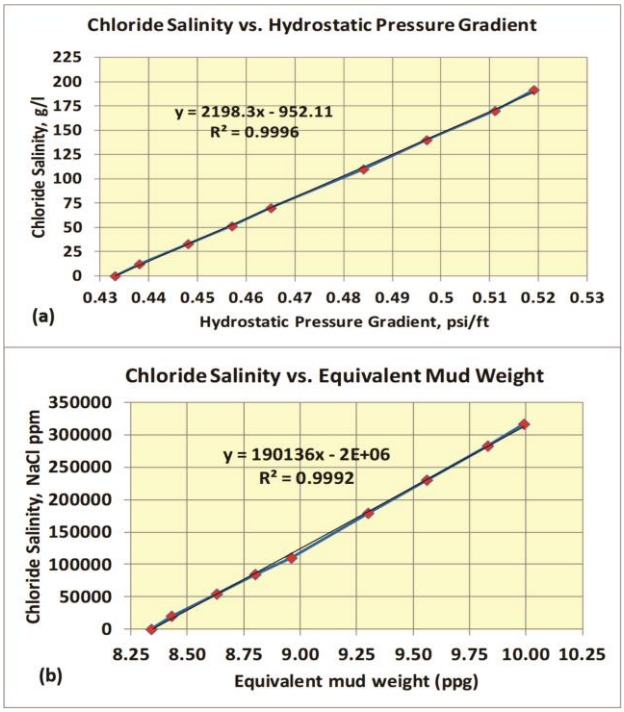

Fig. 5. Diagram of linear relationship between chloride salinity of the basin water, (g/l in (a), NaCl ppm in (b)) and hydrostatic pressure gradients (psi/ft).

The analysis of these data gives us strict empirical patterns between different types of water solutions observed in various geological

environments in a variety of units shown in table 1; such as mineralization units, corresponding pressure gradient units and equivalent mud weight units. However, as we can see from Figures 5 (a) and (b)., there is a fairly clear linear relationship between the hydrostatic pressure gradients and the salinity of different types of water, and the hydrostatic pressure gradients they generate; and this natural relationship is explained quite simply - the higher the mineralization, the higher the specific density of solutions and, hence, the hydrostatic pressure gradients that they create. The same linear relationship is observed between the types of salinity and the values expressed in equivalent values of the drilling mud. (Figures 6 (a) and (b)).

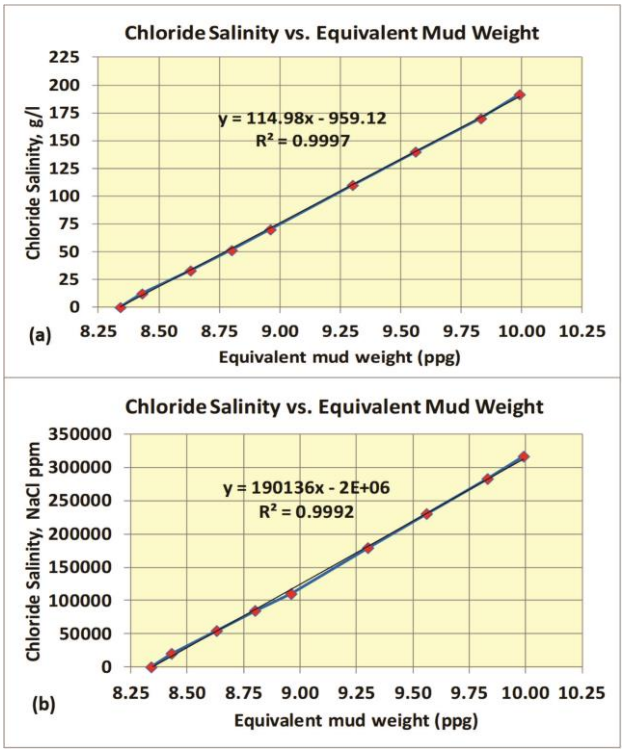

Fig. 6. Diagram of linear relationship between chloride salinity of the basin water, (g/l in (a), NaCl ppm in (b)) and Equivalent Mud Weight (ppg).

III.B. Hydrostatic Pressure Forecast for Various South Caspian Basin Zones Based on Proposed Method

In fact, the gradients of basin hydrostatic pressure are far from simplified linearity, they actually vary with depth depending on changes in mineralization, as well as the salinity of subsoil aquatic solutions that determine their density and, hence the hydrostatic pressure gradients. Thus, the accurate quantitative forecast of hydrostatic pressures is reduced to a water density forecast, which in its turn is a forecast of the water salinity composing the section of the horizons. For example, in some basins, the cross section of deposits in the South Caspian basin, shows the intervals of reverse or cyclic mineralization. Hence, the hydrostatic pressure curves in these basin zones are complex and ambiguous. Salinity fluctuation and hydrostatic pressure charts were produced based on the literature data [15] for measured water salinities from different horizons of the sediment section, which included both the gradient values and equivalent values of the drilling mud. The data was analyzed and used targeted to the following zones of the South Caspian Basin:

- Gabyrry-Ajinour zone
- Yevlakh-Agjabedi Trough zone
- Lower Kurian depression zone
- Gobustan-Absheron zone

At the same time, the salinity data were analyzed in detail against the available studied salinity values for individual stratigraphic horizons. The horizons in the developed and below listed drawings are shown and numbered in ascending order from top to bottom in accordance with their stratigraphic sequence as follows:

1. Quaternary deposits
2. Absheron deposits
3. Agchagil deposits
4. Productive strata sediments
5. Pontian deposits
6. Sarmat deposits
7. Chokrak deposits
8. Maykop deposits
9. Eocene deposits
10. Upper Cretaceous deposits
11. Lower Cretaceous deposits

Data in Table 2 describes average, minimum and maximum salinity values for the most impressive horizons that have such information [15]. Next, the water type is indicated by the quantitative values of the largest cation and anion, and then the hydrostatic pressure parameters calculated from the average salinity values, such as their gradients and the corresponding equivalent values of the drilling mud gradients.

The various basin water salinity trend diagrams were prepared on the basis of these data and according to their stratigraphic affiliation and related approximate depth.

As we can see from Figure 7, the salinity of section water is not too high, in some places it is reversing and cyclic; maximum values are observed in Absheron deposits of the section

followed by Sarmat and Lower Cretaceous deposits. Minimum amount of salinity is observed in the Pontian and Eocene deposits. Trend charts for hydrostatic pressure gradients of various horizons are shown in Figure 8. This chart is developed on the basis of the calculated average salinity values obtained through analytic determination and described in Table 2.

Table 2. Salinity types of basin brines in different SCB horizons and corresponding average, minimum and maximum values of normal hydrostatic pressures and equivalent drilling mud weights

No	Stratifraphic age, Horizons	Subbasins and regions	Avarage mineralisation, g/l	Minimal mineralisation, g/l	Maximal mineralisation, g/l	Brine type	Average Hydrostatic Pressure Gradient, psi/ft	Minimal Hydrostatic Pressure Gradient, psi/ft	Maximal Hydrostatic Pressure Gradient, psi/ft	Avarage HSP gradients in EMW, ppg	Minimal HSP gradients in EMW, ppg	Maximal HSP gradients in EMW, ppg
1	Quatenary	Low Kurian	36.8	13.3	57.9	$-Cl, Ca^{+}$	0.4499	0.4392	0.4595	8.66	8.46	8.85
2	Absheronian	Low Kurian	35.7	1.2	113.2	$-Cl, Ca^{+}$	0.4494	0.4337	0.4846	8.65	8.35	9.33
3	Akchagilian	Low Kurian	31.4	9	82.6	$-Cl, Ca^{+}$	0.4474	0.4372	0.4707	8.61	8.42	9.06
4	Productive Series	Gobustan - Absheron	16.8	7	54.3	$-Cl, Ca^{+}$	0.4408	0.4363	0.4578	8.49	8.40	8.81
5	Pontian	Gobustan - Absheron	13	12	16	$-Cl, Na^{+}$	0.4390	0.4386	0.4404	8.45	8.45	8.48
6	Sarmatian	Evlakh - Agjabedi	45.6	24.1	73.5	HCO_3^{-}, Na^{+}	0.4539	0.4441	0.4665	8.74	8.55	8.98
7	Chockrakian	Evlakh - Agjabedi	28.5	15.6	54.6	$-Cl, Ca^{+}$	0.4461	0.4402	0.4579	8.59	8.48	8.82
8	Maykopian	Evlakh - Agjabedi	13.4	6	54.6	$-Cl, Ca^{+}$	0.4392	0.4358	0.4579	8.46	8.39	8.82
9	Eocene	Evlakh - Agjabedi	21.3	6.6	21.6	$-Cl, Ca^{+}$	0.4428	0.4361	0.4429	8.53	8.40	8.53
10	Upper Cretaceous	Evlakh - Agjabedi	16.9	5.4	34.5	$-Cl, Ca^{+}$	0.4408	0.4356	0.4488	8.49	8.39	8.64
11	Low Cretaceous	Evlakh - Agjabedi	49.1	29.9	65.7	$-Cl, Ca^{+}$	0.4554	0.4467	0.4630	8.77	8.60	8.91

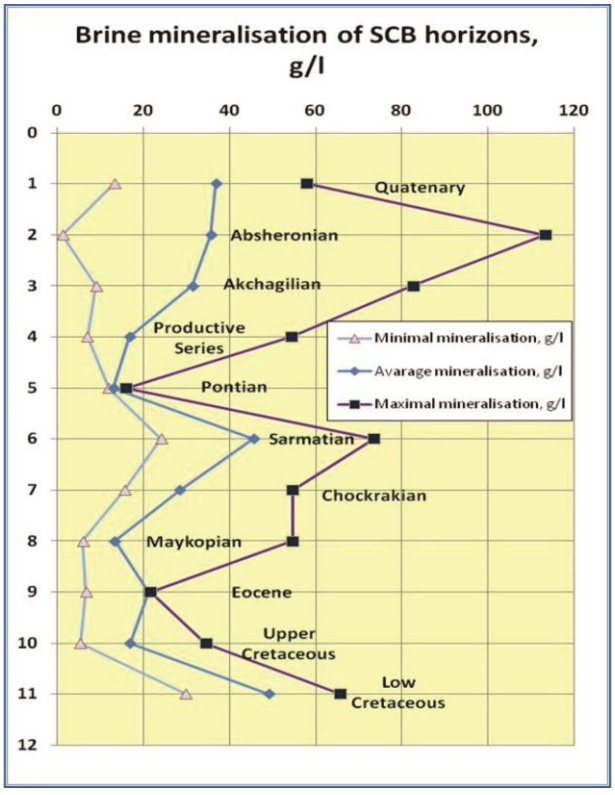

Fig. 7. Salinity types of reservoir brines in the SCB reservoir horizons and their corresponding average, minimum and maximum salinity values.

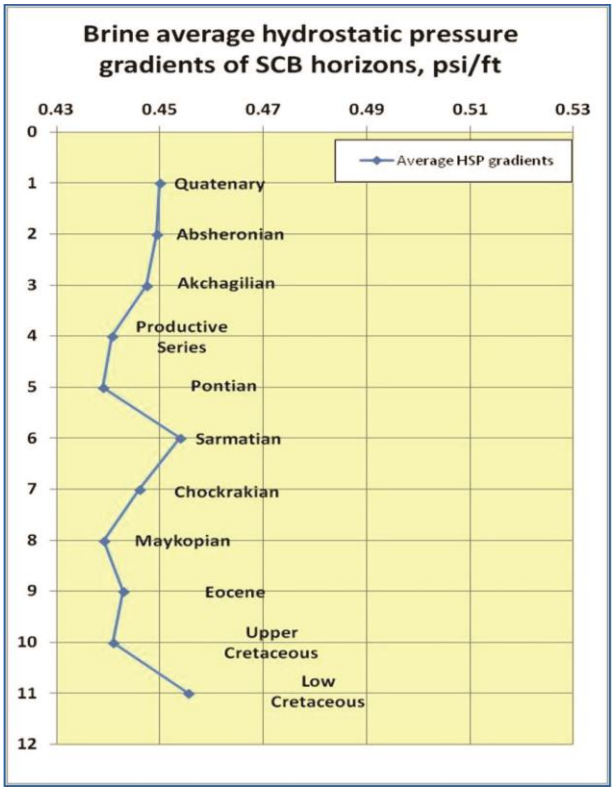

Fig. 8. Average gradient chart of hydrostatic pressures in various horizons of the SCB.

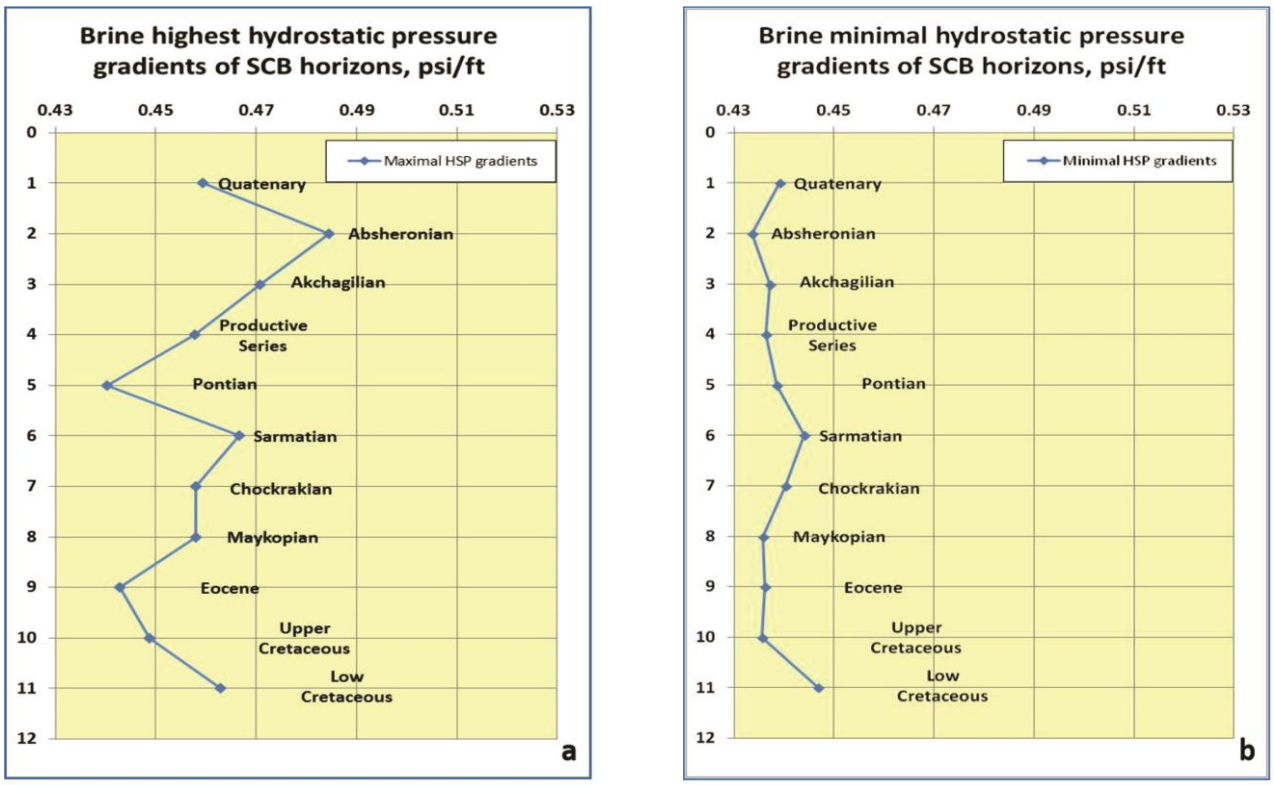

Fig. 9 (a) and (b). Maximum gradient (a) and minimum gradient (b) charts of hydrostatic pressures in various horizons of the SCB.

As it can be seen from this figure, average value of these gradients reduces on the top of the sedimentary section from the Quaternary to Pontian deposits. Two relatively small jumps are observed in Sarmat and Lower Cretaceous deposits. In general, average values do not have high or off the scale values. However, maximum values observed in Absheron, Sarmat and Lower Cretaceous deposits are slightly conservative. Hydrostatic pressure gradients calculated according to these conservative values have respective highest values and are presented in Figure 9(a).

As we can see from Figure 9(a), the maximum values of these gradients in Absheron deposits reach 0.4846 psi/ft, which is significantly higher than the values in other horizons. In this case, the equivalent maximum gradient values expressed in mud units reach 9.33 ppg, which can complicate drilling, especially in cases if the minimum values dominate in overlaying and underlying horizons. (Figure 9(b))

As we can see from Figure 9(b), the minimum hydrostatic pressure values calculated considering statistical minimum salinity are close to freshwater values and, most likely, this is the influence of surface, river and lake waters. Therefore, their average and maximum values should be forecasted during well laying and drilling using above proposed method.

Average, minimum and maximum values of hydrostatic pressure expressed in terms of equivalent mud weight (ppg) are given in Figure 10.

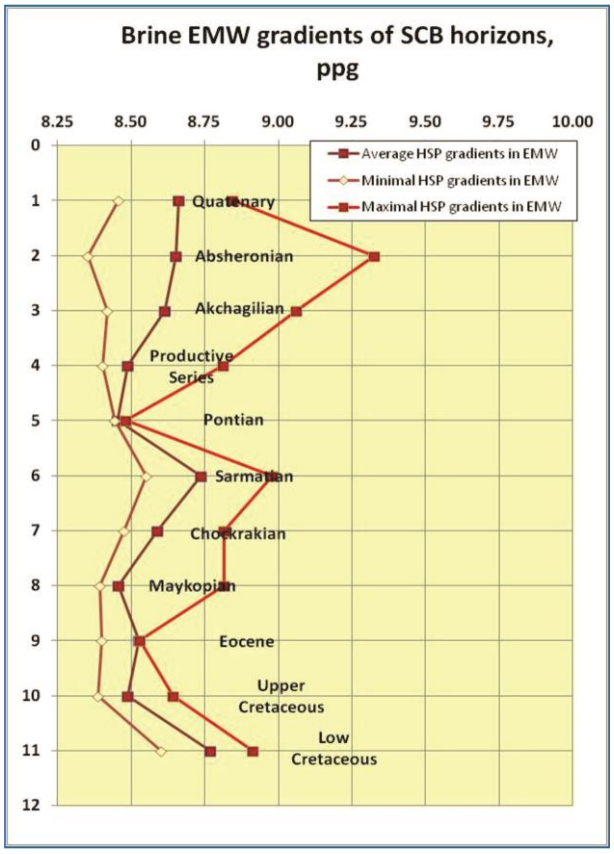

Fig. 10. Trend chart for calculated average, minimum and maximum values of hydrostatic pressure expressed in terms of equivalent specific weight for various SCB horizons.

IV. Prediction and Calculation of Hydrostatic Pressures in Various Horizons of the Gabyrry-ajinour Zone of the CSB

Gabyrry-Ajinour zone is located in the north-west part of the SCB. The most famous oil deposit here is the Tarsdallar field in the volcanogenic sedimentary rocks. Drilling of the first wells in this region revealed certain drilling problems. Therefore, gradients of normal hydrostatic pressures in this region are crucial especially for correct calculations during the drilling through near-surface and lower volcanic-sedimentary deposits. In the Gabyrry-Ajinour zone of the SCB, brine mineralization in permeable horizons has a specific feature to change with the depth.

As it can be seen from Figure 11, the cross section of this zone contains three mineralization variation ranges.

Average and maximum values of upper Quaternary to Sarmat deposits gradually increase from 1.05 g/l to almost 38 g/l (average) and from 1.1 g/l to almost 73.3 g/l (maximum).

Such sequential change in mineralization in this region refers to a similar change in hydrostatic pressure gradients from slightly salted river values of 0.4436 psi /ft to noticeably high values of 0.45 psi/ft (average) and 0.466 psi /ft (maximum) (Table 3 and Fig.12). Lower values in this interstream zone are easily explained by the impact of the fluvial factor on formation of water in the Quaternary and other deposits surfacing and gaining from the atmospheric precipitation in some places.

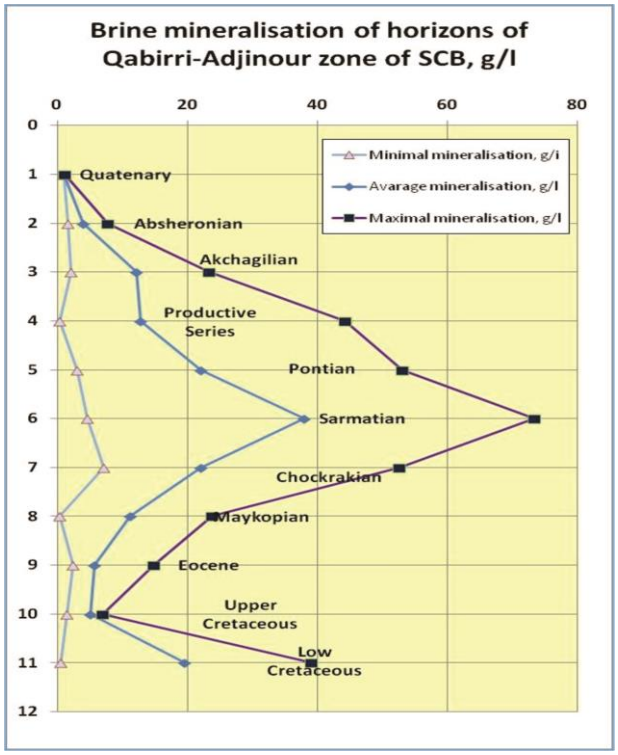

Fig. 11. Trend chart for average, minimum and maximum salinity values in various horizons of the SCB Gabyrry-Ajinour zone.

Table 3. Salinity types of basin brines in different horizons of Gabyrry-Ajinour zone of the SCB and corresponding average, minimum and maximum values of normal hydrostatic pressures and equivalent drilling mud weights.

No	Stratifraphic age, Horizons	Avarage mineralisation, g/l	Minimal mineralisation, g/l	Maximal mineralisation, g/l	Brine type	Avarage Hydrostatic Pressure Gradient, psi/ft	Minimal Hydrostatic Pressure Gradient, psi/ft	Maximal Hydrostatic Pressure Gradient, psi/ft	Avarage HSP gradients in EMW, ppg	Minimal HSP gradients in EMW, ppg	Maximal HSP gradients in EMW, ppg
1	Quatenary	1.05	1.02	1.1	$-Cl, Na^+$	0.4336	0.4336	0.4336	8.35	8.35	8.35
2	Absheronian	4	1.6	7.7	HCO_3^-, Na^+	0.4349	0.4338	0.4366	8.38	8.36	8.41
3	Akchagilian	12.1	2.1	23.3	$-Cl, Ca^+$	0.4386	0.4341	0.4437	8.45	8.36	8.54
4	Productive Series	12.8	0.4	44.2	$-Cl, Ca^+$	0.4389	0.4333	0.4532	8.45	8.35	8.73
5	Pontian	22	3	53	$-Cl, Ca^+$	0.4431	0.4345	0.4572	8.53	8.37	8.80
6	Sarmatian	37.9	4.6	73.3	$-Cl, Ca^+$	0.4504	0.4352	0.4665	8.67	8.38	8.98
7	Chockrakian	22	7.1	52.5	HCO_3^-, Na^+	0.4431	0.4363	0.4570	8.53	8.40	8.80
8	Maykopian	11.3	0.4	23.8	HCO_3^-, Na^+	0.4383	0.4333	0.4439	8.44	8.35	8.55
9	Eocene	5.8	2.5	14.8	$-Cl, Ca^+$	0.4358	0.4342	0.4398	8.39	8.36	8.47
10	Upper Cretaceous	5.03	1.5	7	$-Cl, Ca^+$	0.4354	0.4338	0.4363	8.39	8.35	8.40
11	Low Cretaceous	19.5	0.6	39	$-Cl, Ca^+$	0.4420	0.4334	0.4509	8.51	8.35	8.68

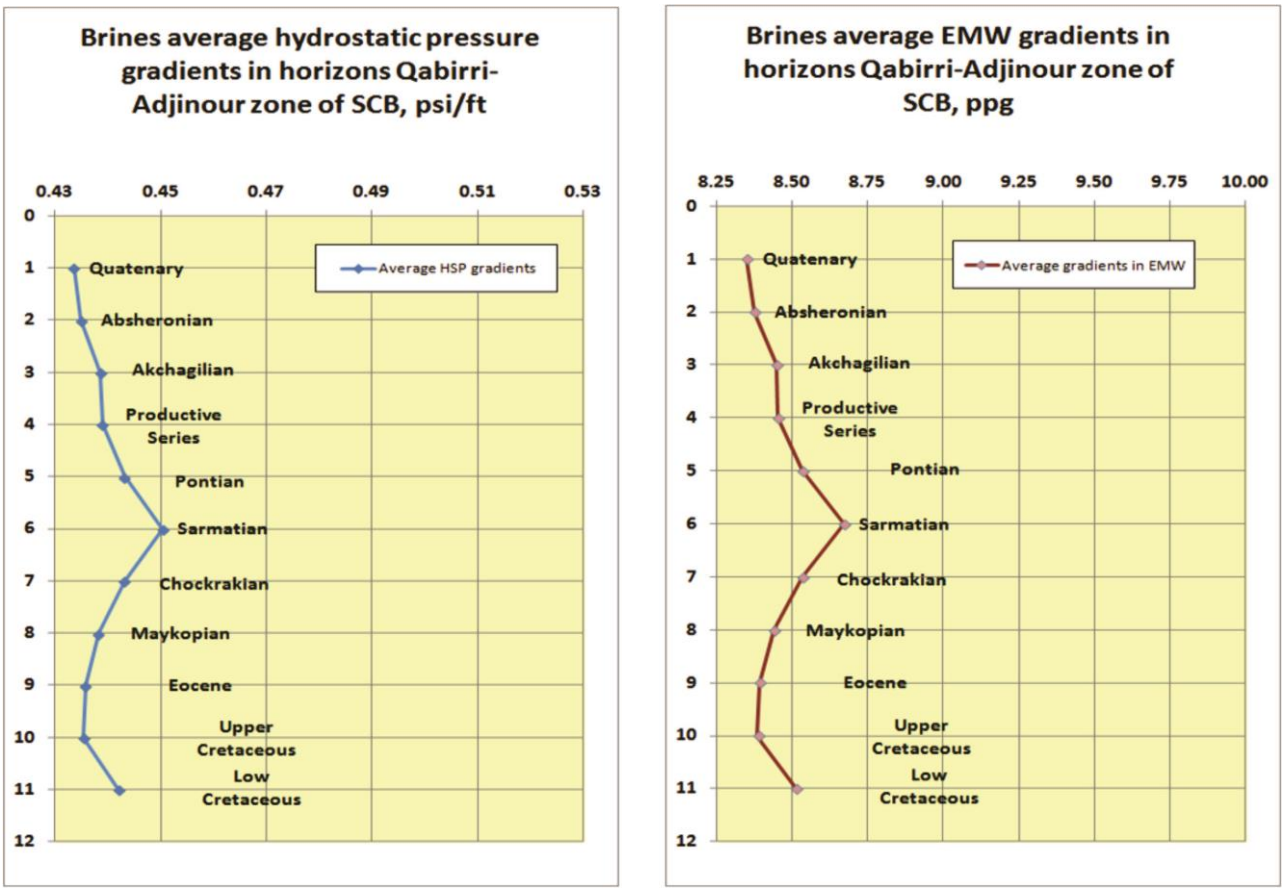

Fig. 12. Chart of average values of hydrostatic pressures and EMW gradients in various horizons of Gabyrry-Ajinour zone of the SCB.

The second clearly distinguished interval in this region shall include the section from the Sarmatian to the upper Cretaceous deposits inclusive. The section shows stable salinity regression and resulting density of the ground water and related hydrostatic features. Within the first ten horizons the salinity reduces to the value variation range expressed in 1.5; 5; 7 g/l respectively.

And finally, the lowest part of the cross section of Cretaceous age horizons again indicates increase in mineralization values up to 20 g / l (average) and 40 g / l (maximum).

If the difference in the direction of salinity variation in the first two intervals can be explained by the hydrogeological evolution of the SCB zones, then the change in the salinity of the Cretaceous deposits requires an appropriate explanation.

Such mineralization profile creates a correspondingly similar contrasting profile of hydrostatic pressures in this region, both in the gradient and equivalent values of the drilling mud.

Modelling of the underground pressure evolution and overpressure risks used during the geological design of the wells drilled in Gabyrry-Ajinour zone of the basins was based not on linear, but on dog-leg hydrostatic pressure model, where each area is included in the model in parts and in accordance with values described in Table 3.

V. Prediction and Calculation of Hydrostatic Pressures in Various Horizons of Yevlakh-Agjabedi Region of the SCB

Yevlakh-Agjabedi trough area is one of the most studied regions of the South Caspian basin. This region includes such impressive oil fields like Muradkhanli and Zardob covering eroded volcanic and volcanic-sedimentary deposits of the upper Cretaceous, Eocene and Maikop age. The first wells drilled in Muradkhanly field indicated high oil rate produced from the horizons with high formation pressure in this region and other problems related to the well drilling.

As it can be seen from Figure 13, the cross section of this trough contains more complex picture of changes in mineralization along the horizons.

Available salinity data for this trough start from Agchagil deposits. If minimum and average values increase gradually from freshwater 0.42 g/l to up to almost 36 g/l (minimum) and from 22.3 g/l to up to almost 45.6 g/l (average), the maximum values indicating maximum salinity (129.8 g/l) in Agchagil deposits reduce to 44.9 in productive strata sediments.

Further the basin cross section reflects overall reduction of salinity from 45.6 g/l to almost 16.9 g/l (average values) and from 73.5 g/l to almost 21.6g/l (maximum values) from Sarmatian

towards Eocene and Upper Cretaceous deposits (Figure 13).

Such irregular changes of the salinity in this region, namely gradual changes in average and minimum values on one hand and abrupt changes in maximum values on the other hand, reflect the changes in hydrostatic pressure gradients from almost fluvial values of 0.443 psi/ft to significantly higher maximum values of 0.4921 psi/ft (Table 4 and Fig. 13). Lower values in this trough zone are easily explained by the impact of the fluvial factor on formation of water in the upper deposits surfacing and gaining from the atmospheric precipitation in some places. While the high maximum values of Agchagil horizon requires additional studies.

Table 4. Salinity types of basin brines in different horizons of the Yevlakh-Agjabedi trough of the SCB and corresponding average, minimum and maximum values of normal hydrostatic pressures and equivalent drilling mud weights.

No	Stratifraphic age, Horizons	Avarage mineralisation, g/l	Minimal mineralisation, g/l	Maximal mineralisation, g/l	Brine type	Avarage Hydrostatic Pressure Gradient, psi/ft	Minimal Hydrostatic Pressure Gradient, psi/ft	Maximal Hydrostatic Pressure Gradient, psi/ft	Avarage HSP gradients in EMW, ppg	Minimal HSP gradients in EMW, ppg	Maximal HSP gradients in EMW, ppg
1	Quatenary										
2	Absheronian										
3	Akchagilian	22.3	0.42	129.6	$^{-}Cl, Ca^{+}$	0.4433	0.4333	0.4921	8.54	8.35	9.47
4	Productive Series	38.14	36	44.9	$^{-}Cl, Ca^{+}$	0.4505	0.4495	0.4535	8.67	8.65	8.73
5	Pontian	40	32	62	$^{-}Cl, Ca^{+}$	0.4513	0.4477	0.4613	8.69	8.62	8.88
6	Sarmatian	45.6	24.1	73.5	HCO_3^{-}, Na^{+}	0.4539	0.4441	0.4665	8.74	8.55	8.98
7	Chockrakian	28.5	15.6	54.6	$^{-}Cl, Ca^{+}$	0.4461	0.4402	0.4579	8.59	8.48	8.82
8	Maykopian	13.4	6	54.6	$^{-}Cl, Ca^{+}$	0.4392	0.4358	0.4579	8.46	8.39	8.82
9	Eocene	21.3	6.6	21.6	$^{-}Cl, Ca^{+}$	0.4428	0.4361	0.4429	8.53	8.40	8.53
10	Upper Cretaceous	16.9	5.4	34.5	$^{-}Cl, Ca^{+}$	0.4408	0.4356	0.4488	8.49	8.39	8.64
11	Low Cretaceous	49.1	29.9	65.7	$^{-}Cl, Ca^{+}$	0.4554	0.4467	0.4630	8.77	8.60	8.91

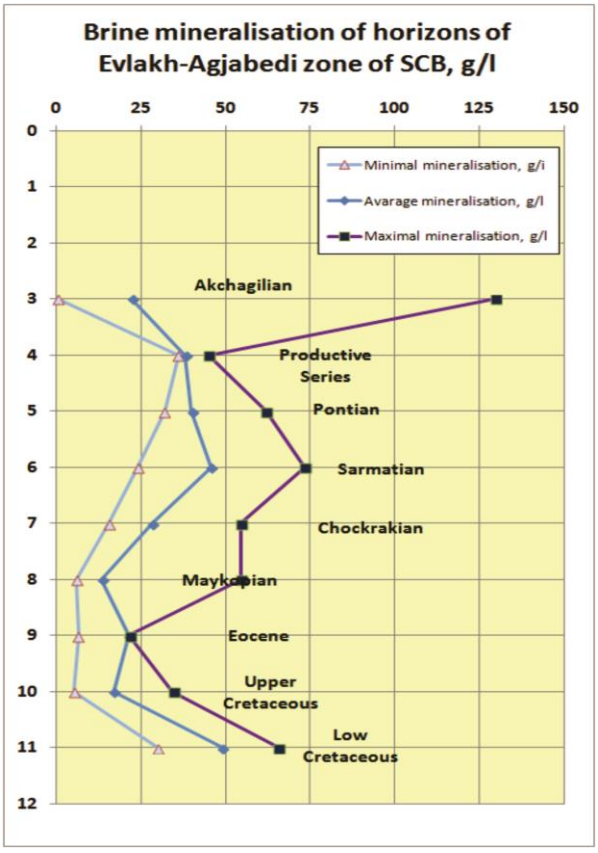

Fig. 13. Trend chart for average, minimum and maximum salinity values in various horizons of the SCB Yevlakh-Agjabedi trough.

Further harmonic increase of salinity in all three curves describing upper section of Sarmat deposits repeats general picture of changes all over the basin. The salinity and related density of ground water and associated hydrostatic parameters reduces from Sarmatian downward to the Eocene and Upper Cretaceous deposits, Salinity reduces till the values of the variation range - 5.4; 16.9 and 34.5 g/l respectively.

And the lowest part of the cross section of Cretaceous age horizons again indicates increase in mineralization values up to 29.9 g/l (minimum), 49.1 g/l (average) and 65.7 g/l (maximum).

Upon conditional exclusion of the difference in maximum values of Agchagil deposits, the variation of the salinity in the remaining section can be explained by the common hydro-geological evolution of this zone located in the western part of the SCB.

Such mineralization profile creates a correspondingly similar contrasting profile of hydrostatic pressures in this region, both in the gradient and equivalent values of the drilling mud.

The geological design of the new wells to be drilled in Yevlakh-Agjabadi trough shall consider the modelling of the evolution of underground pressure and AHP risks based on such non-linear model of hydrostatic pressure in accordance with values described in Table 4 and Figure 14.

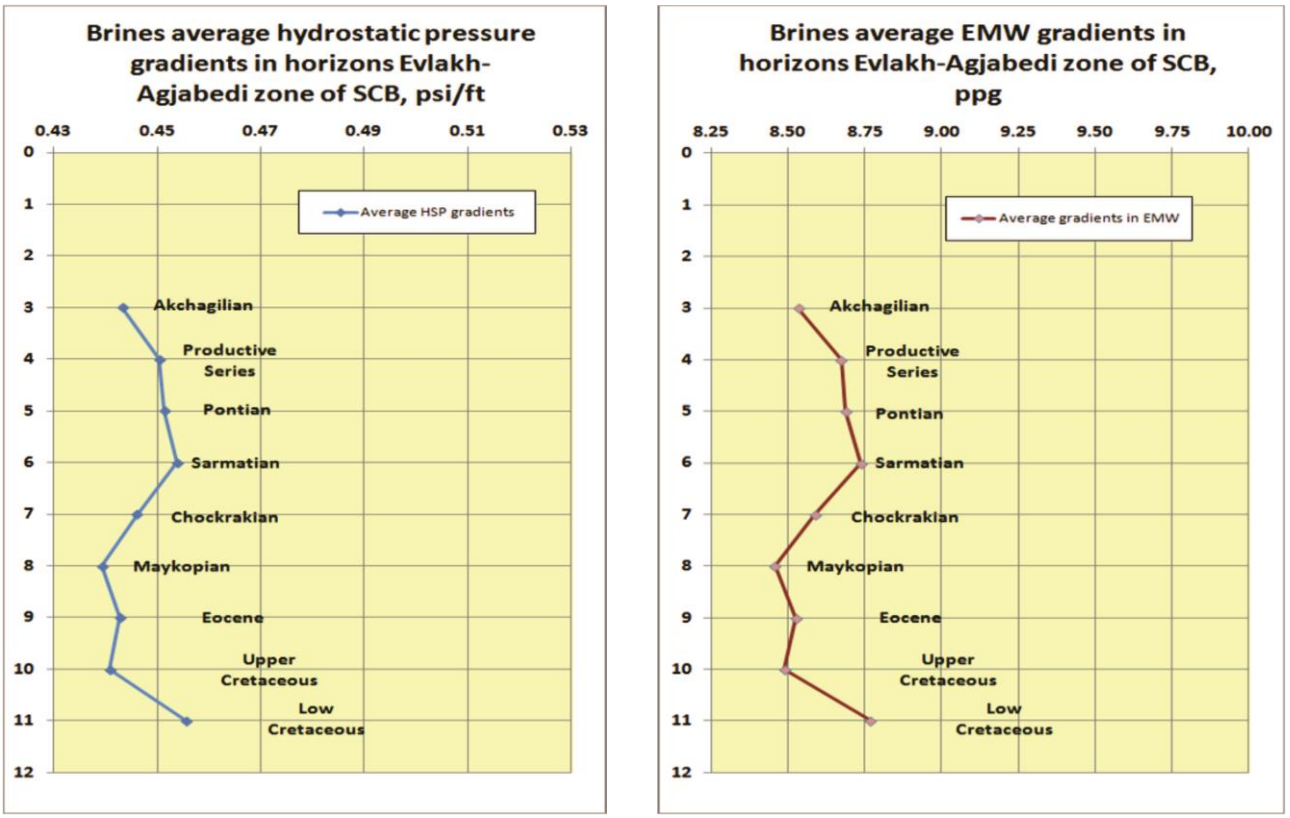

Fig. 14. Chart of average values of hydrostatic pressures in various horizons of Yevlakh-Adjabedy Trough of the SCB.

VI. Prediction and Calculation of Hydrostatic Pressures in Various Horizons of Low Kurian Area of the SCB

Prediction and calculation of hydrostatic pressures in various horizons of Low Kurian area of the SCB.

Low Kurian area is one of the most unique and studied regions of the South Caspian basin. However, there are quite a number of unstudied matters concerning the relationship between various structural stages of this unique trough.

The well-known and impressive oil deposits in the sandy-clay reservoirs of productive strata, like Kurovdag, Khilly and others are located here. Drilling of wells in these fields and in this region, in general, revealed formations with different pressure values. In number of cases, formation pressures of oil-bearing horizons were interpreted as abnormally low, while the others were accepted as excessive.

Therefore, the correct calculation of normal hydrostatic pressures in the horizons of the Low Kurian trough deposits section will allow avoiding a false interpretation of the anomalous pressures of this region.

As we can see from Table 5 and Figure 15, water salinity data for this region include only Upper Pliocene - Quaternary sediment complex. This is due to the more submerged structure of the trough and, as a result, drilling of only upper part of the section.

Available salinity data for this trough start from Quaternary deposits. Here the minimum and average values of salinity increase gradually from slightly higher freshwater 9 g/l to up to almost 14.7 g/l (minimum) and from 31.4 g/l to up to almost 38.5 g/l (average). Thus indicating relatively stable salinity of the deposit, the maximum values show maximum salinity (113.2 g/l) in Absheron deposits, which reduce to 74.7 in Productive Series sediments. (Fig. 15)

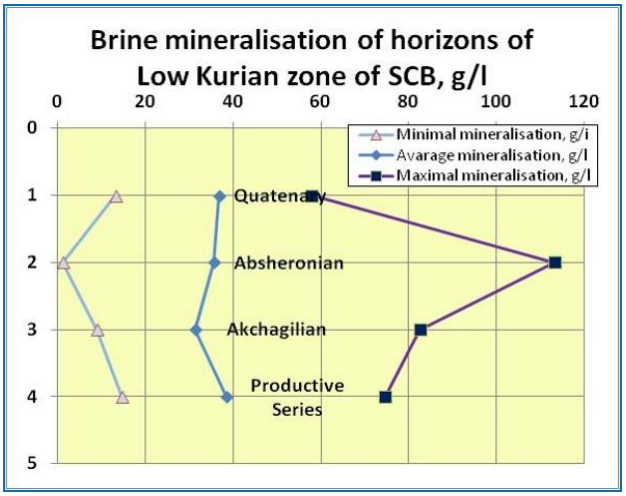

Fig. 15. Trend chart for average, minimum and maximum salinity values in various horizons of the SCB Low Kurian trough.

Such relatively negligent changes in average salinity values in this region indicate the possibility of relatively stable gradients and linear changes in its hydrostatic pressure from freshwater values of 0.447 psi/ft up to 0.4506 psi/ft (Table 5 and Figure 15). Also lower values in this trough zone are explained by the impact of the fluvial factor on formation of water in the upper deposits surfacing and gaining from the atmospheric precipitation in some places. While the high maximum values (0.4846 psi/ft) of Absheron horizon requires additional studies.

Comparative analysis of salinity data and corresponding pressures of this trough with the available data for the western regions of Azerbaijan indicates different pressure profiles, which can be explained by different hydrogeological evolution of these zones in the western edge of the SCB.

Table 5. Salinity types of basin brines in different horizons of the Low Kurian trough of the SCB and corresponding average, minimum and maximum values of normal hydrostatic pressures and equivalent drilling mud weights.

No	Stratifraphic age, Horizons	Avarage mineralisation, g/l	Minimal mineralisation, g/l	Maximal mineralisation, g/l	Brine type	Avarage Hydrostatic Pressure Gradient, psi/ft	Minimal Hydrostatic Pressure Gradient, psi/ft	Maximal Hydrostatic Pressure Gradient, psi/ft	Avarage HSP gradients in EMW, ppg	Minimal HSP gradients in EMW, ppg	Maximal HSP gradients in EMW, ppg
1	Quatenary	36.8	13.3	57.9	$^{-}Cl, Ca^{+}$	0.4499	0.4392	0.4595	8.66	8.46	8.85
2	Absheronian	35.7	1.2	113.2	$^{-}Cl, Ca^{+}$	0.4494	0.4337	0.4846	8.65	8.35	9.33
3	Akchagilian	31.4	9	82.6	$^{-}Cl, Ca^{+}$	0.4474	0.4372	0.4707	8.61	8.42	9.06
4	Productive Series	38.5	14.7	74.7	$^{-}Cl, Ca^{+}$	0.4506	0.4398	0.4671	8.68	8.47	8.99

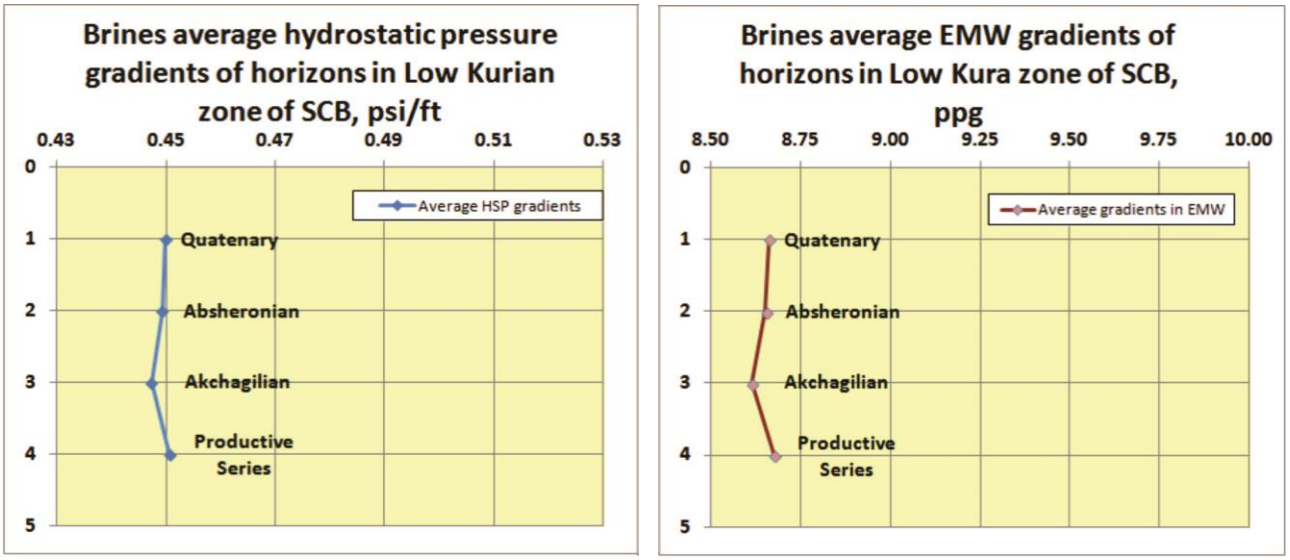

Fig. 16. Average value chart of hydrostatic pressures in various horizons of Low Kurian trough of the SCB.

This mineralization profile creates a correspondingly similar stable profile of hydrostatic pressures in this region, both in the gradient and equivalent values of the drilling mud.

The geological design of the new wells to be drilled in Low Kurian trough shall consider the modelling of the evolution of underground pressure and AHP risks based on such detected model of hydrostatic pressure in accordance with values described in Table 5 and Figures 15 and 16.

VII. Prediction and Calculation of Hydrostatic Pressures in the Basins of Various Horizons of Gobustan-Absheron Zone

Gobustan-Absheron zone of Azerbaijan is one of the complex geological regions of the South Caspian Basin. The region contains the largest number of the oil-bearing deposits of the country.

Notwithstanding the large quantity of drilled wells, the drilling in this region still presents surprises, which requires re-drilliing of complicated and unsuccessful sections. Gobustan

part of the region and deeper sections of the Absheron region have considerable number of unstudied issues mainly related to the relationship of various structural floors of this unique oil-bearing region.

The drilling opened stratigraphically older deposits in the sandy-clay reservoirs of productive strata in Gobustan section of the region than in Absheron region. Drilling of wells in these fields and in this region, in general, revealed formations with different pressure values.

Therefore, the correct calculation of normal hydrostatic pressures in the horizons of the deposit section of this region allows more effectively exploration drilling in this formations.

The water salinity data for this region and calculated hydrostatic pressure gradients are shown in Table 6.

Table 6. Salinity types of basin brines in different horizons of Gobustan-Absheron zone of the SCB and corresponding average, minimum and maximum values of normal hydrostatic pressures and equivalent drilling mud weights.

No	Stratifraphic age, Horizons	Avarage mineralisation, g/l	Minimal mineralisation, g/l	Maximal mineralisation, g/l	Brine type	Avarage Hydrostatic Pressure Gradient, psi/ft	Minimal Hydrostatic Pressure Gradient, psi/ft	Maximal Hydrostatic Pressure Gradient, psi/ft	Avarage HSP gradients in EMW, ppg	Minimal HSP gradients in EMW, ppg	Maximal HSP gradients in EMW, ppg
1	Quatenary										
2	Absheronian										
3	Akchagilian										
4	Productive Series	16.8	7	54.3	$^{-}Cl, Ca^{+}$	0.4408	0.4363	0.4578	8.49	8.40	8.81
5	Pontian	13	12	16	$^{-}Cl, Na^{+}$	0.4390	0.4386	0.4404	8.45	8.45	8.48
6	Sarmatian	45.6	24.1	73.5	HCO_3^{-}, Na^{+}	0.4539	0.4441	0.4665	8.74	8.55	8.98
7	Chockrakian	32.1	17	53	$^{-}Cl, Ca^{+}$	0.4477	0.4408	0.4572	8.62	8.49	8.80
8	Maykopian	10.3	5.6	12.8	HCO_3^{-}, Na^{+}	0.4378	0.4357	0.4389	8.43	8.39	8.45
9	Eocene	8.5	4	11	HCO_3^{-}, Na^{+}	0.4370	0.4349	0.4381	8.42	8.38	8.44
10	Upper Cretaceous	3.5	2.7	4.2	HCO_3^{-}, Na^{+}	0.4347	0.4343	0.4350	8.37	8.37	8.38
11	Low Cretaceous										

As we can see from this table and salinity trend chart for formation water opened by horizon drilling developed according to these data (Figure 20) the cross section of these horizons indicate the following changes in salinity profile.

The literary sources [ ] do not contain mineralization data for overlying deposits from Quaternary to Akchagyl inclusive. Average and maximum values of salinity sharply decreases from productive strata sediments towards Pontian deposits up to 13-16 g/l. Further towards to the section of Sarmat deposits the salinity sharply increases in all three observed curves up to 24.1 g/l (minimum), 45.6 g/l (average) and up to almost 73.5 g/l (maximum). This maximum Sarmatian salinity observed in number of regions also repeated in the Gobustan-Absheron region.

Further all three curves of minimum, average and maximum salinity values show stable regression that develops till Upper Cretaceous deposits, where the minimum values reduce to 2.7 g/l, average - to 3.5 g/l and maximum - to 4.2 g/l. (Fig. 17).

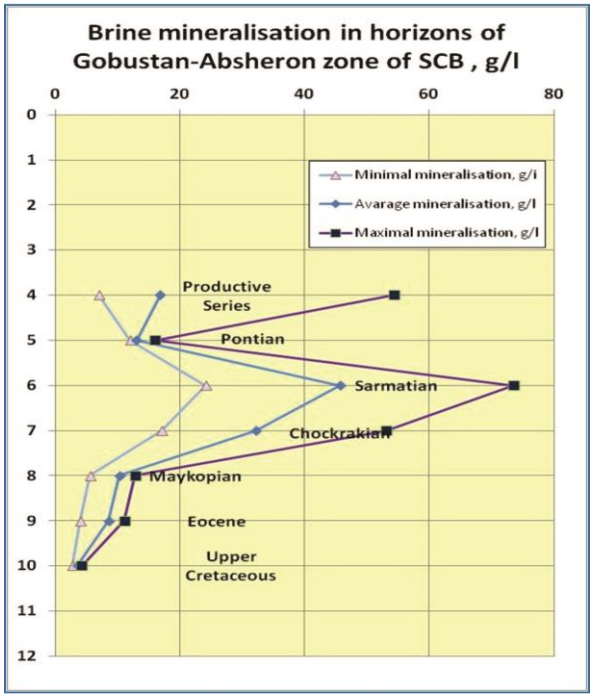

Fig. 17. Trend chart for average, minimum and maximum salinity values in various horizons of the SCB Gobustan-Absheron Region.

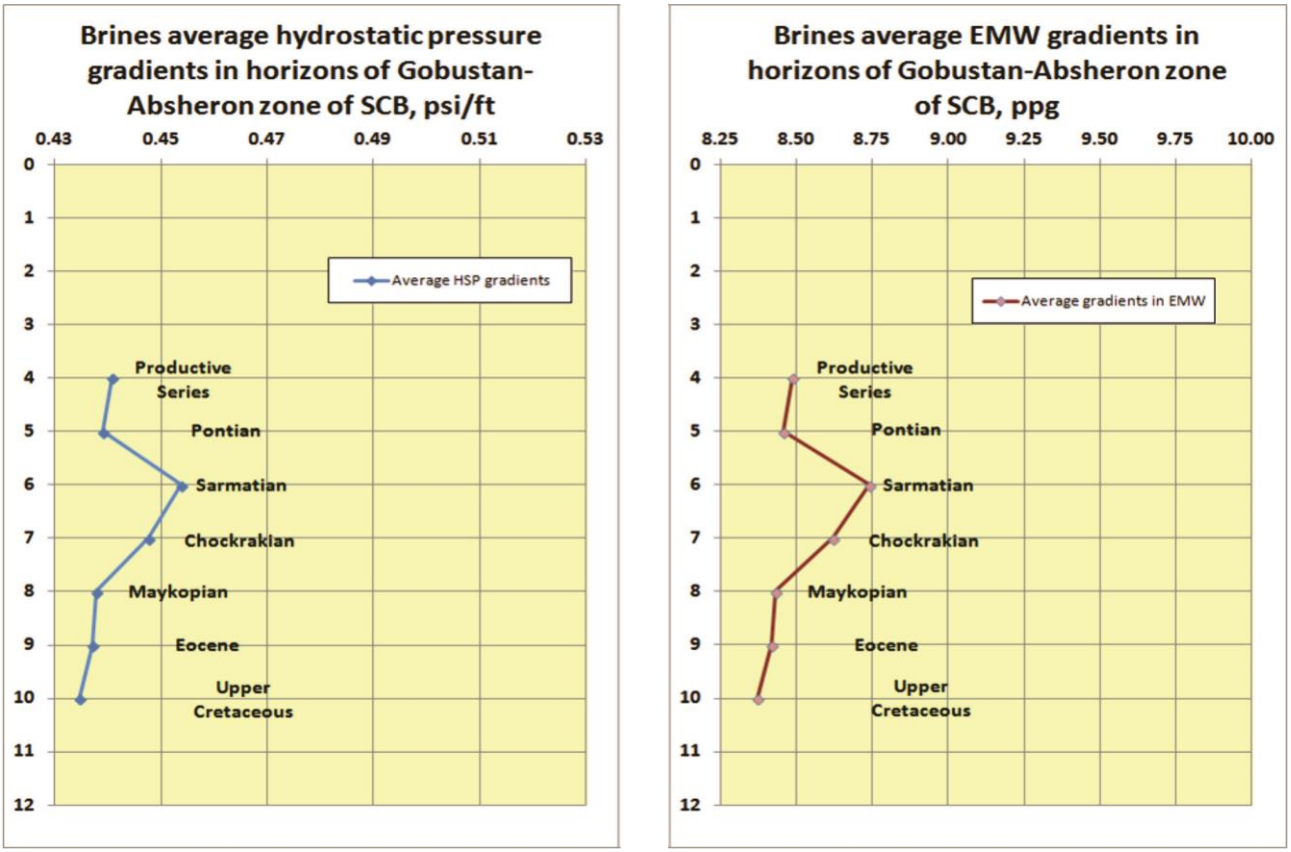

Fig. 18. Average values chart of hydrostatic pressures in various horizons of Gobustan-Absheron Region of the SCB.

Such change in salinity in the region shows the similar changes in hydrostatic pressure gradients. In general, except the Sarmatian-Chokrak gradient peak, the pressure here regresses from 0.44 psi/ft (average value) to considerably low values of 0.4347 psi/ft in the Upper Cretaceous deposits. This regression is fractured into two by Sarmatian gradient peak: 0.444 psi/ft (minimum values), 0.4539 psi/ft (average values) and 0.465 psi/ft (maximum values) (Table 6 and Fig 18).

In this case, the equivalent maximum gradient values expressed in mud units reach 8.98 ppg in Sarmat deposits, which is considerably higher than the gradients in overlaying and underlying deposits; this can complicate drilling, especially in cases if the minimum values dominate in overlaying and underlying horizons.

That is, this mineralization profile creates a correspondingly similar contrasting profile of hydrostatic pressures in this region, both in the gradient and equivalent values of the drilling mud.

CONCLUSION

As a conclusion, we can name the following main results obtained from the studies:

1) A method (algorithm) identifying full salinity of drilled collector horizons during the drilling process and based on logging data was developed and proposed.
2) A sequential calculation method for hydrostatic pressure gradients based on both total dissolved solids defined by the total amount of solid impurities dissolved in reservoir water, and its chloride component was proposed.
3) It was recommended to calibrate the full and chloride salinity values on the basis of laboratory results obtained by analytical methods.
4) Hydrostatic pressure gradients for deposit sections of four main zones of the South Caspian Basin were defined and calculated as calibration data on the basis of collected literature information on water salinity results.
5) Overall trend of changes in hydrostatic gradients were defined and described both for each individual zone of the South Caspian Basin and all four zones of the basin covering these regions.
6) Study results allows to resolve the following practical tasks:
   - assess the salinity of the basin reservoirs forming as a result of lithification of the set of its sedimentary rocks.
   - generate more effective model of the set of parameters of the basin evolution associated with its pore pressures.

- reduce the drilling risks by correct planning of the wells in the conditions of abnormally high pore pressure.

References

[1] Petroleum Geoscience. Jon Gluyas, Richard Swarbrick. John Wiley & Sons, 2013 M04-25, 376 pp.

[2] Alan R. Huffman, Glenn L. Bowers-Pressure Regimes in Sedimentary Basins and Their Prediction. AAPG Memoir-76. Houston. 1996.

[3] P. Skalle -Pressure Control during Oil Well Drilling. © 2011 Pal Skalle & Ventus Publishing ApS. 2011

[4] G. K. Hodlur, Ratnakar Dhakate, T. Sirisha & D. B. Panaskar. Resolution of freshwater and saline water aquifers by composite geophysical data analysis methods. Hydrological Sciences Journal – Journal des Sciences Hydrologiques, 55(3) 2010.

[5] Formation Evaluation - Log Interpretation Charts. 2015, Allied-Horizontal Wireline Services. All rights reserved. 132 pp.

[6] Archie, G.E. (1942) 'The electrical resistivity log as an aid in determining some reservoir characteristics', Trans. Am. Inst. Mech. Eng., Vol.146, pp.54~61.

[7] Jorgensen, D.G. (1990) 'Estimating water quality from geophysical logs' In STP 1989: Symposium on. Geophysical Methods for Geotechnical Investigations. ASTM Special Technical Publication, Denver, USA, pp.47-64.

[8] B. J. M. Goes et all. Estimating the depth of fresh and brackish groundwater in a predominantly saline region using geophysical and hydrological methods. Near Surface Geophysics, 2009, 401-412.

[9] Robert Maliva and Thomas Missimer. Arid Lands Water Evaluation and Management. Springer-Verlag Berlin Heidelberg. 2012.

[10] Arulanantan K. Salinity Measurements and Use of the Practical Salinity Scale (PSS). Oceanography Division, National Aquatic Resources Research and Development Agency, Crow Island., Colombo 15. 2002

[11] Mcconnell, C.L. (1983) 'Spontaneous potential corrections for groundwater salinity calculations–Carter County, Oklahoma, USA', Journal of Hydrology, Vol.65 No.4, pp. 363-372.

[12] Greg Ussher et All. Understanding the resistivity's observed in Geothermal Systems. Proceedings World Geothermal Congress 2000

[13] Hannes Schmidt et all, The density–salinity relation of standard seawater. Ocean Science, 14, 15–40, 2018

[14] Dong J. (2009) 'Rapid determination of total dissolved solids in drinking water by the conductivity meter', Chinese Journal of Health Laboratory Technology,Vol.19 No.10, pp.2719-2420.(

[15] F.M. Hajiyev. Hydrogeological conditions of formation and distribution of oil and gas fields in the South Caspian Megatrough. Moscow. Nedra, 1998. 386 pp.

Journal of Engineering Sciences & Modern Technologies
ISSN 3078-1760, E-ISSN 3078-1965
Volume 1, Number 1, 2025, page 24-29

BAKI ALİ NEFT MƏKTƏBİ
BAKU HIGHER OIL SCHOOL

https://jesmt.org/

https://doi.org/10.70334/3078-1965.2025.1.24

UDC 004.932

Using convolutional filter for restoration of distorted image

Naila Allahverdiyeva

Baku Higher Oil School, Department of Process Automation Engineering, Baku, Azerbaijan
naila.allakhverdiyeva@bhos.edu.az

Keywords:

Image Restoration, Convolutional Filter, Homomorphic Filtering, Blind Deconvolution, Image Processing

A B S T R A C T

The main objective of this paper is the enhancement of the quality and the restoration of the acquired and distorted images. There are a lot of application areas and many methods of image restoration. In this work we apply Convolutional Filter for such case. This technique includes several stages. First stage was pre-processing phase before coding in terms for method selection and picture size adjusting and writing pseudo code for copying it to the script. After pre-processing, the next stage is compiling the code and observing results obtained from different methods. Two different solutions for image enhancement have been used in this work. First method is Homomorphic Filtering which has been applied to the distorted image. Obtained result is very satisfactory in terms of the quality of the outcome picture. The second method is the Blind Deconvolution method. The Blind Deconvolution algorithm is also very good in terms of the error range and the quality of the resultant image. On the other hand, it has been observed from the results that, the Homomorphic Filtering can be good choice for object detection, while the Blind Deconvolution algorithm should be applied where the adjusting of the brightness of the input image is required.

Received: 06.03.2024
Accept: 10.04.2024

I. Introduction

There are several methods and solutions for image restoration and its enhancement from unwanted noises, in theory. It is the reason why there are several methods for coding, too. Therefore, some different methods can be realized by using software, moreover, their outcomes can be analyzed and compared with each other. Furthermore, it is obvious that, to demonstrate, to analyze and to compare the results of the methods is very important, and it can be done by visualization of the outcomes in the MATLAB software. There are several types of information which can be gathered from the result of the written script. For image restoration, there are two main types of the data which should be observed by the software result box.

First necessary type is the visual illustration of the images. There is not only the picture of the resultant procedure, but also, all images from different steps can be shown in the window after the code compiled, one by one. This property of software allows to follow the results and observe the changings from the previous stage to the next stages. If the result is not satisfactory, then the code can be alternated, and the results can be observed until the desired image is obtained. There is also a great opportunity which provides to observe different images or results in one picture. Moreover, the images from the different steps of the filtering process can be saved in the folder or anywhere in the memory of the computer. It creates a chance to creating a database and used past results in order to improve the future results or solutions by means of the prediction methods which are working based on the past conditions and comparison among them. Addition to this, the images can be edited after the result

was shown in the main window. There are some tools for increasing the size of outcomes or changing some properties of resultant image in terms of its type of the file for saving them in a proper way.

The second necessary type of data which is demonstrated by the outcome of the written script is the numerical or graphical parameters which can be useful for different phases of the image restoration processes. There is another opportunity here in order to follow and observe the results of the phases by means of the results of the mathematical calculations. If there are a lot of errors in the numerical values of the results in the phases compared with the theoretical calculations, it means that there should be miswriting of the formula for calculation of that phase or there should be the error which arises from the previous stage. In terms of those factors, the determining of the numerical values such as values of the matrix row and columns for images for the different stages of the image deblurring is very necessary. Addition to this, the results should be stored and copied to the text file or excel file, and it enables to check the process progression and analyze the errors and time-wasting parts in order to provide high quality output and decrease the downtime for the further applications of those filters. All parameters are important for further processing of the pictures and their availability creates very good environment for development of the next procedures.

Overall, there are a lot of benefits of using software in order to observing results from the theoretical background and the results from the software decreases the time for hard calculations and all results can be observed, individually. Furthermore, usage of the software for a lot of applications increases the speed of the progression of the theory part, because all faults are detected immediately, and there is only requirement to change the part at the theory in order to correct the faults in the code part. Addition to this, the outcomes of the different solutions and methods for the same problem can be easily compared by means of the software, and it allows to check a lot of conditions and to suggest the most optimal way for solving the same type of the problem in which there are a number of the methods for solving them, in theory.

The preprocessing for coding consists of problem defining and suggesting of the methods for applying them for the specific problem. Therefore, it is necessary to gather a lot of information about the input data which has to be processed by the filter which should be selected in the preprocessing phase. The preprocessing stage is more theoretical rather than practical, because the digital images are only used for observing the problem and suggesting the solutions about that issue. The experiences allow to detect the base of the problem and apply the most optimal solution for that type of the problem. However, there should be conditions in which the problem is unknown and there is not more information about those types of distorted images restoration or deblurring [1-4]. On the other hand, the information from the past problems should be non-beneficial in terms of providing suggestions for solutions of the new types of the problems related to the distorted image restoration. Although the sources of both theoretical part and practical part is not enough for solution, the digital analyzing should be done in order to observe the problem, deeply. The matrix of the pixels of distorted image can be extracted from the software and it can be very useful in order to new proposals for restoration of that specific image.

The preprocessing phase of the image restoration by the software is the one of the most important stages which directly affect the resultant patterns, in terms of the optimal way of solutions, the spending time on the problem and obtaining high quality picture as an outcome. Moreover, there are several simple parts before the coding in software and first stage is downloading image from the main source with its original version. On the other hand, if there is requirement for decreasing the sizes of the image dimensions it has to be done before writing script. The sizes of the image are also necessary in order to observe the full potential of the methods which are selected for solution of the problem which is the removing unwanted part from the main original or desired picture. The regulation of the dimensions of the input image can be done by the several sources such as websites and specific software. There is some software which adjusts the dimensions of the input image into the desire format.

After that, the ready functions inside of the software are necessary to be known and their usage improves the way of coding and it decreases the number of the rows in the script. Moreover, the ready functions are very useful in terms of their high-speed work, because the code which is background of those functions has the most optimal and high-speed algorithms. On the other hand, there should be the condition in which the ready function for that condition is not identified beforehand and ready. To solve those types of the problems, it is required to write the code for

the special function and it can be used as a ready function in the different parts of the script by its referred name in the function code part.

To sum up, if all phases of the preprocessing are done the next stage can be started by means of the information taking from the preprocessing stage of the writing code in the special software. Addition to this, it is clear from the above part that the preprocessing stage affects the next stages and also the resultant image, directly. Because this procedure determines the way of approaching the problem and suggests the solutions in terms of the past experiences. However, if there are not the experiences for new type of the problem, then the new approach is provided by the preprocessing phase, and it is done by observing the parameters of the distorted picture by means of the numerical values and the graphical representations of several important parameters. Addition to this, the selection of the appropriate dimensions of the distorted image for using it as an input for the software is another essential phase of the preprocessing stage. The next stage in the image restoration by means of the practical way is the defining the sequence of the code and writing pseudo code in order to observe the algorithm based on the theoretical knowledge to see whether there is a fault or not. If all parts have done correctly in the paper for the preprocessing, then the code can be written in the software, in order to observe the results from the applied method which is suggested by means of the preprocessing techniques. After the preprocessing part is finished, then the next phase of the distorted image restoration can be started in order to complete the full process until the satisfactory result is obtained.

II. Image Restoration

The coding process as the part of the image restoration sequence, is the most important section in terms of making decisions about several problems and solutions for those problems. It was used MATLAB software for image restoration and two different types of the filtering in order to enhance and restore distorted images by means of the different factors.

First method which has been used for image restoration is Homomorphic filtering which has a lot of advantages in terms of removing distorted parts from the unknown type of combination of the functions. In our case, the image should be distorted by the unwanted weather conditions and also blur of the point spread function (PSF) of the device for image taking. Addition to this, all phases in the Homomorphic filtering have been used for writing code and all mathematical parts are represented by the appropriate function in the MATLAB software.

Second method which has been used for the distorted image restoration or deblurring is the blind deconvolution algorithm which is very useful in terms of increasing the brightness of the picture and improving the quality of the picture. In our case, the picture is blurred artificially, by means of the white noise with its specific mean and variance. After that, blind deconvolution algorithm has been used for deblurring the picture for the further processing.

III. Homomorphic Filtering

There are five main phases in the Homomorphic filtering method and all of them have been introduced in our code.

Firstly, it is necessary to introduce the picture to the code by means of the 'imread' command which provides the reading of the image from the defined location such as predefined location file or folder of the image. Inside of the command, the address of the image, its correct file and its file type should be written. If the image is in the desktop, there is not requirement to write the address of the image, only the name and file type are enough for reading image by the software. After that, 'imshow' command is used for illustrating the original image which needs for restoration. Moreover, if it is necessary to compare the outcome picture with the original input image or images from previous stages, there is 'imshowpair' command which allows to join two pictures in one figure. There is another main command in the MATLAB which is the 'rgb2gray' command that converts colorful RGB image into the gray image which has two dimensions and the result has two-dimensional matrix values.

```
%% Image Restoration with Homomorphic Filtering
%Image reading from Desktop
myimage1= imread('im6.jpg');
%Conversion from Colorful Image into the Gray Image
grayimage1=rgb2gray(myimage1);
figure, imshow(grayimage1);
grayimage1 = im2double(grayimage1);
%Applying Logarithm for Linearization
grayimage1 = log(1 + grayimage1);
A = 2*size(grayimage1,1) + 1;
B = 2*size(grayimage1,2) + 1;
sigma = 2;
[C, D] = meshgrid(1:B,1:A);
centerC = ceil(B/2);
centerD = ceil(A/2);
%Determination of the Numerator
```

```
myNum = (C - centerC).^2 + (D - centerD).^2;
%Applying Anti-Logarithm
antilog = exp(-myNum./(2*sigma.^2));
antilog = 1 - antilog;
imshow(antilog,'InitialMagnification',25);
antilog = fftshift(antilog);
%Applying Discrete Fourier Transform
myDFT = fft2(grayimage1, A, B);
%Applying Inverse Fourier Transform
myResult = real(ifft2(antilog.*myDFT));
myResult =
myResult(1:size(grayimage1,1),1:size(grayimage1,2));
mymain = exp(myResult) - 1;
figure, imshowpair(myimage1, mymain, 'montage') ,
title('Original Input Image and Outcome Image from
Homomorphic Filtering');
```

After image reading, the next stage is conversion from the colorful image into the gray image by means of the 'rgb2gray' command. The next procedure is to convert gray image into the double format by means of the 'im2double' command which increases the precision of the values of the matric of the picture. Then, the logarithm function is applied as a part of the Homomorphic transform and it is realized by means of the 'log' command. The transfer function which should be used for removing the negative effects of the point spread function (PSF), is created by means of the two arrays. The commands for defining transfer function are 'size' and 'meshgrid' commands which are useful in order to provide true grid points for center. After the unwanted part has been removed, then the inverse Homomorphic transform has been applied in order to observe the results. For last processes, anti-logarithm and inverse Fourier transform have been applied by means of the 'antilog' and 'ifft2' commands. As a result, first original image and the resultant image are shown in Fig.1 by means of the 'imshowpair' command.

Fig. 1. Result from Homomorphic Filtering

Overall, the result from the Homomorphic filtering is very satisfactory in terms of the noise reduction on the distorted image by means of the unwanted weather conditions. As a result, the objects with dark colors had the more colorful in terms of deblurring. Moreover, it is very good outcome for further processing as an object detection. Because in the first original input image, the black objects are hardly identified, because they have been distorted by the undesired factors. However, Homomorphic filtering enables the ways in order to work with that problem, and as a result, the image is cleared from the noisy patterns (Fig.2).

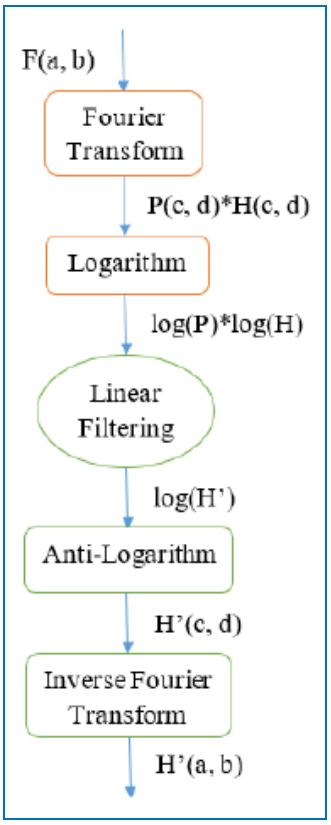

Fig. 2. The sequence of the stage in Homomorphic Filtering

In order to illustrate graphically the notion of similarity level *SL* between any given pair of data clouds we have cut *11* different data clouds (windows) from the entire data cloud in Fig. 2. For this purpose we have used equal length of each window of *M=500* samplings that corresponds to the respective data cloud. In addition, these windows are not overlapping to each other, but are rather arranged in a consecutive order and the extracted data clouds are numbered from *1* to *11*. The illustration of the all *11* data clouds is depicted in Fig. 3.

Homomorphic filtering also affects the tonal structure of the images. We have obtained results that, Homomorphic filtering increase the dark tonal pixels and it is very useful for object detection as further processing (Fig.3).

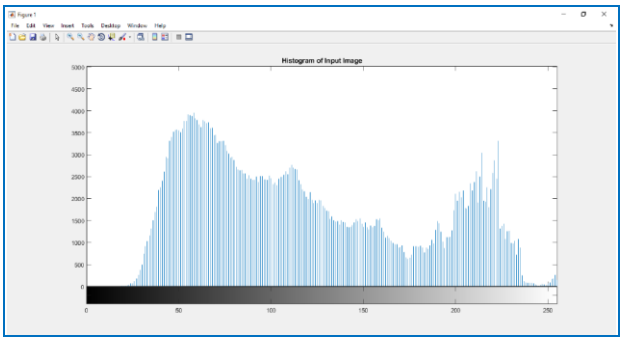

Fig. 3. Histogram of Input Image

It can be observed from the above figure that, the pixels have been distributed among each tone, and there are also light tones which belongs to more pixels (Fig.4).

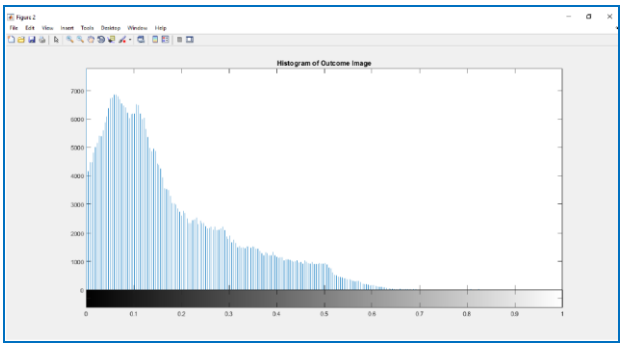

Fig. 4. Histogram of Outcome Image

After Homomorphic filtering, it can be seen from the image above that, the dark tones of the image have more pixels rather than the dark pixels of the input image. Therefore, Homomorphic filtering can be very useful for object detection in terms of their colors and their tones of pixels.

IV. Blind Deconvolution Algorithm

Based on the theoretical mathematical methods, the pseudo code has been written before copying it into the software script. For that problem, it has been used also the MATLAB software for coding and observing results. The blind deconvolution algorithm has a very satisfactory results in terms of distorted image restoration from the unwanted factors over the original desired picture.

To begin with coding, there are several types of the convolutional filters which are able to deblur the distorted image. Firstly, it is necessary to read the image from its address by its file name by means if the 'imread' command. Addition to this, this original picture can be shown by means of the 'imshow' command. Then, the colorful input image is converted into the gray picture with usage of the 'rgb2gray' command. Moreover, the special point spread function is created by means of the 'fspecial' command, and then, it is convolved with the original input image with 'imfilter' command in order to provide artificial blur over the original image. There have been several point spread functions which are constructed by means of the 'deconvblind' command. In picture it has been shown pictures of the all of the point spread functions which are obtained by different ways. 'padarray' command is used for creating an array which has non-negative integer values and there should be some zeros inside of this array and therefore, its loading with values is very important. The zero values should be located in the place where there is the unwanted part of the input original array.

By using comparisons between methods, it can be clear that, what type of the filter can be suggested in the what type of function combination or image restoration.

```
% Reading Original Image from Desktop
myimage = imread('C:\Users\adilr\Desktop\PTZ3.png');
%Conversion from Colorful Image into the Gray Image
myimage = rgb2gray(myimage);
figure, imshow(myimage),title('Input Image');
%Defining artificial blur Function
psfunc = fspecial('gaussian',7,10);
%Blurred Image by means of Convolution
myblurredim = imfilter(myimage,
psfunc,'symmetric','conv');
figure, imshow(myblurredim), title('Blurred Picture');
%Undersized PSF for Deblurring
sizeunder = ones(size(psfunc)-4);
[A1,B1] = deconvblind(myblurredim,sizeunder);
imshow(A1)
title('Result with undersized Function')
%Undersized PSF for Deblurring
sizeover = padarray(sizeunder,[4 4],'replicate','both');
[A2,B2] = deconvblind(myblurredim,sizeover);
imshow(A2)
title('Result with oversized Function')
%PSF
firstpsf = padarray(sizeunder,[2 2],'replicate','both');
[A3,B3] = deconvblind(myblurredim,firstpsf);
imshow(A3)
title('Result with firstPSF')
figure, imshow(psfunc,[],'InitialMagnification','fit'),
title('True PSF');
figure, imshow(B1,[],'InitialMagnification','fit'),
title('Reconstructed Undersized PSF');
figure,
imshow(B2,[],'InitialMagnification','fit'),title('Reconstruct
ed Oversized PSF');
figure, imshow(B3,[],'InitialMagnification','fit'),
title('Reconstructed true PSF');
Factor = edge(myblurredim,'sobel',.08);
MYse = strel('disk',2);
Factor = 1-double(imdilate(Factor,MYse));
Factor([1:3 end-(0:2)],:) = 0;
Factor(:,[1:3 end-(0:2)]) = 0;
```

```
figure, imshow(Factor), title('Weight Array');
[A,B] = deconvblind(myblurredim,firstpsf,30,[],Factor);
figure, imshow(A), title('Deblurred Picture');
B1 = 2;
B2 = 2;
mypsf = @( psfunc) padarray(PSF(B1+1:end-
B1,B2+1:end-B2),[B1 B2]);
[AF,BF] =
deconvblind(myblurredim,sizeover,30,[],Factor,mypsf);
figure, imshow(AF), title('Deblurred Picture')
figure, imshow(myblurredim), title('Blurred Picture')
figure, imshowpair(myblurredim, AF, 'montage'), title
('Blurred Image (Input image) Image after restoration
(Output Image)');
```

From the code, all steps are depicted clearly, and they are based on the theory about the blind deconvolutional filtering. There are several functions which have been used already in the script, and these functions are very beneficial in terms of the time consuming and high speed in terms of the working with the most optimal algorithms. To conclude the code part, all faults have been detected by means of the software and all have been corrected for obtaining the relevant outcome for the original input picture. Results are shown in Fig.5, Fig.6 and Fig.7.

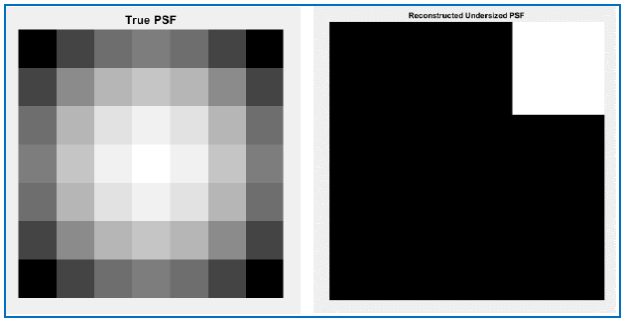

Fig. 5. True and Undersized PSF

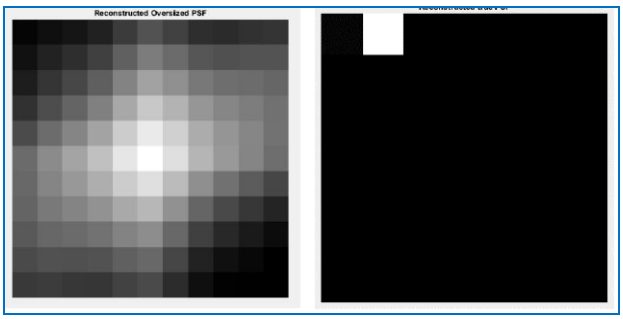

Fig. 6. Reconstructed Oversized and True PSF

Fig. 7. Output of Deconvolutional Filter

We have calculated mean square error between clear image and image after restoration. It is shown from the result that the mean square error is decreased by means of the Blind Deconvolutional Filter. Mean square error between clear image and image after restoration is equal to approximately 488, while it is approximately 85 between output image and first clear image.

It shows that Blind Deconvolutional Filter achieve 10 times better result and it improves image very well. This property of Blind Deconvolutional Filter allows to use this method in order to obtain good quality image from the distorted one.

V. Conclusion

Two different solutions for image enhancement have been used in this work. First method is Homomorphic Filtering which has been applied to the distorted image. Obtained results are very satisfactory in terms of the quality of the outcome picture. The second method is the Blind Deconvolution method. The Blind Deconvolution algorithm is also very good in terms of the error range and the quality of the resultant image. On the other hand, it has been observed from the results that, the Homomorphic Filtering can be good choice for object detection, while the Blind Deconvolution algorithm should be applied where the adjusting of the brightness of the input image is required.

References

[1] J.Biemond, J.W.Woods, A.M.Tekalp. “Boundary value problem in image restoration”, Proceedings of the IEEE International Conference on Acoustics, Speech, and Signal Processing, 1985.

[2] S.Smith. Digital Signal Processing: A Practical Guide for Engineers and Scientists. Publishing by Newness, 2015, 650 pp.

[3] W.C.Tang, M.K.Ng, R.H.Chan. “A fast algorithm for deblurring models with Neumann boundary conditions”, SIAM Journal of Scientific Computing, 1999.

[4] J.Biemond, D.E.Boekee, R.L.Lagendijk. “Identification and restoration of noisy blurred images using the expectation-maximization algorithm”, IEEE Transactions on Acoustic, Speech, and Signal Processing, 1990.

Journal of Engineering Sciences & Modern Technologies
ISSN 3078-1760, E-ISSN 3078-1965
Volume 1, Number 1, 2025, page 30-39

BAKI ALİ NEFT MƏKTƏBİ
BAKU HIGHER OIL SCHOOL

https://jesmt.org/

https://doi.org/10.70334/3078-1965.2025.1.30

UDC 004.65

Monitoring system for anomaly detection in plants with continuous operation

Gancho Vachkov

Baku Higher Oil School, Department of Process Automation Engineering, Baku, Azerbaijan
gancho.vachkov@bhos.edu.az

Keywords:

Data streams,
Data cloud models,
Moving window,
Grid cells,
Anomaly detection,
Similarity analysis

A B S T R A C T

Detection of anomaly in the operation of continuous plants and systems based on real time observations is a very important activity that aims at determining the health status of the system. This paper presents a methodology and algorithm for creating a computer monitoring system for anomaly detection in online mode. The proposed method includes creating Data Cloud models based on predefined equal size portions of data samplings and estimating the Similarity Level between them as a bounded value in the interval [0, 1]. Data cloud models use the concept of mesh of grid cells that capture the local density of the data points around the cells. The Similarity analysis is based on estimating the difference between the local densities in the two data clouds. The whole methodology is explained and illustrated in details in the paper by using numerous examples with real data. The proposed monitoring system is based on using the moving window concept for continuous analysis of the similarity level in online mode. The final section of the paper shows experimental results for anomaly detection based on using real operation data (temperatures) from a Petrochemical plant.

Received: 30.09.2020
Accept: 15.03.2024

I. Introduction

Chemical plants are typical examples of continuous operating plants with hundreds or thousands of technological parameters, such as temperatures, pressures, levels, flowrates etc. being measured constantly with a given sampling period. All these measurements are first recorded and then analyzed in *near online* or in *offline* mode for decision making about the quality and the status (normal, abnormal) of the plant operation. In practice the measurements produce endless *data streams* because at each sampling period a new data point for the respective process parameter is added. The data streams are usually *multidimensional* (multichannel) in structure, where every measured parameter represents a single channel in the data stream.

Analysis of the multidimensional data streams in real time is an important activity that is aimed at extracting a meaningful information about the *health status* of the operating plant or system. However, this analysis represents a big challenge in terms of computation complexity, time consuming, accuracy and plausibility. One of the problems that arises in analyzing the data streams is that we are not able to use the whole (unlimited) length of the stream because it is continuously increasing with each new sampling time. Therefore the most often used approach for data streams analysis is the *moving window* approach. Here we use consecutively relatively small portions of the data stream, called *windows*, with a predefined fixed length for making *local analysis* based on this concrete portion of data. Then we proceed to the next window with the same size that takes another fixed portion of data from the data stream, but moved ahead by one or more steps (samplings).

Here obviously the size (length) of the window, as well as the step for proceeding to the next window are important tuning parameters that obviously influence the accuracy and the generalization ability of the analysis.

There could be different ways of analyzing (data mining) of the data streams based on the moving window concept. This analysis depends on the specific aim, goal and area of application. One of the first things that is needed to be analyzed from a given data stream is to judge the current health status of the continuously operating system in terms of detecting some anomaly in its operation.

The definition of anomaly is quiet vague and subjective one, but usually the operators of the system (plant) are the best people to be able to detect it. They use their long term experience on operating and monitoring the plant, in order to discover whether or not the current operation (i.e. the current observed multichannel data stream portion) can be classified is *normal* or *abnormal.* Foe such judgment they use their knowledge about the prescribed limits of the technological parameters combined with some other human based factors about the history in the operation of this plant.

An excellent survey of the general methods for anomaly detection based on data and data streams can be found in [1]. Here the authors split the methods in several categories, such as: Classification based, Distance based, Clustering based, Statistical and Information theory based etc. Other concrete methods and application in the area of anomaly detections in data streams are presented in [2,3]. Another similar problem, namely change detection in radar images has been investigated and applied in image processing [4], but it is also interesting and can be applied to data streams in industrial systems.

The research in this paper is a continuation of our previous research work [5,6,7] in the area of anomaly detection and change detection in data streams. In this current work we are introducing some new algorithms for similarity analysis and for anomaly detection. The algorithms have been applied to real data from the continuous operation of a petrochemical plant.

The paper is organized as follows. Section II explains the notion of the Similarity Analysis. Sections III and IV presents the theoretical part about creating the Data Cloud Models and estimation of the Similarity Level. Sections V and VI are practical and explain the structure of the proposed Monitoring System as well as the experimental results. The conclusions and suggestions for a future research and improvements are given in Section VII.

II. The Concept of the Similarity Analysis of Data Clouds

As mentioned in the previous section, estimation of the similarity level between given pairs of windows from the data stream plays fundamental role in the data stream analysis and consequent decision making about the health status of the plant operation. This include also detection of a possible anomaly in the plant operation.

In this paper we define the similarity level *SL* as a real valued number between *0.0* and *1.0* that shows in a numerical way *how close* are two available portions (windows) of data taken from the data stream. Such portions of data are further on called *data clouds*. For example, the extreme case of *SL=1.0* represent the *maximal* similarity of the two data clouds, when they are *identical*. while the other extreme case of *SL=0.0* represents completely *different* (not similar at all) data clouds. All other possible intermediate values of *SL* between *0.0* and *1.0* correspond to different levels of similarity between the given data clouds.

In the simplest case, the data stream could be just *one-dimensional*, when it contains a *single* time series of measurements of one process variable (e.g. temperature). However, the real cases are usually dealing with *multidinesional* (multi-channel) data streams that represent the behavior of $K > 1$ process variables by respective time series. An example of a three-dimensional ($K = 3$) data stream is shown in Fig. 1.

The plots in Fig. 1. are actually three *time series* that represents the *temporal behavior* of three process temperatures *T1*, *T2* and *T2*, collected as real data with a sampling period of 6 minutes and taken over an interval of *5600* samplings. This is equlvalent of *560* hours operation of a plant operation (roughly about *23* calendar days) and represents the continuous operation of the *Stabilization Section* of the gasoline production in a Petrochemical plant, as explained and our previous research in [5]. For easy understanding by graphical illustration of the main concept for similarity analysis and detection of anomaly, we will consider further on in this paper only the two dimensional case ($K=2$) with the temperatures *T1* and *T2*.

Throughout the paper we use *M* to denote the *length* (number of the preselected data points) of the data stream. All these data points constitute one specific *data cloud in the K*-dimensional space. Further on we use the notations of *x* and *y* to denote the respective process parameters (e.g. temperatures *T1* and *T2*) of the two-dimensional data streams.

The next Fig. 2. shows the main (entire) data stream with *5600* samplings displayed as a two dimensional *Data Cloud* in the *T1-T2* space. Each sampling in it is represented as one *data point* in the space.

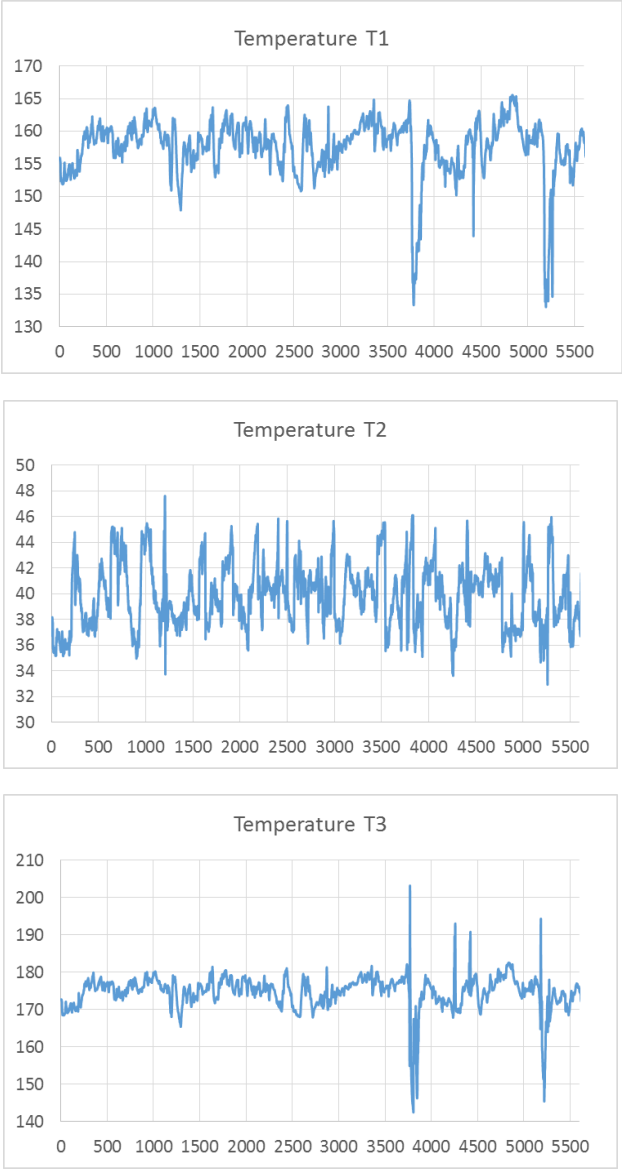

Fig. 1. A three-dimensional data stream that represents three process variables (temperatures): T1, T2 and T3 for 5600 samplings.

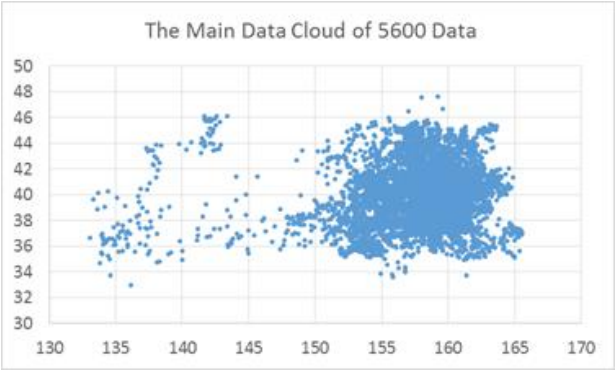

Fig. 2. The main Data Cloud that represents the whole length with M = 5600 samplings of the Data Stream

In order to illustrate graphically the notion of similarity level *SL* between any given pair of data clouds we have cut *11* different data clouds (windows) from the entire data cloud in Fig. 2. For this purpose we have used equal length of each window of *M=500* samplings that corresponds to the respective data cloud. In addition, these windows are not overlapping to each other, but are rather arranged in a consecutive order and the extracted data clouds are numbered from *1* to *11*. The illustration of the all *11* data clouds is depicted in Fig. 3.

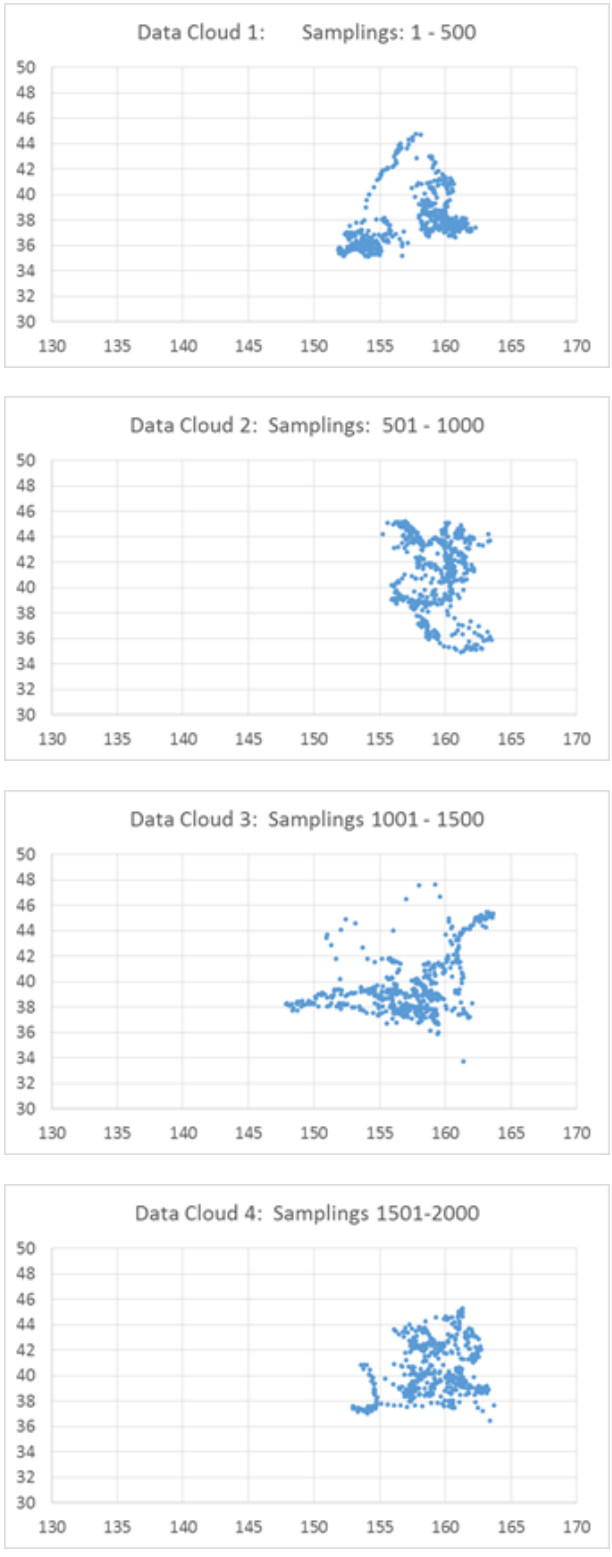

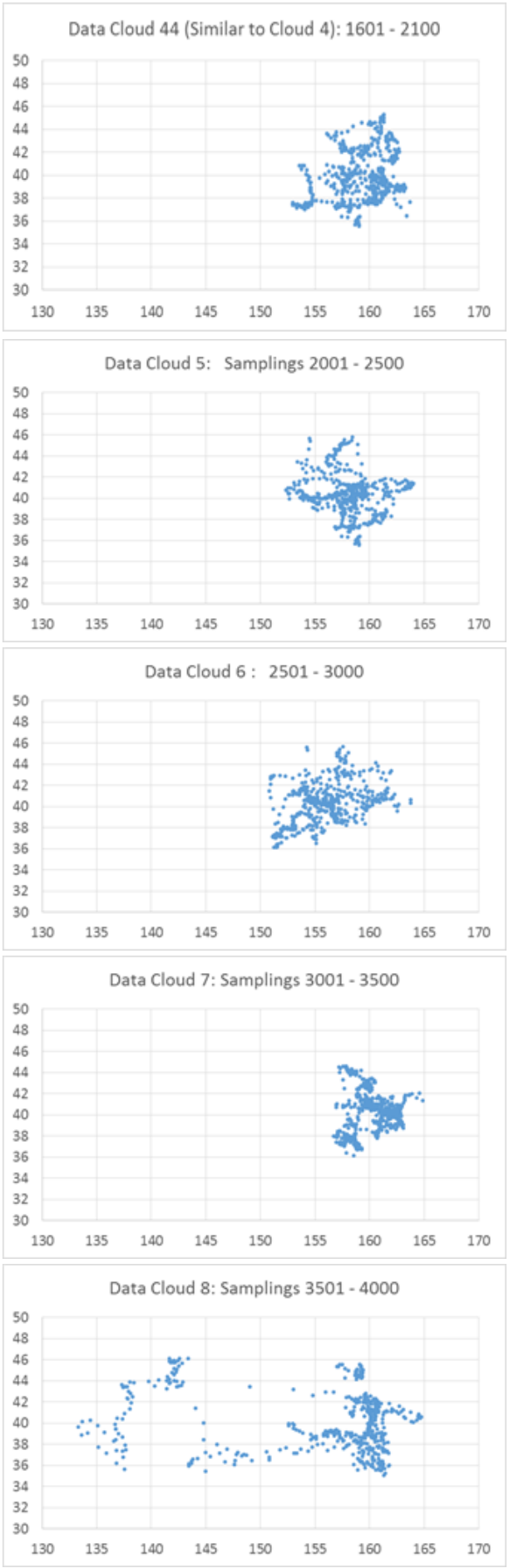

Fig 3. Illustration of *11* Consecutive *Local Data Clouds* with equal length *M = 500*. The cloud named as *Data Cloud 44* is highly overlapped with the *Data Cloud 4* and the high visual *similarity* between them can be easily noticed.

It is easy for the human operator to recognize visually the difference between the data clouds, because each of them have its specific shape in the T1-T2 space. However, we have to create a method and algorithm that will estimate the similarity level as a numerical value *SL* between *0.0* and *1.0.*

In Fig. 3. one additional cloud is shown that is labeled as *Data Cloud 44.* It has been specially created to demonstrate a high similarity level of *SL*, compared to the *Data Cloud 4*. Actually the two data clouds have a high overlapping ratio of *75%* between them with only *100* data (i.e. 25%) that are different. Therefore it is easy to notice *visually* that they are very similar in shape. However the concrete similarity level *SL* can be determined by the established method, described in the sequel of the paper.

III. The Data Cloud Model Based on Grid Cells

The data clouds extracted from a data stream can have arbitrary shape in the *K*-dimensional space as seen from Fig. 3. Therefore in order to compare two data clouds numerically and calculate the respective similarity level SL we have to create a Data Cloud Model (*DCM*) for each of the data clouds. The *DCM* will have some parameters that estimate the characteristics of the data cloud in the space, such as *structure* of the data within the cloud, *density* of the data in different locations, *size* or volume of the cloud in the *K*-dimensional space etc. Once these parameters are extracted then the comparison of any pair of data clouds becomes easy and straightforward.

For easy understanding of the concept for creating the *DCM*, in the next Fig. 4 and Fig. 5. we present one arbitrary chosen data cloud from the entire data stream in Fig. 1. This data cloud is labeled as *Example Data Cloud 1* and consists of *200* samplings within the interval (window) from *501* to *700* samplings.

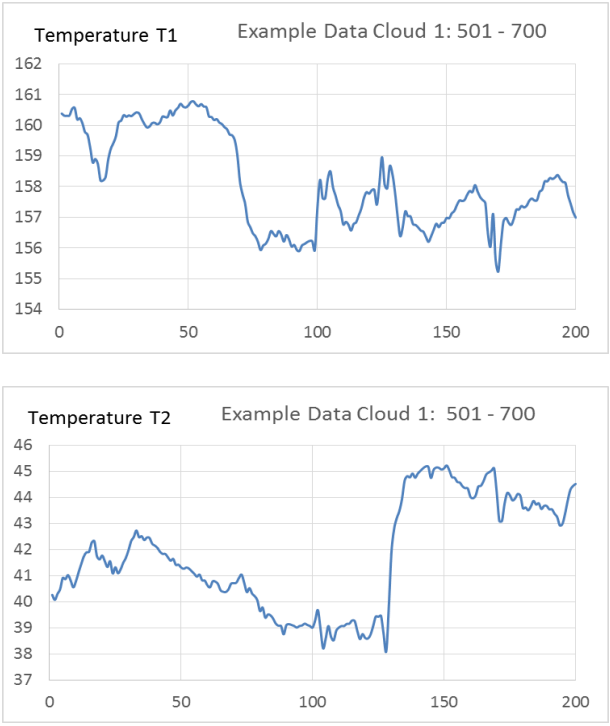

Fig 4. Time series of *200* data samplings for the temperatures *T1* and *T2* that are used to create the *Example Data Cloud 1*.

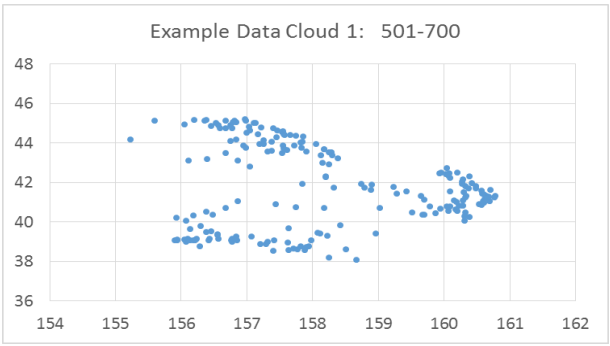

Fig 5. The *Example Data Cloud 1* consisting of *200* data points, taken from the time series in Fig. 1. within the range of *501-700* samplings.

In order to estimate the structure (volume) and density of this data cloud, we propose to create a *Mesh* of predefined number of *Grid Cells* in the *K*-dimensional space. The size and the boundaries of this mesh should be such that the data cloud is entirely inside the area of the mesh. As for the number *N* of all grid cells, it is subjectively defined by the assumed number of cells for each dimension. An example for a mesh of *N=9x3=63* grid cells that accommodates the *Example Data Cloud 1* is given in Fig. 6. It is obvious that the number *N* of the grid cells acts as a *resolution* of the Data Cloud Model in a sense that a larger *N* will produce a *DCM* with more precise characteristics about the modelled data cloud.

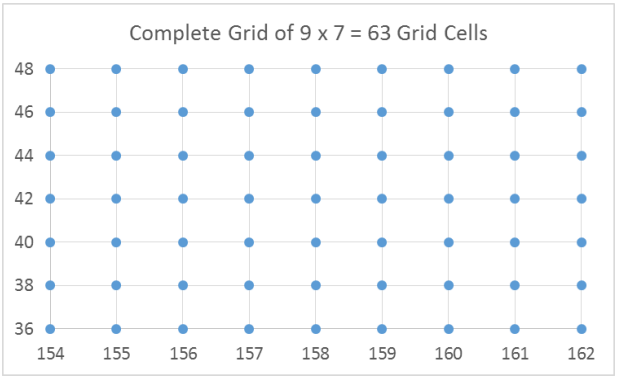

Fig. 6. The predefined *Mesh* of *N=9x7=63 Grid Cells* used for creating the *Data Cloud Model*.

Each grid cell from the mesh collects information about those data points from the *DCM* that are in the vicinity of this grid cell. Basically they collect information about the *number* of the data points and their *closeness* (*weight*) to this grid cell.

In order to obtain such information, we propose that each cell has its own *Gaussian* type *membership function* with *predefined width* for each dimension. The width should be calculated in such way so that the membership functions of every two neighboring grid cells overlap at a level of *0.5*.

Graphical illustration of the one-dimensional case (*K=1*) with *5* evenly distributed grid cells is given in Fig. 7.

Here *C1, C2, ..., C5* are the *centers* (locations) of the grid cells in the one dimensional input *x*. If *d* denotes the *distance* between the center *C* of a given grid cell and its neighbouring cells (from *left* and from *right*), then all data points from the data cloud that fall within the interval [*C-d, C+d*] are called *active data* in respect to this grid cell. They are denoted by M_{ad}. It is obvious that the summation of all active data M_{ad} for all grid cells will make the number *M* of all data in the data cloud.

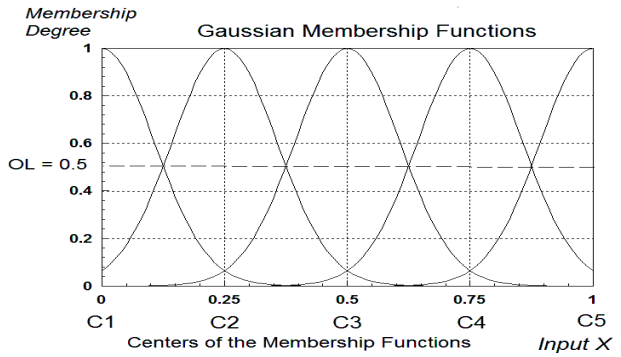

Fig. 7. Example of *5* symmetrical Gaussian Membership functions with overlapping level *OL = 0.5* for one input.

It should be noted that depending on the concrete structure and density of all *M* data points from the data cloud in the space, there could be a case when there are *no* active data points for a certain cell, i.e. $M_{ad} = 0$. In such case we classify this grid cell as *inactive*. Obviously we are only interested in the *active grid cells* with $M_{ad} > 0$ and their number is denoted as N_{act}.

We can estimate additional (more precise) parameter that represents the *closeness* (*weight*) of each data point to a given grid cell, as a value between *0.0* and *1.0*. It is given by the formula for the *Gaussian* membership function:

$$f_x = \exp\left(-(x-C)^2 / 2\sigma^2\right) \in [0,1] \qquad (1)$$

Here *C* and σ are the *center* and the *width* (spread) of the *Gaussian* membership function for this grid cell and f_x represents the *membership degree* (equivalent to the *weight*) of the data point associated to the grid cell.

Then a new parameter called *density* D_i of a given *active* grid cell can be calculated as summation of the membership degrees w_j (called also *weights*) from (1) of all the *active* data points to this grid cell, namely:

$$D_i = \sum_{j=1}^{M_{ad\,i}} w_j, i = 1,2,\ldots,N_{act} \qquad (2)$$

Here $M_{ad\,i}$, $i=1,2,\ldots,N_{act}$ denotes all *active data* points that are associated to the *i*-th active grid cell. These are all data that have membership degrees greater or equal to *0.5* for *all dimensions* for the given active grid cell.

It is obvious that the *density* of an active grid cell is a real number, which is *less or equal* to the number of active data points for this grid cell, i.e.

$$D_i \le M_{ad\,i},\ i = 1,2,\ldots,N_{act} \qquad (3)$$

The following three figures give a graphical illustration of the active grid cells and their densities for the *Example Data Cloud 1.* Fig. 8 represents the locations of all 21 active grid cells for this data cloud. It is seen that they are placed within the area of all *200* data points of the cloud.

Fig. 9 shows the number of all data points, associated to the active grid cells and Fig. 10 depicts the individual densities (2) for each active grid cell.

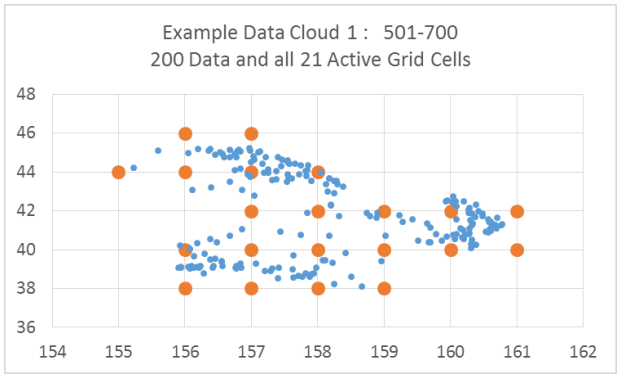

Fig. 8. Locations of all *21 active* grid cells for the *Example Data Cloud 1*.

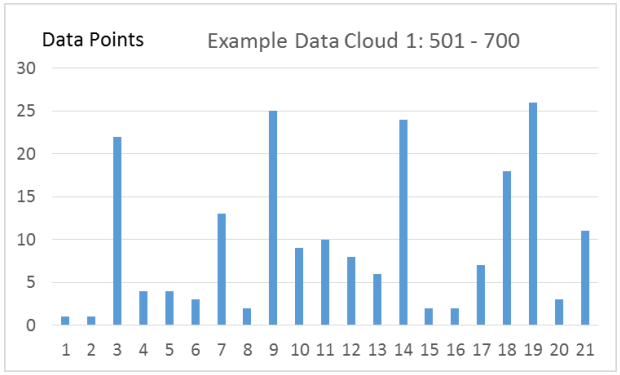

Fig. 9. Number of all data points, associated to all *21* active grid cells.

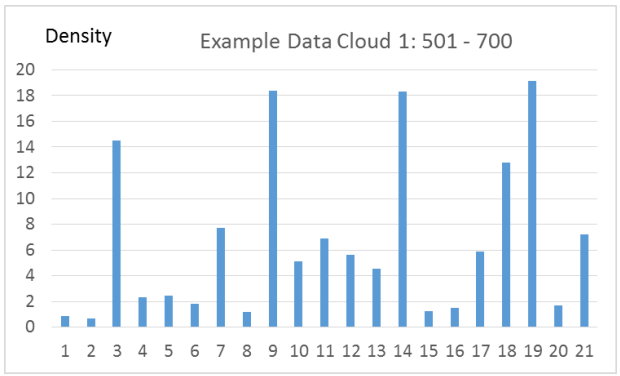

Fig. 10. Densities *Di* for all *21* active grid point for *Example Data Cloud 1*.

IV. Estimation of the Similarity Level Between Two Data Clouds

The data cloud model created in the previous section has two important parameters, namely: the number of the *active* grid cells N_{act} with their locations in the space and the respective *densities* (2) of the active grid points. These parameters can be used now for estimation of the similarity

level *SL* between any pairs of data clouds by the proposed algorithm in this section.

First of all we have to create one more *DCM* from a second data cloud. For the illustration purpose, we use the so called *Example Data Cloud 2* as shown in the next Fig. 11. and Fig. 12 in a similar way, as Fig. 4. and Fig. 5. The new data cloud has also *M=200* data points, but they are taken from another sampling interval, between *401* and *600*.

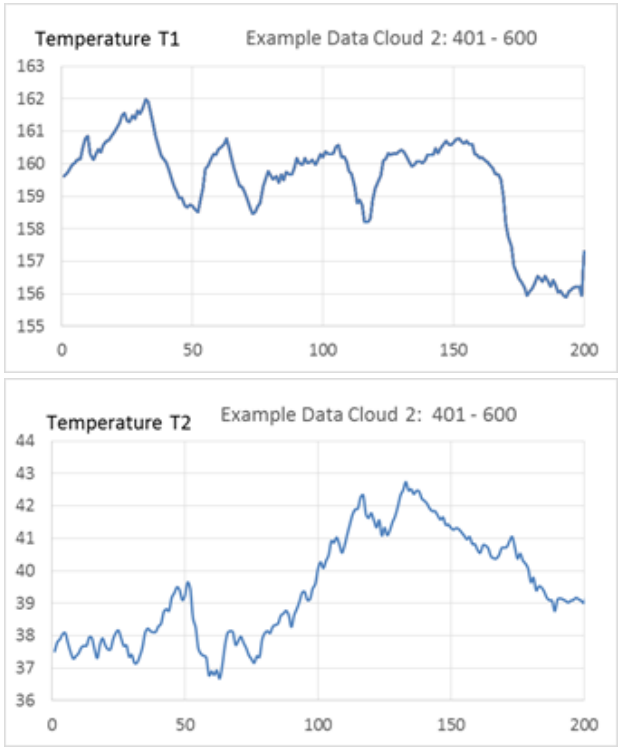

Fig 11. Time series of *200* data samplings for the temperatures *T1* and *T2* used to create the *Example Data Cloud 2*.

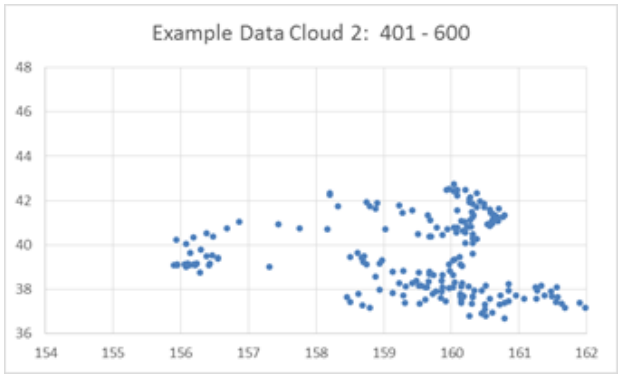

Fig 12. The *Example Data Cloud 2* with *200* data points, taken from the time series in Fig. 1. within the range of *401 – 600* samplings.

We used the method from the previous section to create the *DCM* for the *Example Data Cloud 2*. The created model has *19 active* grid cells and they are located partly in different locations, compared to the *21 active* grid cells from the model for the *Example Data Cloud 1*. The results for this *DCM* are graphically shown in the next figures: Fig. 13, Fig. 14 and Fig. 15.

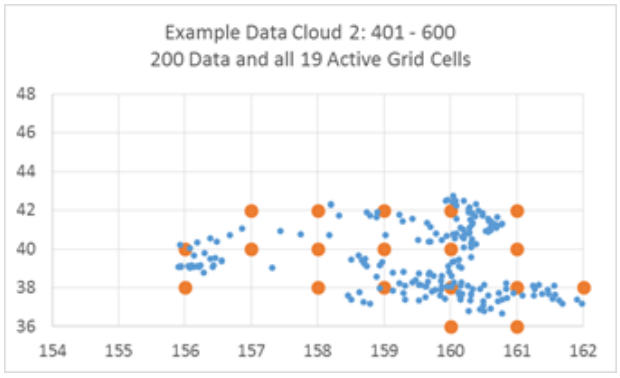

Fig. 13. Locations of all *19 active* grid cells for the *Example Data Cloud 2*.

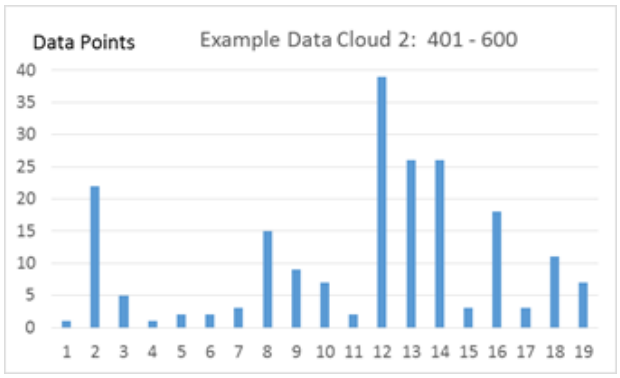

Fig. 14. Number of all data points, associated to all *19* active grid cells.

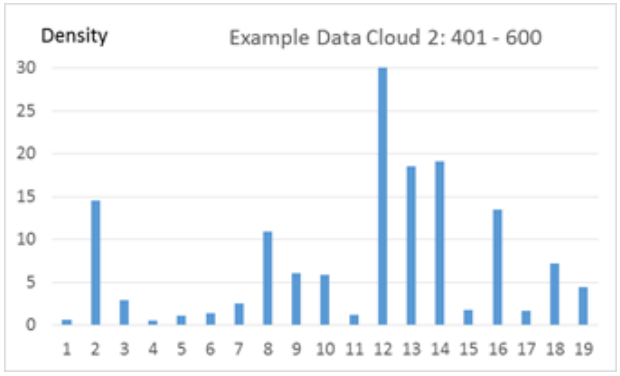

Fig. 15. Densities *Di* for all *19* active grid point for *Example Data Cloud 2*.

Now the comparison of the parameters of the two data cloud models will reveal the similarity level *SL*. The next Fig. 16 depicts the locations in the space of all active grid cells for both models. Then Fig. 17 illustrates all *14 overlapping* active grid cells that represent the *common area* of the space for the two data clouds. From a mathematical point of view this is the *intersection* of the two sets of the active grid cells for both models.

It is straightforward to conclude that a *partial* overlapping between the two sets of grid cells

will definitely lead to a similarity level *SL < 1.0* and the case of no overlapping between the sets will lead to *SL = 0.0*.

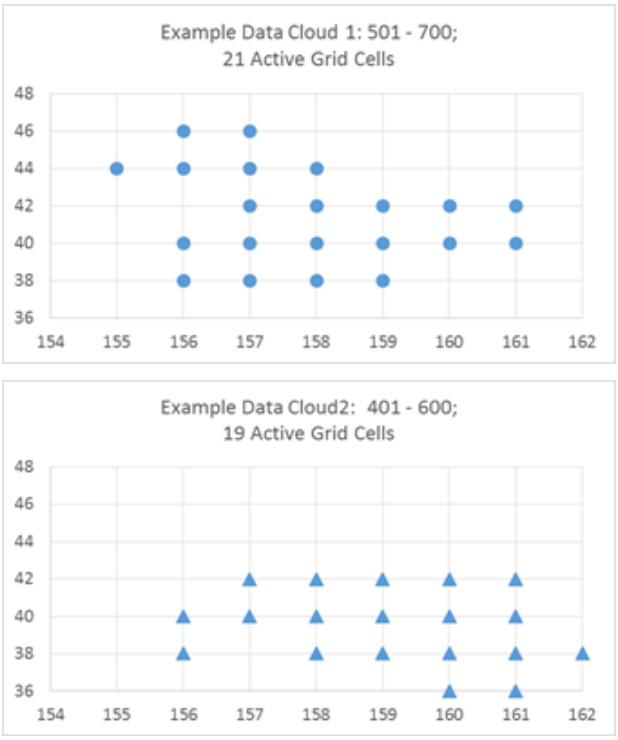

Fig. 16. Comparison of the locations of the *active* grid cells in the *T1-T2* space for *Example Cloud 1* and *Example Cloud 2.*

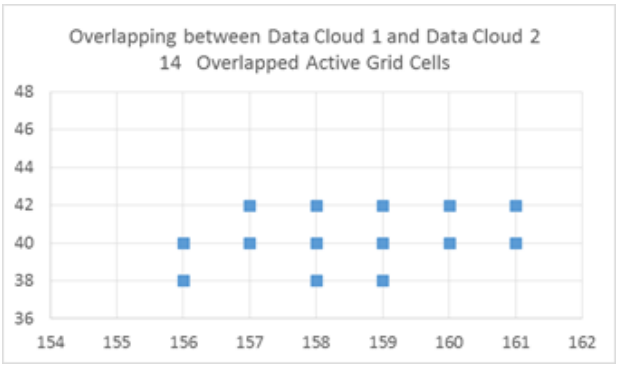

Fig. 17. The subset of all *14 overlapping active grid* cells between the *Example data cloud 1* and *Example Data Cloud 2*.

In the particular case, when the two sets have an *equal* number of active grid cells and their intersection also includes *all* the grid cells (i.e. they *coincide*), we still cannot conclude that there will be a *SL=1.0.* In this case we have to additionally check the *difference* between the *density* of all grid cells for both sets. Only in case this difference is *zero*, we conclude that *SL = 1.0,* i.e. the data clouds are *identical*.

The following general formula for calculating the similarity level *SL* is proposed below:

$$SL = 1.0 - \left(\sum_{i=1}^{N_{act}} \left| D_{iDCM} - D_{iWCM} \right| \right) \Big/ (2L) \qquad (4)$$

Here the subscripts *DCM* and *WCM* follow the notations of our work in [7]. In this current work they refer to the two data cloud models for *Example Data Cloud 1* and *Example Data Cloud2* respectively. Also, *L* denotes the size (length) of the data clouds, i.e. the number of the data points in the cloud.

The notation *Nact* in (4) means the number of the active grid cells in the *union* of the two sets for the two models. Therefore, this number is normally bigger than *Nact* for the active grid cells in each separate set. In such way the formula (4) for calculating the *SL* becomes general and includes the cases of partial overlapping between the two sets of grid cells. In this case of partial overlapping, the weight *Di* of the "missing" grid cell is considered as *zero*.

The denominator in (4) is *2L* in order to normalize the similarity level *SL* within the boundaries: [*0.0, 1.0*]. Then, when there is *no overlapping* at all between the two sets of grid cells. i.e. when *Nact*=0 in (4), *SL* will still bounded to *1.0* at most.

As a result of the proposed method for similarity analysis, the calculated similarity level between the two selected data clouds in Fig. 5 and Fig. 12 is: *SL = 0.6559*.

V. Structure of the Monitoring System for Anomaly Detection

As we commented in the Introduction, the moving window is a very suitable and practical approach to be applied for continuous (online) analysis of the similarity between pairs of data clouds (windows) taken from the endless data stream. Therefore we accepted such structure and approach in our monitoring system.

The monitoring system needs to read the data cloud model of at least one *abnormal case* in the operation of the plant. In the ideal scenario this is an anomaly that has happened before and has been analyzed and recorded as a data cloud. Then a respective data cloud model (*DCM*) was created and saved in a data base. There could be situations of several anomalies that have happened before and their respective *DCM* will also be added to the data base. In such way we can accumulate a data base, consisting of several *DCM* that represent several anomalies in the plant operation.

The objective of the monitoring system is to read at every sampling period one data window (one data cloud) from the data stream with the same length *M* as in the recorded *DCM* in the data base. As a second step the system will create the *DCM* for the newly read cloud from the data stream. The third step is to perform the similarity

analysis according to the explanations in Sections III and IV. Finally, the calculated similarity level *SL* will be displayed to the operator of the plant and can also be saved as a history of the operation.

This history will show at which periods of time the operation of the plants was moving closer to the prerecorded anomaly in the data base. In some possible extreme cases, a similarity level *SL* very close to *1.0* will show as warning that the current situation as almost identical to the previous anomaly. Then respective measures should be taken by the operator to "move" the plant operation away from this dangerous zone of operation.

Based on the above concept, we conclude that the monitoring system is a *passive* type of system that reads the information in online from the real operation of the plant, but the feedback action is left to the operator. Another characteristic of the system is that it is based on *Supervised Learning.* It means that the monitoring system needs a preliminary created and recorded model for one or more typical anomalies in order to calculate the similarity level between the current operation and all of the prerecorded anomalies.

The algorithm of the monitoring system for anomaly detection has been programmed in the DEV C++ environment and tested extensively on large number of examples. We consider that the created program is in fact ready for real practical applications.

VI. Experimental Results for Anomaly Detection

Here we show some examples for detection of anomalies by the proposed monitoring system. We have used the real operation data from the data stream in Fig. 1. However, we did not have any information about past anomalies in the plant operation. Since the proposed monitoring system is based on the *supervised* learning method, it means that the system cannot operate without such existing example.

Therefore we selected (almost arbitrary) several portions of *500* data from the data stream in Fig. 1. and labeled them as *anomalies.* Then for each such "anomaly" we created a respective data cloud model, which further plays the role of *reference model* for that anomaly.

When the monitoring system starts its operation in online mode, at each sampling time it selects one new window (one new data cloud) with the same length as in the reference model. Then a respective model, called *current model* is created from this window and used for calculating the similarity level *SL*. In offline mode the system stops at the end of the data from the data stream. Otherwise, the monitoring system is able to work continuously in online mode.

For demonstrating the performance of the monitoring system, we have selected *5* examples of "anomalies" in the operation of the plant, by selecting *5* data clouds from Fig. 3. in Section II and used them to create *5* respective *reference models* that were saved in the data base. These five reference data models were produced from the following data clouds: *Data Cloud 2, 4, 7, 8* and *9* in Fig. 3.

The plots in Fig. 18. show the performance results from the monitoring system in the form of *5* time series of the similarity level *SL* until the end of the main data stream *T1-T2* from Fig. 1. i.e. until *5600* samplings.

The correctness of the results from the monitoring system is easy to notice, because in all 5 time series for the similarity level *SL,* it reaches the maximal value *1.0* (*identical* data clouds) exactly at the sampling time when the respective reference model (the anomaly) is collected.

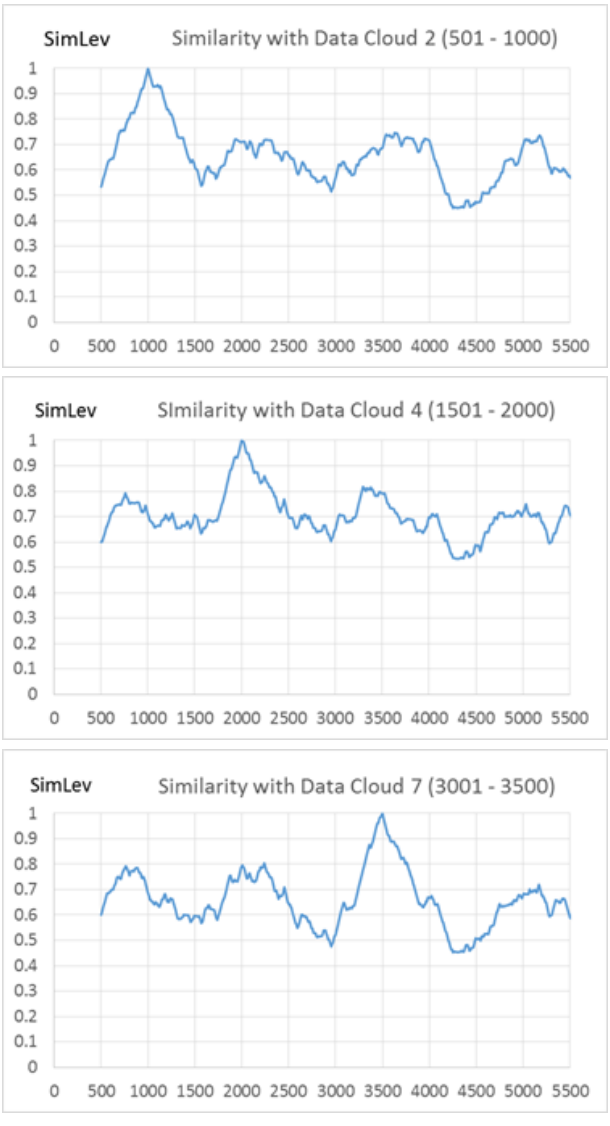

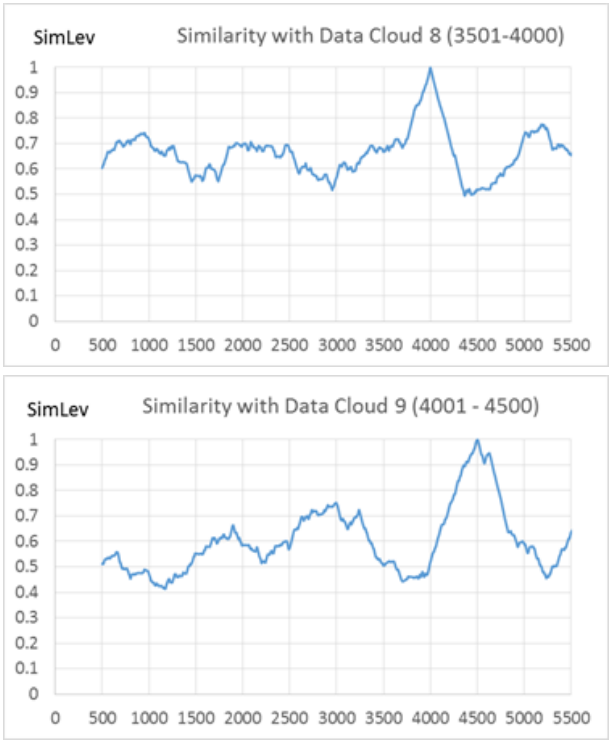

Fig. 18. Performance results from the monitoring system with 5 reference models (5 anomalies) as follows: *Data Cloud 2, 4, 7, 8 and 9.*

These results can be also used for detecting the lengths (duration) of the time periods at which the operation of the plant approaches certain anomaly with a high similarity level (for example *0.8*) or higher.

VII. Conclusions

The proposed monitoring system for detection of anomaly in plant operation is based on a supervised learning method. This requires a previously known example (data cloud) of known anomaly in the plant by recording the values of the data stream within the time interval of this anomaly.

The method for creating the data cloud models in this paper is based on using a predefined mesh of grid cells that produce two important parameters: number and location of the active grid cells as well as the data density at each grid cell. Then the similarity level between two data clouds (*reference* and *current*) is calculated by using these two parameters from the respective data cloud models. The monitoring system can work in online mode continuously following the coming data samplings from the endless data stream.

There are some directions for a further research in order to improve the performance and plausibility of the monitoring system. First, the influence of the number of the grid cells for each dimension to the accuracy of the results should be analyzed. Then a proposal for an automatic selection of this number could be considered. Second, the effect of the noisy data to the accuracy (plausibility) of the monitoring results could be investigated. Third, some other variants for calculation of the similarity level could be considered, developed and compared in a search for a better performance.

Finally, the use of the proposed monitoring system as a tool for knowledge extraction from real operation data could be considered.

Acknowledgment

The author highly appreciates the technical support and permission from SOCAR for getting access to real operation data from a Refinery plant in order to prove the correctness and applicability of the proposed method and algorithm for the monitoring system.

References

[1] V. Chandola, A. Banerjee, and V. Kumar, Anomaly detection: A survey, *ACM Computing Surveys* 41(3), Article 15, 2009, DOI: 10.1145/1541880.1541882, pp. 1-72.

[2] J.L. Zhou, Y. Fu, Y. Wu et al. "Anomaly detection over concept drifting data streams", Journal of Computational Information Systems, v. 5 (6), 2009, pp. 1697-1703.

[3] Zh. Ding and M. Fel, "An anomaly detection approach based on isolation forest algorithm for streaming data using sliding window", Proc. of the 3rd *IFAC ICONS 2013 Int. Conference on Intelligent Control and Automation Science*, Chengdu, China, 2013, pp. 12-17.

[4] M. Gong, M. J. Zhao, J. Liu, Q. Miao, and L.Jiao, "Change detection in synthetic aperture radar images based on deep neural networks", *IEEE Trans. Neural Networks and Learning Systems*, Vol. 27, No. 1, 2016, pp. 125-138.

[5] G. Vachkov, A. Alili, and M. Namazov, "Grid fuzzy models with variable boundaries and their application to monitoring of plant operations", Proc. of the *IEEE ICMA-2017 Int. Conference on Mechatronics and Automation,* Takamatsu, Japan, August, 2017, pp. 273-1278.

[6] G. Vachkov and A. Tzanev, "Similarity analysis of large data sets by use of grid fuzzy models and fuzzy decision making", Proc. of the IFAC *TECIS-2018* Confaderence, Baku, Azerbaijan, September, 2018, pp. 257-262.

[7] G. Vachkov,"Data stream mining for Anomaly and Change detection in continuous plant operation", Proc. of the IFAC *TECIS-2019* Conference, Sozopol, Bulgaria, September, 2019, in press.

Journal of Engineering Sciences & Modern Technologies
ISSN 3078-1760, E-ISSN 3078-1965
Volume 1, Number 1, 2025, page 40-42

BAKI ALİ NEFT MƏKTƏBİ
BAKU HIGHER OIL SCHOOL

https://jesmt.org/

https://doi.org/10.70334/3078-1965.2025.1.40

UDC 004.932

Fire detection using image processing

Leyla Muradkhanli

Baku Higher Oil School, Department of Process Automation Engineering, Baku, Azerbaijan
leyla.muradkhanli@bhos.edu.az

Keywords:

Fire Detection System,
Image Processing,
Computer Vision,
Edge Detection

A B S T R A C T

A number of methods have been developed to detect fire. The working principle of conventional fire detectors is based on physical properties of fire (e.g., smoke, heat, temperature).

This paper describes the detection of fire by processing images of fire. Image processing and computer vision techniques are used to extract key characteristics of fire detection. The algorithm combines color information of the fire with the edge of the fire information. Based on the combined results of both techniques, a parameter is created to segment out the necessary details from the images to detect and identify the fire. The source code for fire detection is written in MATLAB. 30 sample images were tested to detect fire to test the performance of the algorithm introduced in this paper.

Received: 01.01.2020
Accept: 03.11.2023

I. Introduction

Industrial fires lead to injuries and fatalities by leaving damaged properties and facilities behind. The result of fires could leave unamendable effects on people, nature and industrial facilities. Disastrous events can be avoided by timely detecting fire and taking the appropriate measures.

Early detection of fire is very important to reduce the losses due to hazardous fire. Traditional fire detection systems like sensor based methods have many disadvantages:

- they cannot be used everywhere;
- they are not reliable in open space and windy conditions;
- they have transmission delay;
- false alarm rate is high;
- they cannot provide sufficient information about fire's size, location and dynamics.

Conventional fire detection techniques are based on the particle sampling, temperature sampling, relative humidity sampling, air transparency testing and smoke analysis in addition to the traditional ultraviolet and infrared sampling. Therefore, fire detection techniques depend on the byproducts of the combustible. In case of a fire, minimum detection latency is crucial to minimize the damages to the property and save lives. These sensors are inherently suffered from the time delay from the fire to the sensor. Furthermore, these are point sensors, looking at a point and the fire may not affect that point. Therefore, the reliability of the conventional fire detection systems mainly depends on the positional distribution of the sensors. The system to be more accurate the sensors shall be densely distributed [1].

Vision based fire detection system allows to overcome these problems and offers the following advantages:

- low cost
- simple implementation
- early and fast detection
- providing visual information about the location and state of fire.

This paper describes fire detection using image processing and computer vision.

II. Vision Based Systems

Vision based fire detection systems extracts and uses for fire detection information about color, motion and geometry. Block diagram of fire detection system is shown in Figure 1.

In this paper we use algorithm that combine color information of the fire with the edge of the fire information. As a result, parameter is created for segmentation the details from the images to detect and identify fire.

The first step is to detect the color of the fire which is mostly red in color. Then we used the sobel and canny edge detection to detect the edge of the fire while removing threshold which is less than 100. Based on the results of color detection and edge detection we applied the segmentation technique to separate the region of interest (ROI) of the fire from the background.

Color is a very important criterion of the fire. It involves chromatic/color analysis of the images to search for regions with fire colors using one or more decision rules in color spaces. Usually, the RGB (Red Green Blue) color space is used but other color spaces as HSV, HSI (Hue Saturation Intensity) or YCbCr (Luminance ChrominanceBlue ChrominanceRed) have also been used in the literature.

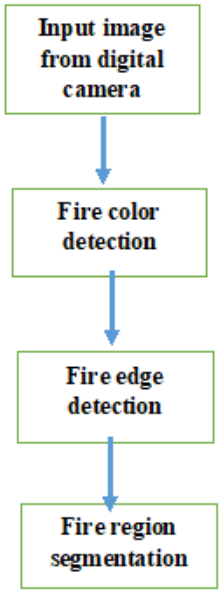

Fig. 1. Fire detection using image processing

In order to create the color model for fire we analyzed several images having fire. Since the color of fire is generally closer to red and has high illumination, and we can use this property to derive the required color model.

RGB Color Model

A fire image can be described by using its color properties. There are three different element of color pixel: R, G and B. The color pixel can be extracted into these three individual elements R, G and B, which is used for color detection.

RGB color model is used to detect red color information in image. In terms of RGB values, the corresponding inter-relation between R, G and B color channels: R>G and G>B. The combined condition for the captured image can be written as: R>G>B. In fire color detection R should be more stressed then the other component, and hence R becomes the domination color channel in an RGB image for fire.

This imposes the condition for R as to be over some pre-determined threshold value RTH.

All of these conditions for fire color in image are summarized as following:

Condition1: R > RTH

Condition2: R > G > B.

Where RTH is the Red color threshold value for fire.

Then the result, is need to convert to HSI color model where H represent hue, S represent saturation and I represent intensity.

Edge Detection

Edge detection technique is used to detect the color variance in an image. The edge detection system compares the intensity difference in the image and it provides an image with black and white color space where high intensity area is white color and low intensity area is black color.

The intensity difference is categorized using a global intensity threshold which is separately calculated for each image by MATLAB the output will provide a shape of the flame. Thus, the edge detection can be used to analyze color detection of fire. After getting the output from the color detection we can apply different detection techniques by mapping these detected coordinate on its corresponding original image with different combinations.

In this paper we use the canny color edge detection techniques because these techniques give the better performance as compared to other techniques. In this method first read the color image and divides it into its three separate color channels. Each color channel run through the Canny color edge detector separately to find a resulting colored edge map. Combine the resulting edge maps from each of the three color channels into one complete edge map. For this step it is found that a simple additive approach provided the best results. So if there was an edge in any of the three colored edge maps, we added it to the general edge map.

Segmentation Technique

The final technique used in this algorithm is segmentation technique which was used to segmented fire from the non-fire background. The first step done by this technique is to specific the color range for segmented process in the ROI. The following formula is used:

$$D(x,m) = \|x - m\| = \{(x,m)^T (x-m)\}^{1/2} =$$
$$= [(x_R - m_R)2 + (x_G - m_G)2 + (x_B - m_B)]^{1/2}$$

III. Experimental Results and Analysis

In proposed work it has been done edge detection by using canny color edge detection method as compared with the other methods. Figure 2 shows the original image. We found the flame by using different technique such as color canny, sobel, Prewitt. From this result conclude that as compared with the other methods color canny method gives better performance. Figure 3 shows the result of edge detection by using sobel and canny color edge detection techniques. After edge detection next parameter is to find motion of fire.

The results and ROI of the fire are shown in Figure 4 and 5.

Fig. 2. Original image

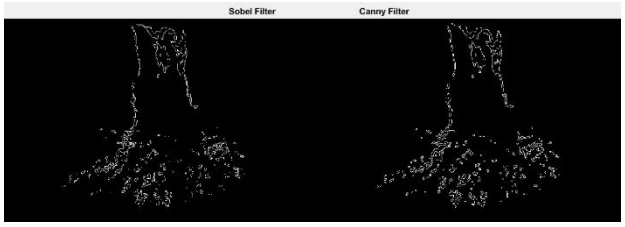

Fig. 3. Edge detection

Fig. 4. The results

Fig. 5. ROI of the fire

Finally, validation was carried out to evaluate the algorithm based on the 30 images. This validation process uses a truth model, with which the results was compared. The true positive (TP) and true negatives (TN) are correct classification. A false positive (FP) is when the outcome of the algorithm is incorrectly predicted, when the in reality it is actually present in the image.

The accuracy of the algorithm specifies the ability of the algorithm in detecting the ROI.

Accuracy = TP/(TP+TN) × 100%

The efficiency test is given as

Efficiency = (TN+TP/TN+TP+FN+FP) × 100%

IV. Conclusion

The algorithm uses RGB color model to detect the color of the fire which is mainly comprehended by the intensity of the component R which is red color. The growth of fire is detected using sobel edge detection. Finally, a color based segmentation technique was applied based on the results from both these techniques to identify the ROI of the fire. The algorithm works very well when there is a fire outbreak. The overall accuracy of the algorithm is greater than 90%, indicating the effectiveness and usefulness of the algorithm. The efficiency of the algorithm currently is 87% and will be improved in future works.

Fire detection using image processing have been used in this work. In order to test the performance of the algorithm introduced in this paper, test conducted on 30 sample images. The images, obtained from different sources contain fire images in different situations. It is important to note, the fire detection method proposed in this paper is experimental and the quality of results could vary. The requirements of fire detection could change based on the fire type, environment and lighting conditions.

References

[1] X.L. Zhou, F.X. Yu, Y.C. Wen, and Z.M. Lu. G.H. Song, "Early fire detection based on flame contours in video," Information Technology Journal, vol.9, no.5, pp 899-908, 2010.

[2] K. Poobalan and S. Liew "Fire detection algorithm using image processing techniques" Proceeding of the 3rd International Conference on Artificial Intelligence and Computer Science (AICS2015), 12-13 October 2015, Penang, Malaysia.

Journal of Engineering Sciences & Modern Technologies
ISSN 3078-1760, E-ISSN 3078-1965
Volume 1, Number 1, 2025, page 43-46

BAKI ALİ NEFT MƏKTƏBİ
BAKU HIGHER OIL SCHOOL

https://jesmt.org/

https://doi.org/10.70334/3078-1965.2025.1.43

UDC 004.12

Using of multifractal analysis for electromyographic signals to detect limbs asymmetry

Kamala Pashayeva

Baku Higher Oil School, Department of Process Automation Engineering, Baku, Azerbaijan
kamala.pashayeva@bhos .edu.az

Keywords:

Multifractal analysis,
Electromyography,
Limb Asymmetry,
Hurst Index,
Renyi Index

A B S T R A C T

The paper studies the possibility of using the multifractal analysis method to quantify the asymmetry of the patient's muscles. Signals received from Quadriceps femoris muscle, Gastrocnemius muscle, Biceps femoris muscle are used in the experiment. The results are indicative of how the Hurst index and the Renyi index values, being informative and used as the main characteristics of multifractals, can be used to detect violations of limb asymmetry.

Received: 15.06.2024
Accept: 15.08.2024

I. Introduction

Despite the fact that in reality the symmetry of the human body is not absolute, it is considered to be its mirror image. There are types of asymmetry, which are the cause of pathological disorders, which as a result can lead to serious pathologies.

Muscular imbalance is a violation of the balance of the amount of opposing forces between the muscles. Asymmetry of muscle mass and unbalanced muscle tone can lead even to the irregularity of the skeletal structure, and therefore the problem of identifying and treating these disorders remains highly relevant [1,2].

The study of the signals of biological systems must be carried out taking into account such significant factors as the essentially nonlinear nature of the relationship between different physiological indices and between the counts of biological signals taken from symmetric human organs. An essential limitation for the application of classical methods of analyzing biological signals is their non-stationarity.

The chaotic nature of the dynamic processes of the biological system and the fractal properties of bio-signals obtained from various body structures require the description of processes occurring in these systems with the use of nonlinear dynamics, dynamic chaos theory, fractal analysis, interval statistics analysis, etc. Using such analysis methods, it is possible to obtain diagnostic informative indicators inherent in each of the methods that can serve as early harbingers of the disease of a particular organ.

In this paper we consider the estimation of the fluctuation component of random processes using the method of fluctuation analysis of electromyographic signals. The significance of these signals is represented in the form of a dynamic time series for assessing the asymmetry of the limbs of the human body.

There are not a large number of publications in the science-based databases using the multifractal approach for the analysis of the myographic signal. In [5], the author used fractal analysis to evaluate the morphological complexities of the surface of the connecting parts scanned by the 3D scanner. The authors [6] tested the possibility of predicting the asymmetry of electromyographic signals from limbs (arms and legs) by the method of multifractal sets. To establish the connection between the imbalance of the jaw and the loss of muscle strength of the hand using surface electromyography, the fractal dimension of Higuchi was used [7].

In [8], examples of changes in the fluctuation functions of the electromyographic signal for different levels of loading on a specific muscle are given.

In this paper, electromyographic signals are comparable limbs: the right and left parts of the hip muscles. In contrast to the classical approach to evaluating asymmetry using a single point (maximum) of the measured signal, we consider the set U of measured limb signals as inhomogeneous nonuniformly distributed points of the fractal set. To assess the randomness of myographic signals, one can use the characteristics of fractal sets, such as the Hausdorff fractal dimension, the Hurst exponent, the generalized dimension, the correlation and information dimension [9-11].

II. Methods

At present, in clinical conditions, asymmetry is assessed by the maximum value of the amplitude of muscle strength. Despite the fact that, this process includes "maximum muscle contractility - reaching the peak - the maximum relaxation of the muscle", as an informative result only the peak value is taken into account. If we consider the whole process as a dynamic time series, then to make a decision it is necessary to take into account the contribution of all the elements of the aggregate that creates this process. To study all the data of the dynamic series and the minimum step of the window size in one count, it is necessary to ensure the multiplicity of the record length and the window size. For this, the segmentation is performed in two passes, performed in opposite directions.

The calculation algorithm consists of the following steps.

First, from the series *x(k), k=0,1,2…N* we isolate the total fluctuation (or fluctuation profile).

$$Y(i)=\sum_{k=1}^{i}\left[x(k)-\bar{x}\right],\ i=1,2,...N \qquad (1)$$

where $\bar{x}$ is the arithmetic mean of the series *x(κ).*

We divide the entire interval [1,N] into N_s=[N/s] segments, each of which contains s values. Elements of the new interval are $x_{(\nu-1)s+1},\ldots, x_{\nu_i S}$, $\nu=1,\ldots, N_s$. It should be borne in mind that in the case s>N/4 the function of the deformed variance loses statistical informativity because of the smallness of the number N_s<4, used in averaging. In this case, the inequality s<10 must be satisfied [13-15].

Since the change in the random variable $Y_{(i)}$ occurs near $y_\nu(i)\neq 0$ we find the polynomial for this function using the least squares method, and calculate the variance in the interval ν:

$$F^2(\nu,s)=\frac{1}{s}\sum_{i=1}^{s}\{y[(\nu-1)s+i]-y_\nu(i)\}^2 \qquad (2)$$

for segments $\nu=1,2,\ldots N_s$, in the case when the decomposition is performed in the forward direction, and for the negative sequence $\nu=N_s+1,\ldots,2N_s$ we use the equality

$$F^2(\nu,s)=\frac{1}{s}\sum_{i=1}^{s}\{y[N-(\nu-N_s)s+i]-y_\nu(i)\}^2 \qquad (3)$$

We average the deformed variance over the intervals

$$F_q(s)=\left\{\frac{1}{2N_s}\sum_{\nu}^{2N_s}[F^2(\nu,s)]^{q/2}\right\}^{1/q} \qquad (4)$$

The coefficient 2 in the denominator and in the upper limit of the sum are used only when the algorithm with a double pass is reflexed.

For zero order q, this equation contains the uncertainty, and then by definition

$$F_0(s)=\exp\left\{\frac{1}{4N_s}\sum_{\nu=1}^{2N_s}\ln[F^2(\nu,s)]\right\} \qquad (5)$$

In order to find the dependence $F_q(s)$, we change the time scale s of the fixed exponent *q* and represent it in double logarithmic coordinates.

If the series under investigation reduces to a self-similar set ($s\to 0$), then the scaling relation

$$F_q(s)\sim s^{h(q)} \qquad (6)$$

where h(1) is the generalized Hurst exponent [10]. For stationary time series, h(2)=H is the known exponent of Hurst's degree, which, on the one hand, does not depend on *q*, and on the other hand the variance is the same for all segments. With a positive/negative value of q, h(q) indicates the scaling behavior of segments with large/ small fluctuations [13].

For small values of s, h(q) we determine from the linear regression [14]

$$F_q(s)=h(q)\cdot\ln(s) \qquad (7)$$

The standard representation of the scaling properties of the time series assumes a transition from the Hurst exponent h(q) to the mass exponent τ(q) and the spectral function f(α), the Renyi dimension, which are the main characteristics of multifractals [15].

The mass index is calculated by the formula

$$\tau(q)=qh(q)-1 \qquad (8)$$

The spectral function has a connection with the mass index and the Hurst index:

$$\alpha(q)=\frac{d\tau(q)}{dq}=h(q)+q\frac{dh}{dq}$$

$$f(\alpha)=1+q(\alpha)[\alpha-h(q(\alpha))] \qquad (9)$$

where α is the Holder exponent estimating the probability of the element of the fractal set falling into the ν-th fragment.

The Renyi dimension is determined from the equality of the spectral function (8) and is equal to:

$$D(q)=\frac{qh(q)-1}{q-1}, \qquad (10)$$

As we see, the equality does not hold when q=1. For this value, according to Lopital's rule [14], we use the dependence:

$$D(1) = h(1) + \left.\frac{\partial h}{\partial q}\right|_{q=1} \qquad (11)$$

III. Results and Disscusions

The calculation is performed for each set of muscle separately.

Muscle signals are used in the experiments: Quadriceps femoris muscle - rectus femoris, Quadriceps femoris muscle - vastus lateralis, Quadriceps femoris muscle - vastus medialis, Gastrocnemius muscle - lateral part, Gastrocnemius muscle - medial part, Biceps femoris muscle - for the left and the right parts, respectively.

In accordance with the above algorithm, the medical recordings of the muscles Quadriceps femoris muscle-vastus lateralis, obtained by the ME6000 16-channel electromyograph in the lateral and medial muscle parts (right and left) were used for the computational experiment.

The signals are denoted by $x_l(k)$ - for the derivation of the left side, $x_r(k)$ - for the derivation of the right-hand side. Each signal was divided into 5 segments (N_s=5). In the time series, in both directions $x_l(k)s$=83 and in $x_r(k)s$=83.

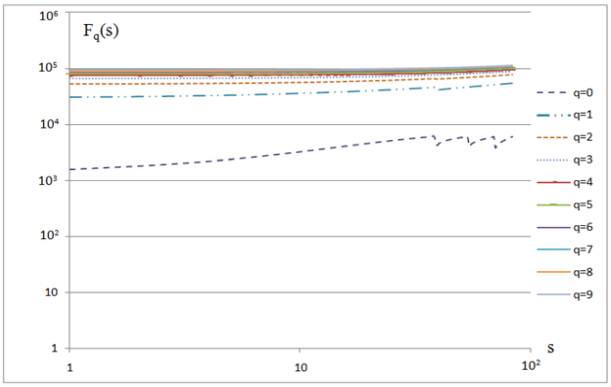

(a)

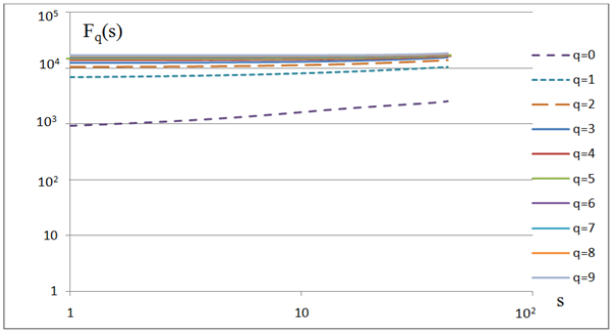

(b)

Fig.1. Dependence of the dispersion of Quadriceps femoris muscle-vastus lateralis on the size of the segment s ((a)–s=83, (b)–s=43) for different values of the strain parameter q(q=1-9).

The dependence $F_q(s)$ for various values of $q = \overline{1,9}$ is obtained after taking into account the trend in formulas (2) and (3) - Fig. 1. For values of q<0 and q>4, there is so little difference that one can say that they repeat (Fig. 1) and with this, these values lose their significance. This is also found in the values of the Renyi index calculated using (9) (Fig. 3).

The obtained results of the Hurst index are shown in Fig. 2. For values of q>2, one can observe a well-marked value of the indicator, which makes it possible to use it as an information indicator. Between the values of h(q) the relation $h^{L}_{(q)} > h^{R}_{(q)}$ is determined and this is observed for positive values of q.

Denoting $D_q^{(L)}$ and $D_q^{(R)}$ of the parameter D_q obtained from the measurement values of the left and right parts of the muscle Quadriceps femoris muscle-vastus lateralis patient. From Fig. 3 it is easy to determine the relation

$$D_q^{(L)} > D_q^{(R)}$$

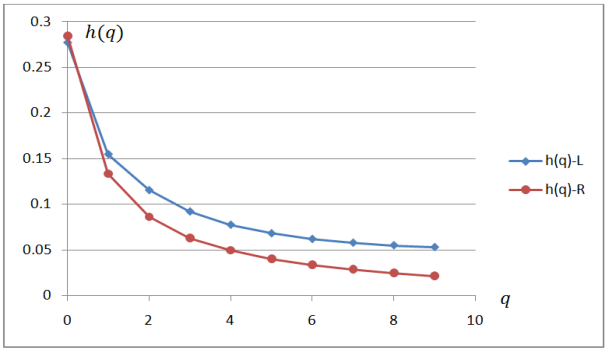

Fig. 2. Graphs of the Hurst exponent for the left and right sides

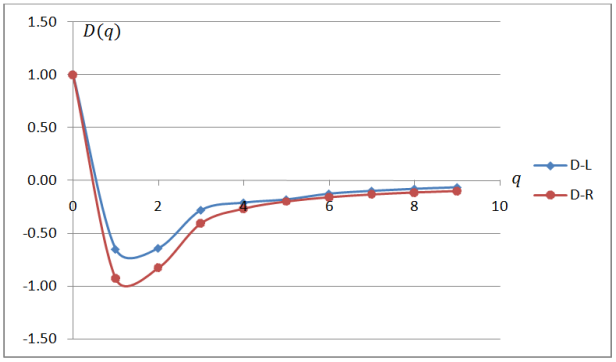

Fig.3. Result of the Renyi index for the right and left sides

This inequality holds for 0<q<4, and for other values we get duplicate values (this can be seen from the graphs), which lose their diagnostic value

$$D_q^{(L)} = D_q^{(R)}$$

The computational value of the spectral function f (α) is shown in Fig.4.

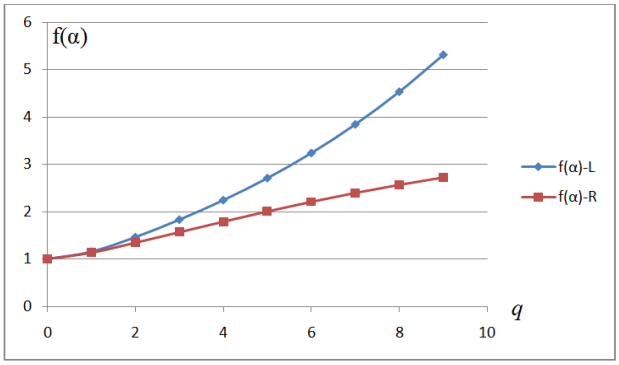

Fig.4. The graphs of the spectral function f (α) for the right and left parts

As in the graphs showing Hurst (Fig. 2), here too, a good correlation is found in the values of q>2. As the value of q increases in the signals of the left side of the muscles, the values of f (α) increase in comparison to the value of the right-hand side

$$f_q^{(L)} > f_q^{(R)}$$

IV. Conclusion

The results show that the proposed method is also acceptable for analysis of the detection of asymmetry in the limbs of a person. It can be considered that the quantities that are used as the main characteristics of multifractals is informative which can be used to detect violations of limb asymmetry. The results obtained show that to determine the asymmetry of the extremities, it is advisable to use the Hurst index and the value of the spectral function, since the informative range is wider than the Renyi index.

References

[1] M. Rynkiewicz, T. Rynkiewicz, P.Zurek, E.Zicmann, R. Szymanik. Asymmetry of muscle mass distribution in tennis players. Trends in Sport Sciences. 2013; 1 (20): p. 47-53

[2] http://www.bonamedica.ru/assimmetrii-cheloveka/

[3] E. L. Goldberger, D.R. Rigny, B.J. West. Chaos and fractals in human physiology. www.kozlenkoa.narod.ru/docs/fractal2.docx

[4] V.V. Isayeva. Fractal and chaotic patterns in the morphology of animals. Proceedings of the Zoological Institute of the Russian Academy of Sciences Appendix No. 1, 2009, p. 199-218

[5] A. Zumwalt. A New Method for Quantifying the Complexity of Muscle Attachment Sites. The Anatomical Record (Part B: New Anat.) 286B: 21-28, 2005

[6] D.G. Stephen, A.Hajnal. Transfer of Calibration Between Hand and Foot: Functional Equivalence and Fractal Fluctuations. Atten Percept Psychophys. (2011) 73: 1302-1328

[7] Kh. T. Q. Dang, H. L. Minh et al. Analyzing surface EMG signals to determine the relationship between jaw imbalance and arm strength loss. BioMedical Engineering Online 2012

[8] M.I. Bogachev, K.E. Gromova, D.M. Klionsky. Fluctuation analysis of physiological signals. //Izd.VUZov of Russia. Radioelectronics, 2012, issue 6, p.37-45

[9] H.O.Paitgen, H.Jurgens, D.Saupe. Chaos and fractals: New frontiers of science. New York, Springer-Verlag, 1992, -984p.

[10] E. Feder. Fractals. -M. : The World, 2001, -260 pp.

[11] A.A. Gorshenkov, Yu.N. Klikushin. Methods for estimating the chaos of signals. Polzunovsky Herald, No. 3 (1), 2011, p. 30-33

[12] J.W. Kantelhardt, S.A. Zschienger, E. Koscielny-Bumde, S.Havlin, A.Bumde, H.E. Stanley. Multifractal detrended fluctuation analysis of non-stationary time series. Physica A, 2002, v.316, p.87-114

[13] P. Mali, A. Mukhopadhyay. Multifractal characterization of the gold market: a multifractal detrended fluctuation analysis. Physica A: Statistical Mechanics and its Applications 413: 2014, p. 361-372

[14] N.T. Abdullaev, OA Dyshin, G.T. Hasmamedov. Diagnosis of the state of the cardiovascular system on the basis of fractal analysis of RR-intervalograms. "Biomedical radioelectronics", 2010, N12, p.25-29

[15] A.I. Olemsky, V.N. Borisyuk, I.A. Shuda. Multifractal analysis of time series. Bulletin of SumDU, №2, 2008, p.70-81.

Journal of Engineering Sciences & Modern Technologies
ISSN 3078-1760, E-ISSN 3078-1965
Volume 1, Number 1, 2025, page 47-50

BAKI ALİ NEFT MƏKTƏBİ
BAKU HIGHER OIL SCHOOL

https://jesmt.org/

https://doi.org/10.70334/3078-1965.2025.1.47

UDC 543

Synthesis and study of surface-active salts based on propoxy derivatives of octylamine, hexadecylamine and hydrochloric acid

Sevda Zargarova[a], Ilhama Zarbaliyeva[b], Saida Huseynova[c]

[a]Baku Higher Oil School, Vice-rector for teaching and scientific affairs, Baku, Azerbaijan, sevda.zargarova@bhos.edu.az
[b]Baku Higher Oil School, Scientific Secretary in the administration, ilhama.zarbaliyeva@bhos.edu.az
[c]Institute of Petrochemical Processes of ANAS, seidehuseyn74@mail.ru

Keywords:

Octylamine;
Hexadecylamine;
Propoxy derivatives;
Hydrochloric acid;
Surfactant;
Petrocollecting;

ABSTRACT

Salts of the oligomeric propoxy derivatives of octylamine and hexadecylamine with hydrochloric acid were synthesized. Structure and composition of the salts were confirmed by using IR spectroscopy. Surface tension and electroconductivity properties of the oligomers were examined and corresponding main parameters of the salts were calculated. Moreover, petrocollecting properties of these salts were determined and maximum values of petrocollecting coefficients were calculated.

Received: 22.05.2024
Accept: 19.08.2024

I. Introduction

It is well known that demand for crude oil and petrochemical product and usage of them increase from year to year. Such increase of demand to crude oil and products of its refining results in ecological instability and disbalance. In order to improve ecological balance of the nature, surfactants are used in industry including oil production and refining [1,2]. Thin oil layers on the surface of the water become one of such ecological problems which may occur during transportation of crude oil and its refining products.

According to the literature, higher aliphatic amines may be used for synthesis of surface-active compounds [3-8]. Beside surface activity, such components are able to decrease surface area of thin pertoleum layers several times on the surface of water [3-5]. In a given study, surfactants are obtained from octylamine, hexadecylamine, propylene oxide and hydrochloric acids. Main physical-chemical properties of the new surfactants including colloidal-chemical ones were determined in order to apply them as petrocollecting agents.

II. Experimental

Octylamine was a product of "Alfa Aesar GmbH & Co KG" firm (Germany) of purity > 98%.

Hexadecylamine was a product of "Alfa Aesar GmbH & Co KG" firm (Germany) of purity > 98%.

Propylene oxide was a product "Organic Synthesis" factory (Sumgayit, Azerbaijan) of 99.97-99.98% purity.

Hydrochloric acid was "analytically pure" grade product of "Uralximinvest" (Russia) of >37% purity.

Potassium hydroxide was used as "analytically pure" product of "Chemapol" firm (Czech Republic).

Oligomers based on octylamine, hexadecylamine and propylene oxide were synthesized at 140-150°C for 13-14 hours in an autoclave made of stainless steel and equipped with a regulator of temperature. In the given reaction, potassium hydroxide was used as a catalyst. In the second

step, propoxy derivatives of the octylamine and hexadecylamine reacted with hydrochoric acid at 25°C for 5-6 hours in order to obtain salts.

All salts are liquids of yellow-brown color.

IR spectra were recorded by using an ALPHA FT-IR spectrometer (Bruker, USA) using KBr tablets.

Surface tension (γ) values were measured by Du Nouy ring method using a KSV Sigma 702 tensiometer (Finland).

Specific electroconductivity (κ) values were determined by "Anion-4120" electroconductometer (Russia).

III. Resuls and Their Discussion

The reaction between alkylamine (octylamine or hexadecylamine) and propylene oxide is illustrated as following:

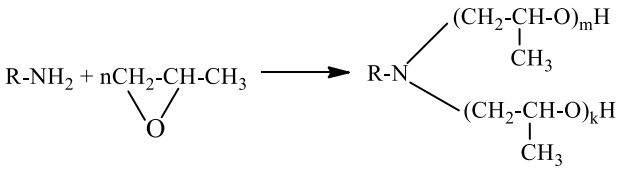

where R is octyl or hexadecyl group, n=m+k. Values of n are equal to 2.74 for octylamine propoxy derivative and 10.02 for hexadecylamine propoxy derivative.

In the second step, propoxy derivatives of the octylamine and hexadecylamine were reacted with hydrochloric acid as following:

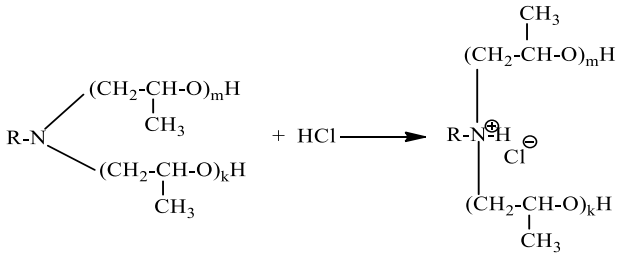

Structure and composition of the final products were analyzed by using IR spectroscopy. The IR-spectra are given in Figure 1.

By examining IR spectra, it was deduced that absorption bands at 3345.25 cm^{-1} in the first spectrum, 3354.50cm^{-1} in the second spectrum represent O-H valent vibration bands. C-H valent vibration bands of C-H bonds in CH_3, CH_2 and CH groups are observed at 2957.29-2856.33cm^{-1} in the first spectrum, at 2968.20-2853.33cm^{-1} in the second spectrum. N-H deformational vibrations bands exist at 1645.85cm^{-1} in the 1st and 1638.58 cm^{-1} in the 2nd spectra. C-H deformational vibration bands are at 1458.87-1377.38 cm^{-1} and 1458.06-1374.87cm^{-1}, respectively in the first and second spectra. C-N valence vibration bands are at 1293.08cm^{-1} (1st spectrum) and 1290.55cm^{-1} (2nd spectrum). C-O valent vibrations band of C-OH group can be defined at 1078.90 cm^{-1} in Salt 1 spectrum and 1089.96cm^{-1} in Salt 2 spectrum. $(CH_2)_x$ "pendulum"vibrations bands exist at 722.44 cm^{-1} in the first spectrum and 720.62 cm^{-1} in the second spectrum.

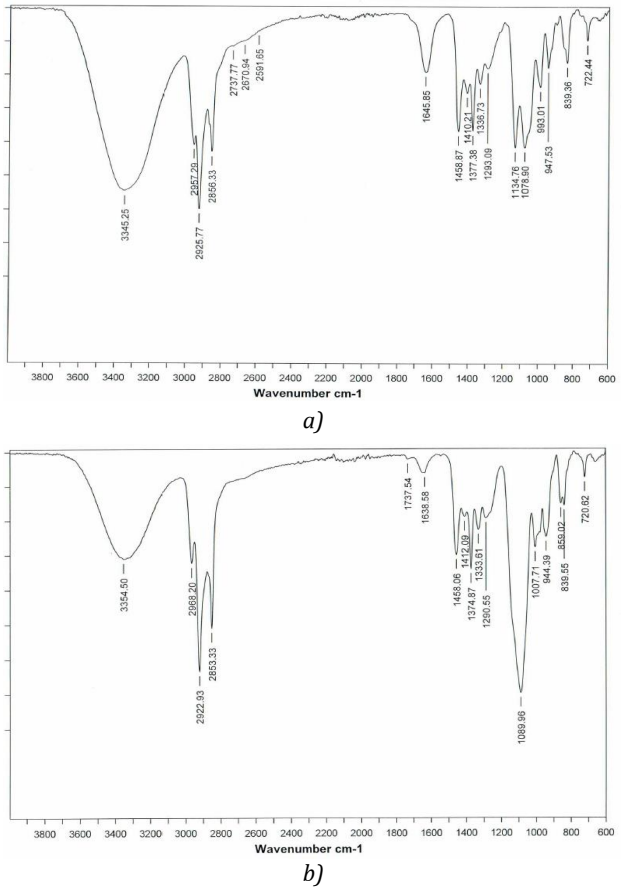

Fig 1. IR spectra of the synthesized hydrochloride salts of a) octylamine propoxy derivative (n=2.74) and b) hexadecylamine propoxy derivative (n=10.02)

Surface tension data of hydrochloride salts of alkyamine propoxy derivatives were determined at temperatures 20°C. γ versus concentration (c) plots of the components are given in Figure 2.

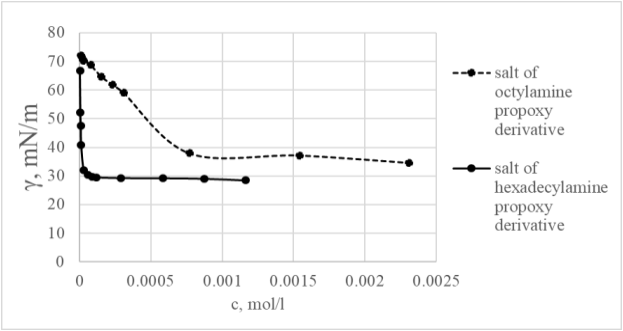

Fig 2. Surface tension at the water-air border versus concentration plots of the salts

Bu using these plots of the salts, characteristic parameters of the surface activity can be determined. Critical micelle concentrations (CMC), γ_{CMC}, surface pressure (π_{CMC}), C_{20} (the concentration

for reduction of γ by 20 mN/m), adsorption efficiency ($pC_{20}=-logC_{20}$) as well as CMC/C_{20} values of the all salts were determined according to [9] and given in Table 1.

Maximum surface excess concentration - Γ_{max} values were calculated from the following equation:

$$\Gamma_{max} = -\frac{1}{n * R * T} * \lim_{c \to c_{CMC}} \frac{d\,\gamma}{d\,lnc}$$

where R is universal gas constant (R=8.3145 C/mol*K) and T is absolute temperature. The value of n was taken as 2 because 2 ions are formed by dissociation of the salts.

The minimum value of the area for one surfactant molecule of the salts at the water-air border (A_{min}) were determined by the given equation

$$A_{min} = \frac{10^{16}}{N_A \times \Gamma_{max}}$$

and tabulated in Table 1.

Table 1. Surface activity parameters of the synthesized surface-active salts

Surfactant	CMC×10^4 (mol/L)	γ_{CMC} (mN/m)	π_{CMC} (mN/m)	$C_{20}\times10^5$ (mol/L)	pC_{20}	$\Gamma_{max}\times10^{10}$ (mol/cm^2)	$A_{min}\times10^2$ (nm^2)
Hydrochloride salt of octaylamine propoxy derivatite	7.70	37.95	34.05	46.30	3.33	1.19	139.28
Hydrochloride salt of hexadecylamine propoxy derivatite	0.87	29.74	42.26	0.58	5.23	2.11	78.81

Specific electrical conductivity dependence on concentration was studied for hydrochloride salt of octylamine propoxy derivative at 21.8°C and hexadecylamine propoxy derivative at 26.4°C. Isotherms of the specific electrical conductivity were plotted and given in Figure 3:

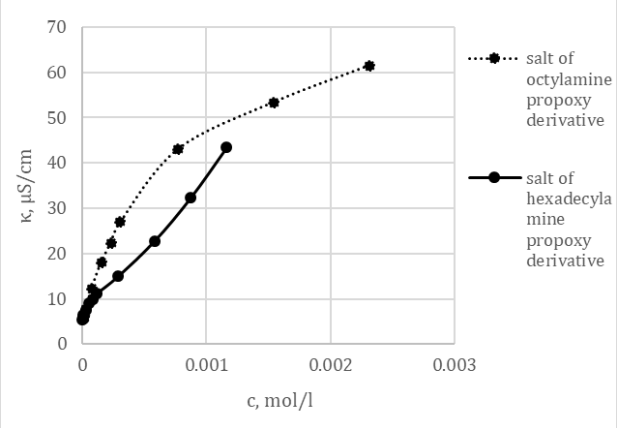

Fig 3. Specific electrical conductivity versus concentration plots of the hydrochloride salts of alkylamines (C_8 and C_{16}) propoxy derivatives

Table 2. Specific electrical conductivity parameters and thermodynamic parameters of micellization and adsorption of the hydrochloride salts of alkylamines (C_8 and C_{16}) propoxy derivatives.

Surfactant	α	β	ΔG_{mic}, kJ/mol	ΔG_{ad}, kJ/mol
Salt of octylamine propoxy derivative	0.24	0.76	-31.27	-34.13
Salt of hexadecylamine propoxy derivative	0.59	0.41	-32.67	-34.68

Slopes of the straight line before (S_1) and after (S_2) CMC value of each salt were determined. Such thermodynamic properties as Gibbs free energy of micellization (ΔG_{mic}) and Gibbs free energy of adsorption (ΔG_{ad}) values were calculated according to the following equations:

$$\Delta G_{mic} = (2-\alpha) \times R \times T \times \ln(CMC)$$

$$\Delta G_{ad} = (2-\alpha) \times R \times T \times \ln(CMC) - 0.6023 \times \pi_{CMC} \times A_{CMC}$$

where A_{CMC} is surface area of the one surfactant molecule at the interface in terms of Å^2.

As is seen, the ΔG_{ad} values are more negative than the ΔG_{mic} values which points out to preference of the adsorption of the surfactants rather than the micelle formation.

In order to identify petrocollecting property of the surface-active salts, unthinned reagents, 5% wt. aqueous and ethanolic solutions of the salts were separately added to the water with thin petroleum layer. Thin layer (~0.17 mm) of Pirallahi) petroleum was formed on the surface of 40 ml distilled, tap and sea (the Caspian) water in Petri dishes. For each salt, maximum duration of the petrocollecting action and petrocollecting coefficient-K at room temperature were determined and given in Table 3. The value of "K" is derived as the ratio of the area of the surface of initial petroleum film and the area of the surface of the petroleum spot formed under the action of the salts.

As becomes evident from the obtained data, both of the salts have petrocollecting property. Experimental durations (τ) can be considered as the same for both situations and ended with drying of the waters in Petri dishes. For the used waters, petroleum collecting coefficients are between 22 and 29. It can be deduced that, alkyl radicals in the considered alkylamine propoxy derivatives are not dominant factors for petrocolllecting coeffients.

Table 3. Maximum duration of petrocollecting action and petrocollecting coefficients of the synthesized hydrochloride salts of alkylamines (C_8 and C_{16}) propoxy derivatives

Salt	State of surfactant	Duration, hours-τ	K		
			Distilled water	Tap water	Sea water
Hydrochlorid salt of octylamine propoxy derivative (n=2.74)	Unthinned reagent	0.17-6	29.44	29.44	29.44
		25-72	22.08	22.08	22.08
		115	22.08, drying	22.08, drying	22.08, drying
	5% wt. aqueous solution	0.17-6	36.80	33.97	33.97
		25-72	29.44	29.44	29.44
		115	29.44, drying	29.44, drying	29.44, drying
	5% wt. ethanolic solution	0.17-6	33.28	33.97	33.97
		25-29	25.00	25.00	29.44
		48-72	21.97	21.97	22.08
		115	21.97, drying	21.97, drying	22.08, drying
Hydrochlorid salt of hexadecylamine propoxy derivative (n=10.02)	Unthinned reagent	0.17-4	29.44	29.44	22.08
		25-30	22.08	19.00	19.00
		74-79	22.08	14.72	14.72
		122	22.08, drying	9.63, drying	9.63, drying
	5% wt. aqueous solution	0.17-4	29.44	29.44	22.08
		25-30	19.00	17.66	19.00
		74-79	19.00	12.62	12.62
		122	19.00, drying	12.62, drying	12.62, drying
	5% wt. ethanolic solution	0.17-4	29.44	29.44	29.44
		25-79	29.44	22.08	22.08
		122	29.44, drying	22.08, drying	22.08, drying

References

[1] H.H.Humbatov, R.A.Dashdiyev, Z.H.Asadov et al. Chemical Reagents and Petroleum Production, Baku: Elm, 2001, 448p.

[2] Asadov Z.H. New petrocollecting and petrodispersing surfactants based on ecologically-clean and reproducible kinds of feedstock. Azerbaijan oil industry. 2009, №2, p. 60-65 (in Russian).

[3] Asadov Z., Ahmadova G., Rahimov R. et al. Synthesis and Properties of Quaternary Ammonium Surfactants Based on Alkylamine, Propylene Oxide and 2-Chloroethanol, Journal of Surfactants and Detergents. 2018,21. p.247-254.

[4] Asadov Z., Zarbaliyeva I., Zargarova S. Propoxylation of Aliphatic Amines by Propylene Oxide, Journal of Chemical Problems, 2017,1. p.44-50.

[5] S.H.Zargarova, I.A.Zarbaliyeva, R.A.Rahimov, Z.H.Asadov. Synthesis and Study of Surface-Active Salts Based on Propoxy Derivatives of Dodecylamine and Monocarboxylic Aliphatic Acids. Proceedings of International Scientific-Practical Conference on Petroleum and Gas Industry, Almetyevsk (Russia), 2018, p.587-589.

[6] Ju H., Jiang Y., Geng T., Wang Y. et al. Equilibrium and dynamic surface tension of quaternary salts with different hydrocarbon chain length of counterions. Journal of Molecular Liquids, -2017. 225, -p.606-612.

[7] Chauhan S. A, Kumar K., Rana D., Kumar R. et al. comparative Study on the Aggregation and Thermodynamic Properties of Anionic Sodium Dodecylsulphate and Cationic Cetyltrimethylammonium Bromide in Aqueous Medium: Effect of the Co-solvent N-Methylacetamide // Journal of Surfactants and Detergents, -2016. Volume 19, issue 1, -p.193-200.

[8] Fan Z., Tong W., Zheng Q., Lei Q., Fang W. Surface Activity and Micellization Parameters of Quaternary Ammonium Surfactants Containing a Hydroxyethyl Group, Journal of Chemical and Engineering Data, -2013. 58 (2), -p.334-342.

[9] M.J. Rosen. Surfactants and Interfacial Phenomena, 3rd Edn. New York: John Wiley and Sons, Inc-2004,444p.

Journal of Engineering Sciences & Modern Technologies
ISSN 3078-1760, E-ISSN 3078-1965
Volume 1, Number 1, 2025, page 51-53

BAKI ALİ NEFT MƏKTƏBİ
BAKU HIGHER OIL SCHOOL

https://jesmt.org/

https://doi.org/10.70334/3078-1965.2025.1.51

UDC 661.8

Modification of secondary low density polyethylene (SLDPE) with shell-shaped limestone

Ulviyya Jabiyeva

[a]Baku Higher Oil School, Baku, Azerbaijan, ulviyya.jabiyeva@socar.az

Keywords:

Low density polyethylene; High density polyethylene; Linear; Shell-shaped limestone; Chalk-shaped limestone; Fillers; Exploitation; Modification;

A B S T R A C T

Low-density polyethylene has a good balance of flexibility, strength, barrier properties, and cost and can have a wide combination of properties. Low-density polyethylene has high clarity, is chemically inert, and has good impact strength and excellent tear and stress crack resistance. Low-density polyethylene (LDPE) has applications in sterile blister packs for drug packaging. Linear low-density polyethylene (LLDPE) is used in films and packaging due to its flexibility and toughness.

High-density polyethylene (HDPE) is typically translucent and less flexible than LDPE. Due to its higher crystallinity, it has better chemical resistance, stiffness, and strength than LDPE. Surgical and medical instruments use the vast majority of HDPEs. Like LDPE, HDPE exhibits good chemical and stress crack resistance, radiation resistance, and impact strength.

Received: 30.09.2020
Accept: 26.11.2023

I. Introduction

Low density polyethylene is produced by a high pressure process, and has a mix of long and short branched chains and around 50-65% crystallinity, making it translucent in appearance. It is soft and flexible with good elongation before breakage and good puncture resistance. It has a fair moisture barrier and poor oxygen barrier and softens at around 100°C (lower for some grades), making it an economical polymer to process and readily heat sealable, but of course unsuitable for cook-in packs. In common with all the polyolefins, it is non-polar and must be surface treated prior to printing or laminating [2, 3].

Low density polyethylene (LDPE) is a high branched PE. Its high ramification confers a low density to the molecule as well as a lower hardness, stiffness and strength than high density polyethylene, but with higher ductility. It is semitransparent, and only thin foils can be transparent. That strong ramification hinders the packing of the molecules, diminishing the crystallinity of the material.

The development of new polymer compositions is due to the modification of the existing polymers on the basis of multi-component systems. Fillers are one of the main components in the preparation of low density polyethylene (LDPE) coatings and other polymeric materials. The fillers change the physical and mechanical properties, regulate sustainability and reduced the cost of polymer compositions. Considering these, as local mineral fillers were used the cockle-shell and chalky-shaped limestone. This type of fillers were collected by large quantities in the form of a residue in the limestone industry of Azerbaijan Republic. Every year this type of residues was accrued 10-15% of natural stone production.

Currently, the chemical composition, properties, classification, conditions of grinding, dehydration and the processes of incorporation into polymer compositions have been of natural mineral fillers of limestone. The natural mineral fillers of polymer materials is useful in several ways.

The use of polymer compositions of limestone-type fillers reducing their cost, along with improving

the properties of compositions, allow for the expenditure of these products and consequently for the environmental improvement.

II. Experimental Materials and Preparation

Preparation this type of fillers is related to the selection, grinding, drying, and separation of fillers from stone production enterprises. During research it was used chalk-shaped and shell-shaped limestone samples from the Garadag field. It was selected white type of chalk-shaped and grey type of shell-shaped limestone in this place.

Methods

The samples of limestone were selected, mixed and granulated to a small dispersion in the roller mill. The specific surface of the powder filler of nitrogen vapors was 0.8-1.0m^2/gr by the adsorption in low-temperature. Granulated fillers are dried because they have a moisture content of 10-40% (mass). The drying process was carried out at 105-110^{0}C during 14 hours and the main moisture mass is removed within 6-10 hours. Adsorption does not require expulsion of moisture at 100-150^{0}C (Figure 1).

After drying the limestone was dissolved. The output of powdered limestone was 82-98% (mass). The size of particles is approximately 60 mkm. This data allow the use of the Garadagh shell-shaped limestone for modification of secondary

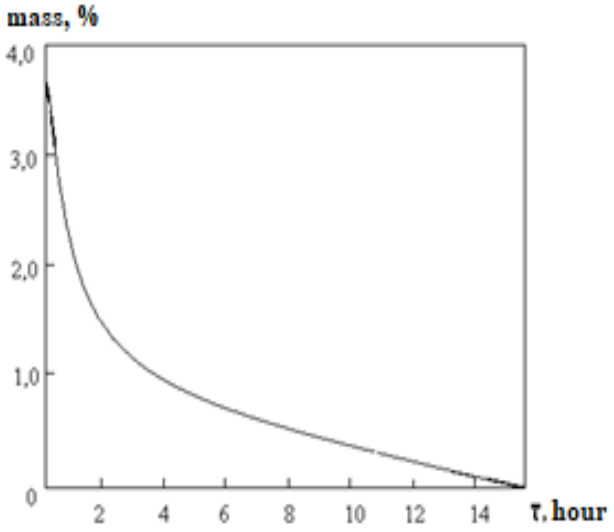

Fig. 1. Drying kinetics of Garadagh shell-shaped limestone, 105^{0}C

LDPE. The main ingredient size of particles is ranging from 6 to 20 mkm in mixtures.

In addition, the chemical composition of the shell-shaped limestone of the Garadagh field is particularly close to the chalk-shaped limestone, which is used as a filler in the polymer industry. In the manufacture of low-thickness products, these fillers are mixed together with plasticizers to prevent contamination [4].

The main physical and mechanical properties of compositions in different quantities were determined (Table 1).

Table 1. Physical and Mechanical Properties of LDPE (16603-011) which was in exploitation and modification

Pressing, %	Heat resistance according to Vika, ^{0}C	Module of flexibility in bending, MPa	Solidity, MPa	Relative extension, %	Fracture resistance, MPa	Flow rate of polymer alloy, 190^{0}C, load 2,16 kg. gr/10 min.	Names of indicators	
3,0	105	98	18	600	12,2	1,1	Primary LDPE	
-	-	42	25	260	7,7	0,075	During exploitation	
0,5	105	70	20	340	8,1	0,4	1	Modified LDPE
0,5	107	71	20	340	8,4	0,4	2	
0,3	110	68	22	320	9,6	0,3	3	
0,1	118	65	22	300	10,3	0,18	4	
0,1	120	60	23	290	10,7	0,12	5	

It has been shown in table that some properties of LDPE (16603-011) during exploitation are improving. This improvement is primarily due to the composition of shell-shaped limestone. The reason is that it contains many metal oxides [5].

The functional - OH, -COOH groups of secondary LDPE, chemically are linked to metal oxides at high temperatures (150-180^{0}C) during mixing and extrusion. Improvement of the properties of LDPE during exploitation is explained by the interaction.

Fracture durability of secondary LDPE increases to 1.8 Mpa in 20-25 mass of filler. At the same time, the increasing of the flow index of alloy and the relative extention indicates that LDPE is plastic. According to the price of these instructions, a modifying amount of shell-shaped limestone was taken 20÷25 mass.

III. Conclusion

After exploitation, the LDPE becomes fragile and its agility module decreases from 98 to 42 MPa. Adding shell-shaped limestone to Secondary LDPE with stearin acid significantly reduces its fragility and increases the agility module to 74 MPa. Generally, the fragility of LDPE makes it difficult to handle during exploitation.

Modification of mineral fillers during exploitation destroys the weak bag structure of secondary LDPE and increases elasticity of polymer.

According to Vika, the increasing of heat resistance is explained by the formation of new bonds in the polymer-filler system. The heat resistance in the optimum number of fillers according to Vika is 110-118 ^{0}C, which is 13^{0}C higher than the original polymer [6].

The results have been shown the modification of LDPE (16603-011) during exploitation with shell-shaped limestone (mineral filler) within 6 months in Absheron are effective. At the same time, the increasing of shell-shaped limestone in the composition to 20÷25 mass, allows for more use than sludge and seolite fillers (6÷8 mass).

LDPE is widely used in packaging like foils, trays and plastic bags for both food and nonfood purposes. It is also used as protective film on paper, textiles and other plastics. For instance, one of the most famous applications is in milk cartons, where it forms part of a system of different plastic layers. Other applications are wrapping foil for packaging, plastic bags (the soft type that does not crackle), garbage bags, tubes or ice cube plastic bags [3].

References

[1] Vinny R. Sastri, in Plastics in Medical Devices (Second Edition), 2014

[2] A. Emblem, in Packaging Technology, 2012

[3] J. Bayer, ... P. Mutjé, in Advanced High Strength Natural Fibre Composites in Construction, 2017

[4] Джафаров В.Д. Изучение наполненных композиционных материалов на основе отрабатованного полиэтилена низкой плотности.// Аз. Хим. жур., 2005, № 1, с. 124-126

[5] Джафаров В.Д., Эфендиев А.А. Синергетический эффект смесей минеральных наполнителей в композициях на основе аппертированного полиэтилена высокого давления. // Пласт. массы. 2007, № 1, с. 28-30

[6] Дувакина Н.И., Ткачева Н.И. Выбор наполнителей для придания специальных свойств полимерным материалам. // Пласт. массы, 1989, № 11, с. 46-48

Journal of Engineering Sciences & Modern Technologies
ISSN 3078-1760, E-ISSN 3078-1965
Volume 1, Number 1, 2025, page 54-59

BAKI ALİ NEFT MƏKTƏBİ
BAKU HIGHER OIL SCHOOL

https://jesmt.org/

https://doi.org/10.70334/3078-1965.2025.1.54

UDC 593.3

The influence of material properties, the geometric shape of the section and temperature on the stressed state of the working bodies

J.Tavbaev[a], A.Shernaev, B.Saparov

[a]Tashkent Institute of Chemical Technology, Tashkent, Uzbekistan, a_shan@bk.ru
[b]Tashkent Institute of Chemical Technology, Tashkent, Uzbekistan, a_shan@bk.ru
[c]Tashkent Institute of Chemical Technology, Tashkent, Uzbekistan, saparov.boburbek@mail.ru

Keywords:

Matrix; bar; inclusions; plastic zone; edge effects; stresses; deformation; crack

A B S T R A C T

In the work on stretching a matrix with a rigid inclusion -an ideal-plastic cylindrical waveguide, a technique was developed for determining the thickness of the boundary layer, which can begeneralized and extended to all problems.

Received: 25.12.2023
Accept: 12.01. 2024

1. Introduction

In this paper, we consider the influence of edge effects arising when pipes and pipelines of a finite length are immersed in another medium. It is assumed that one end or both ends of a pipe or pipeline (hereinafter inclusions) having a finite length is immersed in some foreign medium (hereinafter matrix) in the well and boundary value problems are considered about the current stress state of pipes, pipelines and rods [1-3] ...

In the following, we continue to study the boundary value problems considered in the previous work, taking into account the following additions [4-5]:

a) changes in the shape of the cross-section of the pipe - inclusions;
b) changes in the properties of the inclusion material and matrix - rock;
c) the influence of the thermal effects of the matrix.

2. Research methods

Consider the singular problem of stretching an elastic plane along a thin rigid inclusion of high thermal conductivity and finite width *2l*, coupled to the rest of the body by the matrix at all points of the lateral surface, i.e. conjugate to the matrix. In this case, when the Young's modulus of the inclusion 2l is much greater than its thickness δ, i.e. $\lambda = E^+/E^- \gg 1, \delta/e \ll 1$, where E^+ and E^- – are Young's module of the inclusion and the matrix, respectively, near the inclusion in the matrix there is a boundary layer in which only the shear stress τ_{12} is significant, and all other voltages are negligible [6].

Let us assume that the inclusion is located along the segment $x_2 = 0, |x_1| < l$ in the matrix stretched at infinity by the stress $\tau_{11}=P^{11}$ along the inclusion (Fig. 1).

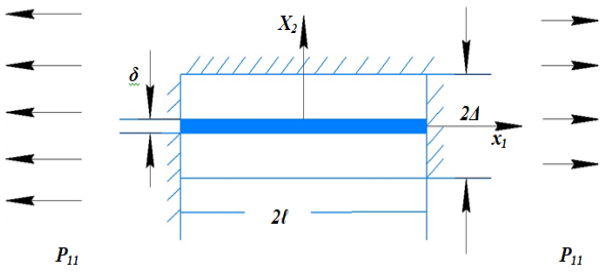

Fig. 1.

The general solution of the boundary layer equations in the matrix is as follows:

$$u_1 = V + \frac{\tau_{12}}{\mu^-} x_2, \quad \tau_{12} = \tau = const \tag{1}$$

Here υ and τ are arbitrary functions x_1, μ is the matrix shift modulus.

As you can see, the stress τ_{12} is constant in the cross-section of the boundary layer and is equal to the shear stress $\tau(x_1)$ on the banks of the inclusion, and the displacement u_1 is linear (function) x_2.

At x_2=0, the boundary layer is associated with an inclusion. Due to rigid adhesion to the matrix, the displacement u_1 of the matrix at this point should be the same as the displacement u_1 of the inclusion.

Therefore, V=V(x_1) in formulas (1) is the displacement of the inclusion at the corresponding points.

At the boundary of the boundary layer at x_2=±A, the field in the boundary layer (1) must be "stitched" with the external, unperturbed field $u_1 = x_1\rho_{11}E^-$ as a condition for "stitching" it is natural to require the equality of the longitudinal deformation $\varepsilon_{11} = \partial u_1/\partial x_1$ and another field at the boundary of the boundary layer at $x_2 = \pm\Delta$.. As a result, based on (1), we obtain

$$V'(x_1) + \frac{\Delta}{\mu -}\tau'(x_1) = \frac{P_{11}}{E^-} \tag{2}$$

Together with the equations

$$\tau = E^+V(x_1), \ \tau = -1/2\partial\dot{t}(x_1) \tag{3}$$

we obtain a closed system of ordinary differential equations for the functions V, τ and τ.

The solution to this system gives the desired solution to the problem posed in the boundary layer approximation [7].

The structure of the field is shown in Fig. 1: the inside of the rectangle $|x_1| \le l, |x_2| \le \Delta$ is the boundary layer, the outside of the same rectangle is the unperturbed field.

First, we exclude $V'(x_1)$ from system (2), (3), we find

$$\tau = E^+\left(\frac{P_{11}}{E^-} - \frac{\Delta}{\mu^-}\tau'(x_1)\right)$$

$$\tau = -1/2\partial\dot{t}(x_1) \tag{4}$$

Now we substitute τ from the second equation in (4) into the first, we obtain

$$\frac{\tau(x_1)}{E^+} = \frac{P_{11}}{E^-} + \frac{\delta\Delta}{2\mu^-}\tau''(x_1) \tag{5}$$

Here, the thickness δ is assumed to be independent of x_1

The general solution of this second-order differential equation has the form:

$$\tau = C_1 l^{\gamma x_1} + C_2 l^{-\gamma x_1} + \frac{P_{11}}{\Delta\delta\gamma^2\left(1+\nu^-\right)} \tag{6}$$

where

$$\gamma = \sqrt{\frac{2\mu^-}{\Delta\delta E^-}} \tag{7}$$

Here C_1 and C_2 are arbitrary constants.

3. Results and discussion

The inclusion can be subjected to direct external loads applied to it. Consider the following four options loaded (Fig. 2).

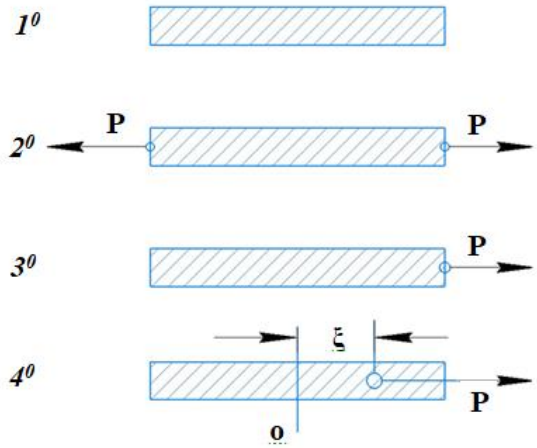

Fig. 2.

1. ***Switching on is free from external loads.*** *In this case, the switch-off ends can be considered unfinished, so that the voltage τ at the ends is equal to zero*

   at $x_1 = \pm l \quad \tau = 0$ (8)

2. ***External forces are applied to both ends of the inclusion.*** *In this case, we have*

   at $x_1 = \pm l \quad \tau = \frac{P}{\delta}$ (9)

   where p is the force per unit of thickness (normal to Fig. 2).

3. ***Force P is applied to only one end.***

   In this case, the following boundary conditions will be

   at $x_1 = -l \quad \tau = 0$

   at $x_1 = \pm l \quad \tau = \frac{P}{\delta}$ (10)

4. ***The force P is applied at some point $x_1 = \xi$ of the inclusion.*** *In this case, the solution has a discontinuity at the point $x_1 = \xi$; find*

   at $x_1 = \pm l \quad \tau = 0$

   at $x_1 = \xi \pm 0$

   $$(\tau(\xi + 0) - \tau(\xi - c)) = \frac{P}{\delta} \tag{11}$$

The linear superposition of these four cases allows us to study the general case of an arbitrary external load on the inclusion [8].

We present the values of the constants C_1 and C_2 in the general solution (6) for the first three cases, obtained as a result of simple calculations:

1. Switching on is free from external loads, only the external p_{11} field in the matrix acts

$$C_1 = C_2 = \frac{-P_{11}}{2\Delta\delta\gamma^2(1+\nu^-)ch\gamma e} \qquad (12)$$

2. Tensile forces P are applied to both ends of the inclusion, there is no external field in the matrix (p_{11}=0):

$$C_1 = C_2 = \frac{P}{2\delta ch\gamma e} \qquad (13)$$

3. Force P is applied only to the right end of the switch, there is no external field in the matrix (p_{11}=0):

$$C_1 = \frac{P}{4\delta}\left(\frac{C_1}{ch\gamma l} + \frac{J_1}{jh\gamma l}\right)$$

$$C_2 = \frac{P}{4\delta}\left(\frac{1}{ch\gamma l} + \frac{1}{jh\gamma l}\right) \qquad (14)$$

In the case of the action of the internal force P at the point $x_1 = \xi$, the solution consists of two analytical parts (piecewise analytical solution):

$$\tau = \begin{cases} V_1 + \frac{1}{\gamma E^+}\left(C_1 e^{\gamma x_1} - C_2 e^{-\gamma x_1}\right) \text{p Ц} -l < x_1 < \xi \\ V_2 + \frac{1}{\gamma E^+}\left(D_1 e^{\gamma x_1} - D_2 e^{-\gamma x_1}\right) \text{p Ц} \xi < x_1 < l \end{cases} \qquad (15)$$

Here V_1 and V_2 are some constants; only one of them can be set equal to zero, since it is determined by the displacement of the body as a whole. Therefore, condition (15) does not provide an additional condition for determining the voltage field in the inclusion.

Note that the equilibrium condition for the entire inclusion as a whole must always be satisfied [9]

$$2\int_{-l}^{+l} \tau(x_1)dx_1 = P \qquad (16)$$

It's not hard to check. that in all previously considered cases 1, 2, 3, the equilibrium condition as a whole is satisfied automatically.

Using solution (14) and (15), we present the following convenient formulas:

$$\begin{cases} C_1 = \frac{1}{4}\tau(\xi - 0)\left(\frac{1}{jh\gamma(l+\xi)} + \frac{1}{ch\gamma(l+\xi)}\right) \\ C_2 = \frac{1}{4}\tau(\xi - 0)\left(\frac{1}{ch\gamma(l+\xi)} - \frac{1}{\xi h\gamma(l+\xi)}\right) \end{cases} \qquad (17)$$

$$\begin{cases} D_1 = \frac{1}{4}\tau(\xi - 0)\left(\frac{1}{ch\gamma(l-\xi)} - \frac{1}{\xi h\gamma(l-\xi)}\right) \\ D_2 = \frac{1}{4}\tau(\xi - 0)\left(\frac{1}{ch\gamma(l-\xi)} + \frac{1}{\xi h\gamma(l-\xi)}\right) \end{cases} \qquad (18)$$

In the considered case of the action of an internal force, on the basis of (2), (3) and (18), one should additionally assume that the function $\tau(x_1)$ is continuous at the point $x_1 = \xi$ of application of an external force P, i.e.

$$\tau(\xi - 0) = \tau(\xi + 0) \qquad (19)$$

Using the second relation (3) and (15), from this we find

$$\tau'(\xi - 0) = \tau'(\xi + 0) \qquad (20)$$

and

$$C_1' l^{\gamma\xi} - C_2' l^{-\gamma\xi} = D_1\ l^{\gamma\xi} - D_2\ l^{-\gamma\xi}$$

On the other hand, conditions (11) based on (15) give

$$\left(D_1 l^{\gamma\xi} + D_2 l^{-\gamma\xi}\right) - \left(C_1' l^{\gamma\xi} + C_{22}' l^{-\gamma\xi}\right) = \frac{P}{\delta}$$

$$C_1' l^{\gamma\xi} + C_2' l^{-\gamma\xi} = 0$$

$$D_1\ l^{\gamma\xi} + D_2\ l^{-\gamma\xi} = 0 \qquad (21)$$

The solution of system (20) and (21), consisting of four linear equations, can be written in the following final form:

4. Force P is applied at the internal point $x_1 = \xi$ of the inclusion, there is no external field in the matrix ($\rho_{11} = 0$)

$$C_1^{(\xi)?} = \frac{P}{2\delta}\left(e^{\gamma\xi}\frac{e^{2\gamma l} - e^{-2\gamma\xi}}{1 - e^{4\gamma l}} - e^{-\gamma\xi}\right) \qquad (22)$$

$$D_1^{(\xi)?} = \frac{P}{2\delta}\cdot e^{\gamma\xi}\cdot\frac{e^{2\gamma l} - e^{-2\gamma\xi}}{1 - e^{4\gamma l}}$$

$$C_1^{(\xi)?} = \frac{P}{2\delta}\cdot e^{-2\gamma\xi}\left(e^{-\gamma\xi} - e^{\gamma\xi}\frac{e^{2\gamma l} - e^{-2\gamma\xi}}{1 - e^{4\gamma l}}\right)$$

$$D_1^{(\xi)?} = -\frac{P}{2\delta}\cdot e^{\gamma(2l+\xi)}\cdot\frac{e^{2\gamma l} - e^{-2\gamma\xi}}{1 - e^{4\gamma l}}$$

$\tau = C_1' e^{\gamma x_1} + C_2' e^{-\gamma x_1}$ at $-l < x_1 < \xi$

$\tau = D_1\ e^{\gamma x_1} + D_2\ e^{-\gamma x_1}$ at $\xi < x_1 < l$

The general qualitative picture of the behavior of the functions $V(x_1)$, $\tau(x_1)$, and $\tau(x_1)$in this case, according to (22), is shown in Fig. 3. the functions $V(x_1)$ and $\tau(x_1)$ are continuous everywhere, but have a break at the point $x_1 = \xi$ (jump of the derivative). The function $\tau(x_1)$ has a discontinuity of the first kind at the point $x_1 = \xi$.

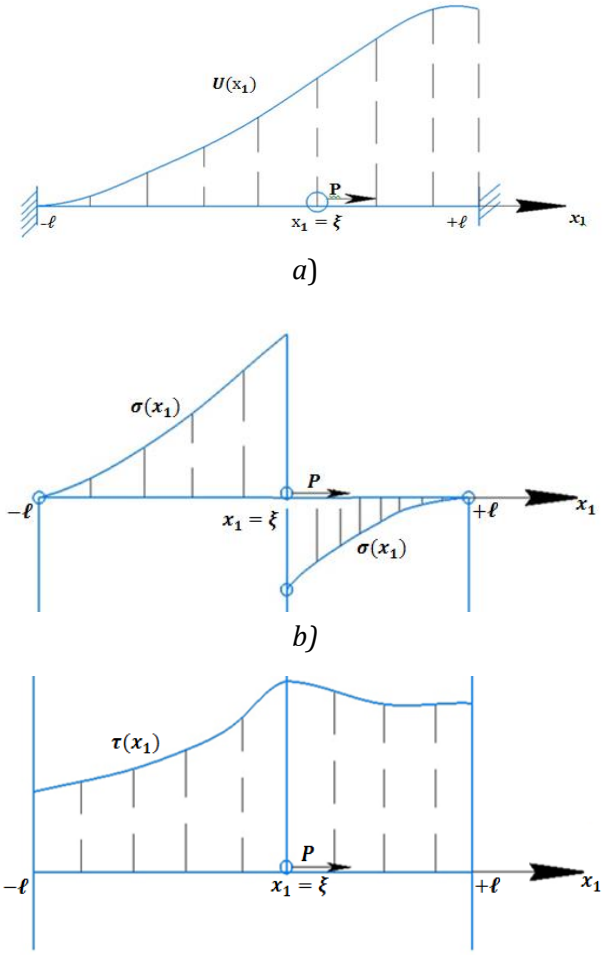

Fig. 3

Solution (22) allows solving the problem of an arbitrarily distributed external load in the inclusion $\rho = \rho(x_1)$. For this, it is necessary to replace p by $p\,d\,\xi$ in formulas (22) and integrate over ξ from $-l$ to l. We get:

$$\tau = \frac{1}{2\delta}\int_{-1}^{+1} p(\xi)\left(e^{\gamma x_1}\left(e^{\gamma\xi}\frac{e^{2\gamma l}-e^{-2\gamma\xi}}{1-e^{4\gamma l}} - e^{-\gamma\xi}\right) + \right.$$

$$\left. + e^{-\gamma x_1}\cdot e^{-2\gamma\xi}\left(e^{-\gamma\xi} - e^{\gamma\xi}\frac{e^{2\gamma l}-e^{-2\gamma\xi}}{1-e^{4\gamma l}}\right)\right) d\xi$$

$(-l<x_1<\xi)$ (23)

$$\tau = \frac{1}{2\delta}\int_{-1}^{+1} p(\xi)\left(e^{\gamma(x_1+\xi)}\cdot\frac{e^{2\gamma l}-e^{-2\gamma\xi}}{1-e^{4\gamma l}} - \right.$$

$$\left. - e^{\gamma(2l-x_1+\xi)x_1}\cdot\frac{e^{2\gamma l}-e^{-2\gamma\xi}}{1-e^{4\gamma l}}\right) d\xi$$

$(\xi < x_1 < +l)$

Using formulas (6), (12) - (14), we study the stresses in the connection for the following most interesting cases [10-12].

1. Switching on is free from external loads, the matrix is stretched by stress p_{11} in an unperturbed field.

In this case

$$\tau = \frac{P_{11}}{\Delta\delta\gamma^2\left(1+\upsilon^-\right)}\cdot\left(1-\frac{ch\gamma x_1}{ch\gamma l}\right) \qquad (24)$$

$(|x_1|<l)$

$$\tau = \frac{P_{11}}{\Delta 2\gamma\left(1+\upsilon^-\right)\Delta}\cdot\frac{jh\gamma x_1}{ch\gamma l}$$

Diagrams of stresses $\tau(x_1)$ and $\tau(x_1)$ in this case are shown in Fig. 4.

The greatest value of the voltage in the inclusion $\tau = \tau_{max}$ is achieved in its middle at $x_1=0$.

$$\tau_{\max} = \frac{P_{11}}{\Delta\delta\gamma^2\left(1+\upsilon^-\right)}\cdot\left(1-\frac{1}{ch\gamma l}\right) \qquad (25)$$

The tangential stress $\tau(x_1)$ at this point vanishes.

Using (7) we transform the divisor value

$$\Delta\delta\gamma^2\left(1+\upsilon^-\right) = \frac{E^-}{E^+} = \frac{1}{\lambda} \qquad (26)$$

Therefore, we have ($\lambda>>l$):

$$\tau = \lambda P_{11}\cdot\left(1-\frac{ch\gamma x_1}{ch\gamma l}\right);\ \tau_{\max} = \lambda P_{11}\cdot\left(1-\frac{1}{ch\gamma l}\right) \qquad (27)$$

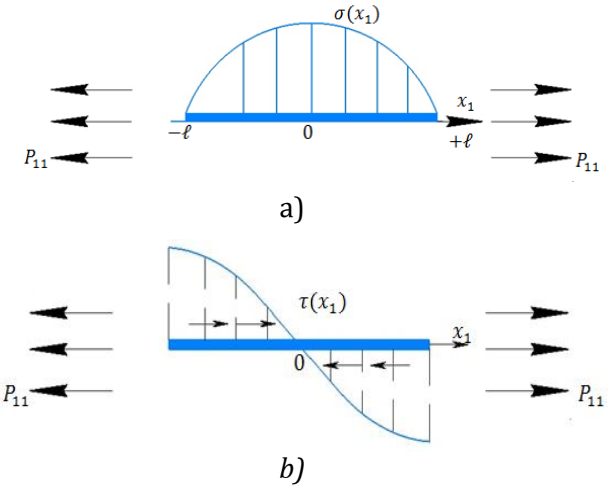

Fig. 4.

Let us dwell in more detail on two limiting cases:

very wide inclusion when γl>>I

$\tau_{max} = \lambda p_{11}$ (28)

ideal-hard switching when γl<<I

$$\tau_{\max} = \frac{1}{2}\lambda p_{11}\gamma^2 l^2 = \frac{l^2 P_{11}}{2\Delta\delta\left(1+\upsilon^-\right)} \qquad (29)$$

As you can see, the wider and tougher the thin inclusion, the greater the stresses are concentrated in it; in this case, in the disturbed zone (boundary layer), the matrix is completely

freed from normal stresses. This reinforcement effect is practically used in composite materials. Switching voltages can be thousands of times higher than matrix voltages [13-17].

However, the possible effect of the inclusion width is limited by the tensile strength of the inclusion, since an inclusion that is too wide breaks in half in the middle. Let us find the maximum width of the inclusion $l=l_{max}$, at which in its middle, at the point $x_1=0$, the limiting tensile strength of the inclusion is achieved $\tau=\tau_B$; using (29), we find

$$l_{\max}=\frac{1}{\gamma}arch\left(1-\frac{\tau_B}{\lambda P_{11}}\right)^{-1} \qquad (30)$$

$0<l<l_{max}$

Thus, the greater the Young's modulus of the inclusion and its tensile strength, the greater the reinforcing effect..

2. Tensile forces p are applied to both ends of the inclusion, there is no external field in the matrix ($\rho_{11}=0$).

In this case, we have

$$\tau=\frac{P_{11}}{\delta}\cdot\frac{ch\gamma x_1}{ch\gamma l} \qquad (31)$$

$$\tau=\frac{-P\gamma}{2}\cdot\frac{jh\gamma x_1}{ch\gamma l} \qquad |x_1|<l$$

The stress diagrams τ and τ in this case are shown in Fig. 5.

The greatest value of stress τ is achieved at the ends of the inclusion, therefore, the possible magnitude of the force p is limited by the strength of the inclusion at break $p\le\delta\tau_B$.

3. Force p is applied only to the right end of the inclusion, there is no external field in the matrix ($p_{11}=0$).

In this case, we have

$$\tau=\frac{P}{\delta}\cdot\left(\frac{ch\gamma x_1}{ch\gamma l}+\frac{jh\gamma x_1}{jh\gamma l}\right) \qquad (32)$$

$$\tau=\frac{-P\gamma}{\delta}\cdot\left(\frac{jh\gamma x_1}{ch\gamma l}+\frac{ch\gamma x_1}{jh\gamma l}\right) \qquad (|x_1|<l)$$

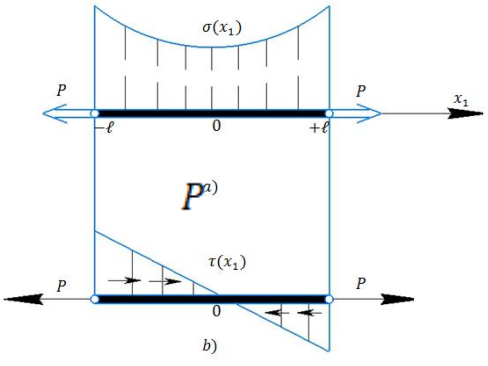

Fig. 5.

Diagrams of stresses τ and τ in the inclusion are shown in Fig. 6.

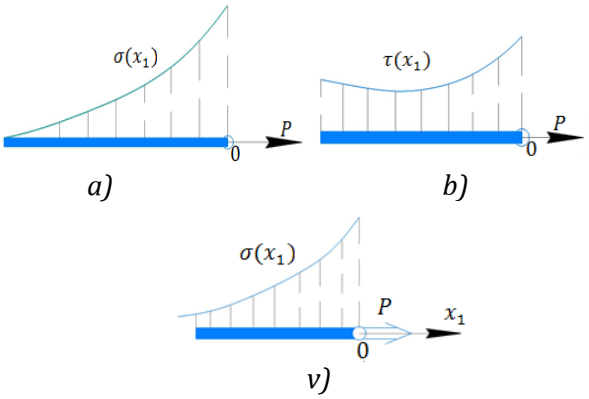

Fig. 6.

Consider one interesting limiting case of this problem, when the width of the inclusion tends to infinity ($\gamma l\to\infty$).

First, in formula (32), we transfer the origin of coordinates to the right end (Fig. 6), we obtain

$$\tau=\frac{P}{2\delta}\cdot\left(\frac{ch\gamma(l+x_1)}{ch\gamma l}+\frac{jh\gamma(l+x_1)}{jh\gamma l}\right) \quad (x_1<0) \qquad (33)$$

For a very wide inclusion, when ($\gamma l\to\infty$), from this we find

$$\tau=\frac{P}{\delta}e^{\gamma x_1};\quad \tau=-\frac{1}{2}p\gamma e^{\gamma x_1} \qquad (34)$$

($\gamma l>>1$, $x_1<0$)

As can be seen, the perturbation from the external force p decays at a distance of the order of ($3/\gamma$) from the end of the inclusion [18-22]

4. Conclusions

We consider the singular problem of stretching an elastic plane along a rigid inclusion of high thermal conductivity and finite length, coupled to the rest of the body by the matrix at all points of the lateral surface, which is conjugate to the matrix. A general technique for solving such problems is built, qualitative and quantitative estimates are given to the stress states of the inclusion and matrix in the following loaded methods:

- switching on is free from external loads;
- external loads are applied to both ends of the connection;
- an external force is applied only to one of the ends of the inclusion;
- external force is applied to an arbitrary switching point.

References

[1] Mamasaidov M.T., Ergashov M., Tavbaev J.S. Strength of flexible elements and pipelines of drilling rigs. Bishkek: Ilim, 2001.-252 p..

[2] Tavbaev J.S. Propagation of a traveling wave in a thread. Incl. "Properties and interactions of waves in threads" Fan.Tashkeent. 2001, pp. 41-60.

[3] Ergashov M., Tavbaev J.S. Strength of pipelines of drilling rigs. Tashkent. Fan. 2002.119 s.

[4] Tavbaev J.S. Determination of the length of the plastic zones and the breaking load of an elastic thread in another medium. Textile problems. 2002. No. 2. S. 83-88.

[5] Tavbaev J.S., Saparov B.J., Rakhimov M.Yu. Investigation of the plastic zones of an elastic bar in an ideal elastoplastic matrix. Scientific, technical and practical journal of composite materials. No. 3/2017

[6] Tavbaev J.S., Saparov B.J., Shernaev A.N. Investigation of cracks in brittle inclusions and matrices. Scientific, technical and practical journal of composite materials № 2/2018

[7] Tavbaev J.S., Saparov B.J., Shernaev A.N. Solving the problem of forming a flat structure of finite width from a high-temperature melt. Scientific, technical and practical journal of composite materials № 3/2018

[8] Tavbaev J.S., Saparov B.J., Shernaev A.N. Calculation of the invariant G-integral. Scientific, technical and practical journal of composite materials №3/2020

[9] Tavbaev J.S., Saparov B.J., Tavbaeva F.J. Methods for strengthening and studying the properties of elastic-viscous materials. Scientific journal "Uz Academia" 3/2020

[10] Tavbaev J.S., Saparov B.J., Narmanov U.A., Narmanov O.A. Research solution of the forming a flat structure of finite width from a high – temperature melt. Annals Of The Romanian Society For Cell Biology., ISSN: 1583-6258, Vol. 25, Issue 6, 2021, Pages. 312-317 Receieved 25 April 2021: Accepted 08 May 2021 https://www.proquest.com/openview/ef40e04c63e535459e2efb1ca22b4a9f/1?pq-origsite=gscholar&cbl=2031963

[11] Saparov B.J., Kodirov A.U., Shernaev A.N., Tavbaev J.S. Analytical study of longitudinal tension of an elastic-plastic matrix with a rigid elastic-plastic inclusion. Universum: technical sciences 5 (86) Moscow May 25, 2021 https://7universum.com/ru/tech/archive/item/11786

[12] Tavbaev J., Saparov B., Kholikulov E. “Solution of the boundary value problem of a semiinfinite waveguide” GALAXY International interdisciplinary research journal (GIIRJ). In Volume 9, Issue 11 Nov., 2021 https://giirj.com/index.php/giirj/article/view/473

[13] Bahadirov, Gayrat and Tsoy, Gerasim and Nabiev, Ayder. (2021). Study of the Efficiency of Squeezing Moisture-Saturated Products (January 29, 2021). EUREKA: Physics and Engineering, (1), 86-96, 2021, doi.10.21303/2461-4262.2021.001606, Available at SSRN: https://ssrn.com/abstract=3778210

[14] Bahadirov GA, Ravutov ShT, Abdukarimov A., Toshmatov E. (2021). Development of the methods of kinematic analysis of elliptic drum of vertical-spindle cotton harvester. IOP Conf. Series: Materials Science and Engineering. 1030 (2021) 012160. doi:10.1088/1757-899X/1030/1/012160

[15] Auezhan T. Amanov, Gayrat A. Bahadirov, Gerasim N. Tsoy, and Ayder M. Nabiev. (2021). "A New Method to Wring Water-Saturated Fibrous Materials," International Journal of Mechanical Engineering and Robotics Research, Vol. 10, No. 3, pp. 151-156, March 2021. DOI: 10.18178/ijmerr.10.3.151-156

[16] Gayrat Bahadirov, Takhirjon Sultanov, Gerosim Tsoy and Ayder Nabiev (2021). Experimental dehydration of wet fibrous materials. E3S Web of Conferences, 264,04060. doi: https://doi.org/10.1051/e3sconf/202126404060

[17] Bahadirov G., Umarov B., Obidov N., Tashpulatov S, and Tashpulatov D. (2021). Justification of the geometric dimensions of drum sorting machine. IOP Conf. Series: Earth and Environmental Science 937 (2021) 032043 IOP Publishing doi:10.1088/1755-1315/937/3/032043

[18] Bykovtsev A .S., Cherepanov G. P. Dynamic growthof curvilinear ruptures at varible speed. Processings of the Sixth ICF. New Delhi. 1984.

[19] Bykovtsev A. S. Modelling of fracture processes ocuring in the focal zone of a tectonic earthquave. “Processings of the Int. Cont. On Computational Mechanics (ICCM 86-Tokyo). 1986. Tokyo. Japan”. Springer-Verlag. 1986.

[20] Bykovtsev A.S., Tovbaev Zh. S. Studies on Wave Fields Caused by a Star-Line Sustem of Propagating Dislogation Ruptures. Proccedings of the Int. Conf on Computational Engeneerings Scince. 1988. Atlanta. G. A. U.S.A. Springer-Verlag. 1988. V. 1-2.

[21] Ergashov M. Mardonov B., Mankovsky Yu. Numerical Simulation of transition Processes in Winding Ties. Inernational Conferencse on computa-tional engeneering science. Hong Kong. 1992.

[22] G.P. Cherepanov. Collision of a bullet with a membrane. Journal of Applied Mechanics and Technical Physics, 2021 - Springer

Journal of Engineering Sciences & Modern Technologies
ISSN 3078-1760, E-ISSN 3078-1965
Volume 1, Number 1, 2025, page 60-64

BAKI ALİ NEFT MƏKTƏBİ
BAKU HIGHER OIL SCHOOL

https://jesmt.org/

https://doi.org/10.70334/3078-1965.2025.1.60

UDC 579.86

The assessment of bactericidal efficacy of seaside water samples and automated detection of sulfate-reducing bacteria using computer vision models

V.M. Abbasov[1], E.A. Aydinsoy[1], D.B. Aghamalieva[1,2], Z.Z. Aghamaliev[1,2]

[1] Institute of Petrochemical Processes, named after Yu.G. Mamedaliyev, Ministry of Science and Education of Azerbaijan, Baku, Azerbaijan
[2] Azerbaijan State University of Oil and Industry, Faculty of Chemical Technology, Baku, Azerbaijan
emil.aydinsoy@gmail.com

Keywords:

Sulfate-reducing bacteria, Caspian Sea, Environmental monitoring, Computer vision

A B S T R A C T

This study examines the presence of sulfate-reducing bacteria, specifically Desulfovibrio desulfuricans, in seawater samples from four coastal sites of the Caspian Sea: Neftchala, Bilgah, Sumgayit, and Pirallahi. The analysis aims to assess microbial dynamics and environmental factors across these locations. sulfate-reducing bacteria concentrations were evaluated using microbiological techniques, revealing significant contamination in the Pirallahi region, likely due to industrial activities. A computer vision model based on the "You only Look Once" algorithm was developed to enhance detection accuracy, automating the identification of Sulfate-Reducing Bacteria infected ampoules. The model demonstrated high accuracy with a mean Average Precision of 99.5 %, precision of 91.6 %, and recall of 98.7 %. This study highlights the potential of combining microbiological assessments with automated detection techniques to improve environmental monitoring. It offers insights into the relationship between industrial pollution and microbial contamination in sensitive marine ecosystems.

Received: 12.11.2024
Accept: 03.12. 2024

I. Introduction

Sulfate-reducing bacteria (SRB) are a diverse group of anaerobic microorganisms that play a crucial role in sulfur and carbon cycling in marine environments. Among them, Desulfovibrio desulfuricans is one of the most studied due to its ability to reduce sulfate to sulfide, influencing the geochemical balance of marine sediments and contributing to biogeochemical processes such as organic matter degradation and nitrogen cycling [1]. The presence and activity of SRB in marine ecosystems are particularly significant because they can lead to the formation of corrosive hydrogen sulfide, posing environmental and industrial challenges, such as biofouling and infrastructure degradation [2]. Understanding the distribution and concentration of SRB, particularly in ecologically sensitive regions like the Caspian Sea, is essential for assessing their impact on both natural ecosystems and human activities.

The Caspian Sea, the world's largest inland body of water, is characterised by unique ecological conditions and diverse coastal environments. Previous studies have shown that microbial types, including SRB, are widely distributed in the sediments and waters of the Caspian Sea, where they participate in essential biogeochemical processes [1, 3]. However, the spatial distribution and concentration of SRB in different coastal locations of the Caspian Sea remain underexplored. This study focuses on analysing the concentration of Desulfovibrio desulfuricans in seawater samples collected from four coastal locations—Neftchala, Bilgah, Sumgayit,

and Pirallahi. By examining the SRB distribution across these sites, we aim to provide insights into the microbial dynamics and environmental factors influencing their presence in this unique marine environment.

In recent years, the use of advanced technologies such as machine learning and computer vision has significantly enhanced our ability to monitor and analyse microbial communities in environmental samples. Object detection models, particularly those based on convolutional neural networks (CNNs), have demonstrated high accuracy in identifying microbial contamination in various contexts [4, 5]. In this study, we developed a computer vision (CV) model to automate the detection of SRB-infected ampoules, offering a novel approach to enhancing the efficiency and accuracy of SRB monitoring. This integration of microbiological analysis with automated detection techniques presents a comprehensive framework for managing microbial contamination in marine environments.

This study hypothesises that the concentration of sulfate-reducing bacteria (SRB), specifically Desulfovibrio desulfuricans, will vary significantly across the four coastal locations of the Caspian Sea — Neftchala, Bilgah, Sumgayit, and Pirallahi — due to differences in industrial activity and environmental conditions. It is expected that sites with higher industrial pollution, particularly Pirallahi, will exhibit higher SRB concentrations, as these bacteria thrive in environments where sulfate is abundant, a condition often exacerbated by industrial discharge. Furthermore, we hypothesise that the integration of computer vision models for SRB detection will demonstrate high accuracy, enabling more efficient and scalable environmental monitoring of microbial contamination in marine ecosystems. This approach is anticipated to streamline the identification process, reducing manual error and improving detection rates in comparison to traditional microbiological techniques.

II. Materials and methods

A. Sample Collection and Preparation

Water samples were collected from four coastal locations along the Caspian Sea in Azerbaijan: Neftchala, Bilgah, Pirallahi, and Sumgayit. Each location has distinct environmental and economic characteristics. Neftchala, a coastal city where Azerbaijan's most significant river flows into the Caspian Sea, is primarily influenced by fishing activities. Bilgah, a coastal region of Baku, is known for its tourism activities, while Pirallahi, another coastal area near Baku, is characterised by extensive oil drilling and processing facilities. Sumgayit, the second-largest city in Azerbaijan, is an industrial hub with numerous factories.

Samples were collected manually by driving to each location and drawing water directly from the seaside using vacuum-sealed buckets (Cordial Company, China) to ensure the preservation of the sample integrity during transport. The collected water samples were transported to the laboratory under controlled conditions to prevent contamination and maintain the samples' original state.

B. Quantification of Sulfate-Reducing Bacteria (SRB)

The concentration of sulfate-reducing bacteria (SRB) in seawater samples collected from the Caspian Sea coastal locations was analysed using a microbiological method adapted from our previous study [6-8]. Desulfovibrio desulfuricans are anaerobic bacteria known for reducing sulfates to sulfides and hydrogen, playing a pivotal role in biogeochemical cycles in marine environments [8-10]. Recent research continues to validate the use of Postgate B nutrient medium as optimal for the cultivation of SRB, where the pH is maintained between 7.0 and 7.5 to create suitable growth conditions [10-12].

To enhance SRB growth, the following additives were included in the Postgate B medium:

- Iron sulfate ($FeSO_4 \cdot 7H_2O$): 0.5-2 mL of a 5 % solution in 2 % hydrochloric acid.
- Sodium bicarbonate ($NaHCO_3$): 1 mL of a 5 % aqueous solution.
- Crystalline sodium sulfide ($Na_2S \cdot 9H_2O$): 1 mL of a solution prepared in 1% sodium carbonate (Na_2CO_3).

The experiments were conducted in 10 mL pre-sterilized test tubes (Cordial Company, China), each containing a water sample inoculated with SRB. The inoculated samples were maintained under anaerobic conditions in a thermostat at a controlled temperature of 30-32°C for an incubation period of 14 days, which allowed sufficient time for the SRB to grow and proliferate in the medium [6,11,12].

The concentration of bacteria in each sample was determined using the serial dilution technique, which involves diluting the sample stepwise and inoculating each dilution onto a growth medium to count colony-forming units (CFUs). The optical density measurements were also taken to estimate bacterial growth quantitatively. The results from different locations—Neftchala, Bilgah, Sumgayit, and Pirallahi—were compared to understand the spatial distribution

of SRB concentrations across the Caspian Sea coastline. These results provide valuable insights into the microbial dynamics of SRB in diverse coastal environments, potentially influenced by factors such as pollution, industrial activity, and natural ecological variations [8,9].

C. Development of the Computer Vision Model for Object Detection

A computer vision (CV) model was developed using the YOLO (You Only Look Once) object detection algorithm to enhance the detection and monitoring of SRB contamination. The images of glass ampoules containing SRB cultures were manually collected from the laboratory. The collected images were then annotated using Roboflow, an online data annotation tool licensed under BY-NC-SA 4.0, to label infected and uninfected ampoules.

The annotated dataset was split into three subsets: 70% for training, 20% for validation, and 10% for testing. The YOLO model was trained on these datasets to detect SRB-infected ampoules accurately. The training process involved adjusting hyperparameters such as learning rate, batch size, and the number of epochs to optimise the model's performance. The evaluation metrics used to assess the model included mean Average Precision (mAP), precision, recall, box loss, class loss, and object loss. These metrics provided a comprehensive understanding of the model's ability to detect SRB contamination with high accuracy and reliability [13-15].

III. Results

A. Sulfate-reducing bacteria (SRB) Concentration in Seaside Water Samples

The concentration of sulfate-reducing bacteria (SRB) was analysed in seawater samples collected from four coastal locations along the Caspian Sea: Neftchala, Bilgah, Sumgayit, and Pirallahi. The analysis revealed that SRB was not detected in Neftchala, Bilgah, and Sumgayit samples, with SRB concentrations measuring 0 colony-forming units per millilitre (CFU/mL). Sulfate-reducing bacteria typically live in colonies, forming clusters and spreading along the walls of the test tubes. Based on the results from tube number 3, a 1 mL water sample taken from the Pirallahi area revealed the presence of thousands of sulfate-reducing bacteria (SRB). Given that the metabolic byproduct of SRB is H_2S, the amount of H_2S was analysed after quantifying the SRB. The sample from test tube number 3 was titrated using the iodometric titration method, revealing an H_2S concentration of 256 mg/L. This high level of H_2S suggests that, due to the acidic nature of the environment, the corrosion process is proceeding at an accelerated rate.

Given the limited dataset and the binary nature of SRB detection (presence or absence), Fisher's exact test (n=40) was applied to determine whether there was a statistically significant difference in the presence of SRB between Pirallahi and the other three locations (Neftchala, Bilgah, and Sumgayit). Fisher's exact test was chosen due to its suitability for small sample sizes and categorical data, comparing SRB presence across the four locations. The 2x2 contingency table (Table 2) below summarises the SRB detection across locations:

Table 1. 2x2 Contingency Table Comparing SRB Presence in Pirallahi vs. Other Locations

Location	SRB Present	SRB Absent	Total
Pirallahi	3	7	10
Other Locations	0	30	30
Total	3	37	40

Fisher's exact test revealed a statistically significant difference in SRB presence between Pirallahi and the other locations, with a p-value of 0.012 ($p < 0.05$). This result suggests that the presence of SRB in Pirallahi is unlikely to be due to random variation and is more likely associated with specific local environmental or industrial factors. The odds ratio was calculated as "infinity" (inf), further indicating that the odds of detecting SRB in Pirallahi are infinitely higher compared to the other locations where SRB was not detected at all.

B. Performance of the Computer Vision Model for Object Detection

A computer vision (CV) model based on the YOLO (You Only Look Once) object detection algorithm was developed to automate the detection of SRB contamination in glass ampoules. The model demonstrated high accuracy and robustness in detecting SRB-infected ampoules, as evidenced by the following performance metrics mentioned in Table 2.

Table 2. Models Performance metrics

Mean Average Precision (mAP)	Precision	Recall
99.5%	91.6%	98.7%

The mAP metric, which measures the accuracy of object detection models, was exceptionally high at 99.5 %, indicating the model's excellent performance in correctly identifying both true positives and negatives. Precision, which measures the proportion of accurate positive detections among all detections, was 91.6 %, while recall, the proportion of accurate positive

detections among all actual positives, reached 98.7 %. These results demonstrate the model's effectiveness in minimising false positives and false negatives.

Figures 1-4 illustrate the training process and model performance:

- Figure 1: mAP scores over 300 epochs showing stable performance after initial training fluctuations.
- Figure 2: Box Loss over 300 epochs, indicating a steady decrease as the model learned to localise the detected objects better.
- Figure 3: Class Loss over 300 epochs, showing a continuous decrease, demonstrating the model's improved ability to classify detected objects correctly.
- Figure 4: Object Loss over 300 epochs, highlighting co nsistent learning in detecting objects against the background.

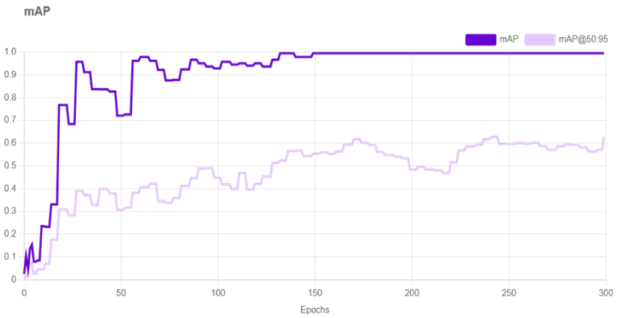

Fig 1. mAP Performace over 300 training epochs

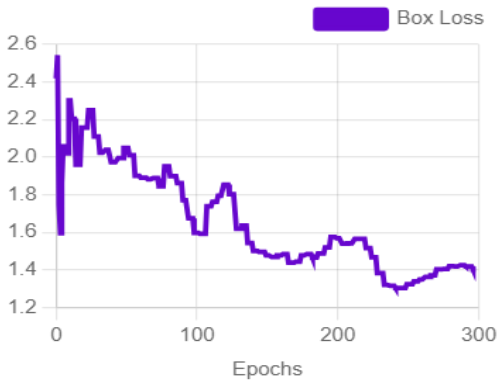

Fig 2. Box loss trend over 300 training epochs

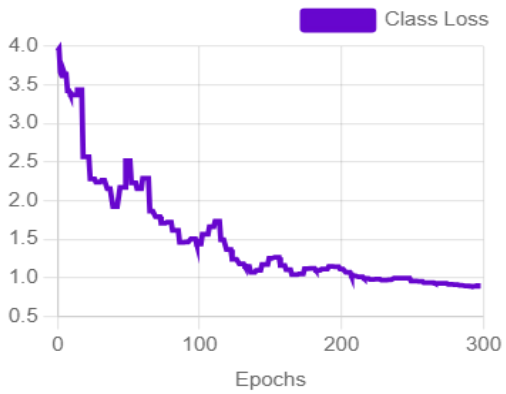

Fig 3. Class loss trend over 300 training epochs

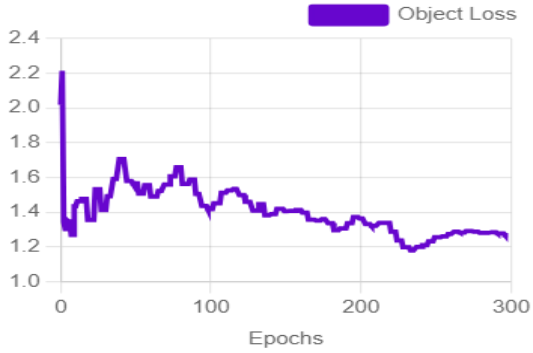

Fig 4. Object loss trend over 300 training epochs

C. Visualization of Detection Results

Fig. 5 depicts the successful detection of SRB-infected ampoules using the trained computer vision model. The model accurately identifies the infected ampoules, demonstrating its utility in real-world applications for monitoring SRB contamination. The detection is visualised with bounding boxes, indicating the model's confidence in identifying the contamination.

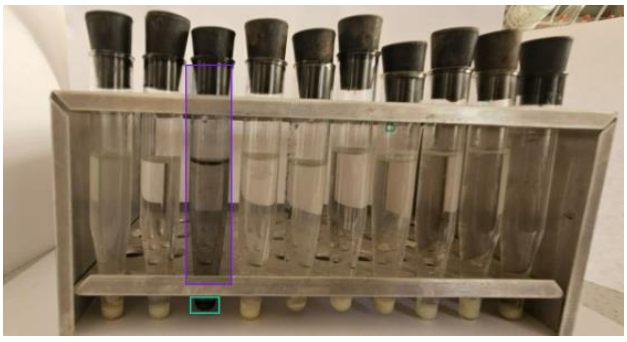

Fig. 5. Detection of SRB-infected ampoule

IV. Conclusion

This study highlights the localised presence of sulfate-reducing bacteria (SRB), specifically Desulfovibrio desulfuricans, in the coastal waters of the Caspian Sea, with a significant concentration detected only in Pirallahi, a region characterised by extensive oil drilling activities. This finding

suggests a potential link between industrial pollution and microbial contamination in marine environments. Additionally, developing and successfully applying a computer vision model based on the YOLO algorithm for automated detection of SRB-infected ampoules demonstrates a powerful tool for environmental monitoring. The model achieved high accuracy, precision, and recall, underscoring its potential to enhance traditional microbiological assessments with rapid, automated analysis. Integrating advanced AI techniques with microbiological studies can provide a more efficient and scalable approach to managing microbial risks in marine and other sensitive ecosystems.

References

[1] N. Mahmoudi, M.S. Robeson, H.F. Castro, Microbial community composition and diversity in Caspian Sea sediments, FEMS Microbiol. Ecol. 91 (2015) 1-11. https://doi.org/10.1093/femsec/fiu013.

[2] Z. Qian, H. Tianwei, H.R. Mackey, M.C.M. van .Loosdrecht, C. Guanghao, Recent advances in dissimilatory sulfate reduction: From metabolic study to application, Water Res. 150 (2019) 162–181. https://doi.org/10.1016/j.watres.2018.11.018.

[3] L. An, Y. Yan, H. Tian, C.Q. Chi, Y. Nie, X.L. Wu, Roles of sulfate-reducing bacteria in sustaining the diversity and stability of marine bacterial communities, Front. Microbiol. 14 (2023) 1218828. https://doi.org/10.3389/fmicb.2023.1218828.

[4] P. Gao, X.L. Huang, Z. Chen, A. Marietou, L. Holmkvist, L. Qu, K. Finster, X. Gong, Genomic insight of sulfate-reducing bacterial genus Desulfofaba reveals their metabolic versatility in biogeochemical cycling, BMC Genomics 24 (2023) 297. https://doi.org/10.1186/s12864-023-09297-2.

[5] M.B. Berens, T.W. Deen, C.L. Chun, Bioelectrochemical reactor to manage anthropogenic sulfate pollution for freshwater ecosystems: Mathematical modeling and experimental validation, Chemosphere 357 (2024) 142054. https://doi.org/10.1016/j.chemosphere.2024.142054.

[6] V.M. Abbasov, D.B. Aghamaliyeva, T.A. Ismailov, et al., Study of the bactericidal effect of dialkylamine complex salts of oleic acid on the vital activity of sulfate-reducing bacteria, PPOR, Spec. Issue (No. 1) (2024) 32–39. https://doi.org/10.62972/1726-4685.si2024.1.32.

[7] C. Wu, Z. Wang, Z. Zhang, B. Zhang, G. Ma, Q. Yao, Z. Gan, J. Wu, X. Li, Influence of crevice width on sulfate-reducing bacteria (SRB)-induced corrosion of stainless steel 316L, Corros. Commun. 4 (2021) 33–44. https://doi.org/10.1016/j.corcom.2021.12.001.

[8] S. Permeh, K. Lau, B. Tansel, M. Duncan, Surface conditions for microcosm development and proliferation of SRB on steel with cathodic corrosion protection, Constr. Build. Mater. 243 (2020) 118209. https://doi.org/10.1016/j.conbuildmat.2020.118209.

[9] V. Liduino, M. Galvão, S. Brasil, E. Sérvulo, SRB-mediated corrosion of marine submerged AISI 1020 steel under impressed current cathodic protection, Colloids Surf. B Biointerfaces 202 (2021) 111701. https://doi.org/10.1016/j.colsurfb.2021.111701.

[10] L. Chen, B. Wei, X. Xu, Effect of sulfate-reducing bacteria (SRB) on the corrosion of buried pipe steel in acidic soil solution, Coatings 11 (2021) 625. https://doi.org/10.3390/coatings11060625.

[11] N.D. Nabiyeva, D.B. Aghamaliyeva, T.A. Ismayilov, Study of inhibitory-bactericidal properties of the byproduct of white oil production against deemulsifier and corrosion, PPOR 22 (2021) 546–551.

[12] V.M. Abbasov, D.B. Aghamaliyeva, L.M. Afandiyeva, Z.Z. Aghamaliyev, N.M. Aliyeva, Z.N. Pashayeva, F.C. Gurbanova, The study of the effect of alkylhalogenide complexes of amidoamine of corn oil on the kinetics of CO_2 corrosion, PPOR 25 (2024) 313–322. https://doi.org/10.62972/1726-4685.2024.2.313.

[13] V.M. Abbasov, Z.Z. Aghamaliyev, E.A. Aydinsoy, N.Y. Alimadatli, Modelling an image detection algorithm to evaluate the degree of corrosion, PPOR 24 (2023) 589–596. https://doi.org/10.36719/1726-4685/95/589-596.

[14] V.M. Abbasov, R.E. Azizov, Z.Z. Aghamaliyev, E.A. Aydinsoy, N.Y. Alimadatli, The localization of oil leaks in the sea using satellite and drone images with artificial intelligence models, Proc. Azerbaijan High Tech. Educ. Inst. 26 (2024) 421–431. http://dspace.azjhpc.org/xmlui/handle/123456789/413.

[15] E.E. Aydinsoy, Z.Z. Aghamaliyev, D.B. Aghamaliyeva, V.B Abbasov, A systematic review of corrosion inhibitors in marine environments: insights from the last 5 years. PPOR 25 (2024) 793-843. https://doi.org/10.62972/1726-4685.2024.3.793

JESMT
JOURNAL OF ENGINEERING SCIENCES & MODERN TECHNOLOGIES

About the Journal

The "Journal of Engineering Sciences and Modern Technologies" (JESMT) was founded in Baku Higher Oil School in 2024. The JESMT aims to provide a comprehensive platform for researchers, practitioners, and industry professionals to disseminate and discuss significant advancements and emerging trends in the fields of technology and engineering sciences. The journal covers a wide range of topics, including but not limited to:

- *Information and Communication Technology (ICT): Innovations in software and hardware, network and communication systems, cybersecurity, artificial intelligence, machine learning, and data analytics.*
- *Engineering Sciences: Developments in civil, mechanical, electrical, chemical, and materials engineering, including novel methodologies, design, and applications.*
- *Emerging Technologies: Exploration of cutting-edge technologies such as nanotechnology, biotechnology, quantum computing, renewable energy systems, and autonomous systems.*
- *Interdisciplinary Research: Integration of technology and engineering with other disciplines such as healthcare, environmental sciences, and social sciences to address complex global challenges.*
- *Petrochemical direction: Emulsion and technology of applications, Enhanced Oil Recovery and applications technology, Catalysts and engineering, and Application of surfactants technology.*

The journal accepts original research articles, review papers, case studies, and technical notes that contribute to the body of knowledge and practical applications in modern technology and engineering.

Aims and Scope

The primary aim of the "Journal of Engineering Sciences and Modern Technologies" is to foster innovation and excellence in the fields of technology and engineering by:

1. *Promoting Knowledge Sharing: Providing a platform for the exchange of ideas, research findings, and technological advancements among academics, researchers, and industry professionals.*
2. *Encouraging Interdisciplinary Collaboration: Bridging the gap between different disciplines to encourage collaborative research that addresses complex problems and leads to holistic solutions.*
3. *Supporting Emerging Researchers: Offering opportunities for early-career researchers and students to publish their work and gain visibility in the scientific community.*
4. *Advancing Practical Applications: Highlighting research that has significant practical implications and can be translated into real-world solutions to benefit society.*
5. *Maintaining High Standards of Excellence: Ensuring the publication of high-quality, peer-reviewed articles that adhere to rigorous scientific and ethical standards.*

Through these aims, JESMT strives to be a leading journal that contributes to the advancement of technology and engineering sciences, fostering innovation, and supporting the development of sustainable solutions for contemporary challenges.

Journal of Engineering Sciences & Modern Technologies

Author Guidelines

Format:

Manuscripts should be submitted in two formats, as single A4 size Word and PDF files, inclusive of abstract, endnotes and references. Introduction and conclusion sections are compulsory.

Font and spacing:

Please use Times New Roman 11pt. All submissions including essential data only should be typed in single spacing.

Language:

The journal is published in English. Please write your article in good English (American or British usage is accepted, but not a mixture of these). In order to avoid possible grammatical or spelling errors and to make your work readable and understandable for readers, we advise you to get your work proofread by professionals or native speakers before submitting it.

Cover Page / Title: Short and informative

On the first page of the paper, present the title of the paper along with the authors' names, institutional affiliations, and contact information. The corresponding author(s) (i.e., the one[s] who will be in contact with the reviewers) must be specified, usually with a footnote or an asterisk (*), and their full contact details (e.g., email address and phone number) must be provided.

For example:
Dr. Clara A. Bell[1,*] and Dr. Scott C. Smith[2]
[1]University of Areopagitica, Department of Biology, Sometown, Somecountry
[2]Leviathan University, Department of Biochemistry and Biomedical Sciences, Sometown, Somecountry
*clara.bell@emailaddress.com

Abstract: 1 paragraph

- The abstract needs to be in English.
- State the research subject (i.e., what was done) and encapsulate the main findings and conclusions of the paper.
- Do not add citations in an abstract (the reader might not be able to access your reference list).
- Avoid using acronyms and abbreviations in the abstract, as the reader may not be familiar with them. Use full terms instead.

Keywords: 3-7 words

Below the abstract, include a list of key terms to help other researchers locate your study. Note that "keywords" is one word (with no space) and is followed by a colon:

Keywords: paper format, scientific writing.

Article Structure

Divide your article into clearly defined and numbered section. Subsections should be numbered 1.1. (then 1.1.1, 1.1.2, …), 1.2, etc. Any subsection may be given a brief heading. Each heading should appear on its own separate line.

Introduction

Introduction should be clear and concise. Include relevant background information on the topic, using in-text citations as necessary. Report new developments in the field, and state how the research fills gaps in the existing research. Focus on the specific problem addressed, along with its possible solutions, and outline the limitations of your study. A research question hypothesis, and/or objectives can also be included at the end of this section.

Methods

- This is the part of the paper that explains *how* the research was done. Relate the research procedures in a clear, logical order (i.e., the order in which you conducted the research) so that other researchers can reproduce your results. Simply refer to the established methods you used but describe any procedures that are original to your study in more detail.
- Identify the specific instruments used in your research by including the manufacturer's name and location in parentheses.
- Stay consistent with the order in which information is presented (e.g., quantity, temperature, stirring speed, refrigeration period).

Results

- Do not include too many details, particularly if you are using tables and figures. While writing this section, be consistent and use the smallest number of words necessary to convey your statistics.
- Use headings to help the reader follow along, particularly if your data are repetitive (but check whether your style guide allows you to use them).

Discussion

- Present your general conclusions, including an assessment of the strengths and weaknesses of the research and the implications of your findings. Resolve the hypothesis and/or research question you identified in the introduction.
- Use in-text citations to support your discussion.
- Do not repeat the information presented in the results or the introduction unless it is necessary for a discussion of the overall implications of the research.

Conclusion

Keep this section short. Explain how your research fits within your field of study and identify areas for future research.

Appendices

If there is more than one appendix, they should be identified as A, B, etc. Formulae and equations in appendices should be given separate numbering: Eq. (A.1), Eq. (A.2), etc.; in a subsequent appendix, Eq. (B.1) and so on. Similarly for tables and figures: Table A.1' Fig. A.1, etc.

Acknowledgements (optional)

Write a brief paragraph giving credit to any institution responsible for funding the study (e.g., through a fellowship or grant) and any individual(s) who contributed to the manuscript (e.g., technical advisors or editors).

Reference Style

Text: Indicate references by number(s) in square brackets in line with the text. The actual authors can be referred to, but the reference number(s) must always be given.

Example: '...as demonstrated [3,6]. Barnaby and Jones [8] obtained a different result ....'
List: Number the references (numbers in square brackets) in the list in the order in which they appear in the text.

Examples:

Reference to a journal publication:

[1] J. van der Geer, J.A.J. Hanraads, R.A. Lupton, The art of writing a scientific article, J. Sci. Commun. 163 (2010) 51–59. https://doi.org/10.1016/j.Sc.2010.00372.

Reference to a journal publication with an article number:

[2] J. van der Geer, J.A.J. Hanraads, R.A. Lupton, 2018. The art of writing a scientific article. Heliyon.19, e00205. https://doi.org/10.1016/j.heliyon.2018.e00205.

Reference to a book:

[3] W. Strunk Jr., E.B. White, The Elements of Style, fourth ed., Longman, New York, 2000.

Reference to a chapter in an edited book:

[4] G.R. Mettam, L.B. Adams, How to prepare an electronic version of your article, in: B.S. Jones, R.Z.

Smith (Eds.), Introduction to the Electronic Age, E-Publishing Inc., New York, 2009, pp. 281–304.

Reference to a website:

[5] Cancer Research UK, Cancer statistics reports for the UK. http://www.cancerresearchuk.org/ aboutcancer/ statistics/cancerstatsreport/, 2003 (accessed 13 March 2003).

Reference to a dataset:

[dataset] [6] M. Oguro, S. Imahiro, S. Saito, T. Nakashizuka, Mortality data for Japanese oak wilt disease and surrounding forest compositions, Mendeley Data, v1, 2015. https://doi.org/10.17632/xwj98nb39r.1.

Tables and Figures (one per page)

- Capitalize the titles of specific tables and figures when you refer to them in the text (e.g., "see Table 3"; "in Figure 4").
- In tables, stay consistent with the use of title case (i.e., Capitalizing Each Word) and sentence case (i.e., Capitalizing the first word).
- In figure captions, stay consistent with the use of punctuation, italics, and capitalization. For example:

Figure 1. Classification of author roles.

versus

Figure 2: taxonomy of paper keywords

Terminology

- Stay consistent with the terms you use. Generally, short forms can be used once the full term has been introduced
- Use standard scientific terminology. Italics must be used correctly for scientific terminology.

Equations

Whether in mathematical, scientific, or technical papers, equations follow a conventional format. Here are some tips for formatting calculations:

- Number each equation you present in the text, inserting the number in parentheses.

$$X + Y = Z \quad (1)$$

- Capitalize the word "Equation" when you refer to equations within the text.

In Equation 1, X represents . . .
(Note also that you should use italics for variables.)

- Remember to save your math equations as editable text and not as images in case changes need to be made before publication.

Measurements

- Use International System of Units (SI).
- Add spaces before units of measurement. For example, 2.5 mL not 2.5mL.
- Be consistent with your units of measure (especially date and time). For example, 3 hours or 3 h.

Supplementary material

Supplementary material, such as images (photographs) and drawings, can be published with your article to enhance it.

- Vector drawings (PDF): embed the font or save the text as 'graphics".
- Color or greyscale photographs (JPG): always use a minimum of 300 dpi.
- Bitmapped line drawings (JPG): use a minimum of 1000 dpi.
- Combinations bitmapped line/half-tone (color or grayscale) (JPG): a minimum of 500 dpi is required.

Statistics

The following to be included for statistical testing: the name of each statistical analysis, along with its *n* value; an explanation of *why* the test was used and *what* is being compared; and the specific alpha levels and P values for each test.

Quotations

Quoted words, phrases and sentences should be enclosed in double quotation marks. Quotations within quotations and glosses should be enclosed in single quotation marks.

Notes

- Notes should be kept to a minimum.
- Use endnotes, not footnotes.
- All notes should be numbered in sequence and in Arabic numeral, typed in double spacing and placed at the end of the main text.
- Notes should contain additional information to the particular discussion.
- Bibliographic notes are not allowed.

Submission declaration

It is implied that the submitted article neither has been published previously nor is under consideration for publication elsewhere. If accepted, it will not be published elsewhere in the same form, in English or in any other language, including electronically without the written consent of the publisher, *BHOS Journal of Engineering Science and Technology*.

To submit a paper use the link:
http://jesmt.org

JOURNAL OF ENGINEERING
SCIENCES & MODERN TECHNOLOGIES

www.jesmt.org